




University of
Stavanger

Faculty of Science and Technology

MASTER'S THESIS

Study program/Specialization: Petroleum Geosciences Engineering	Spring semester, 2017 Open
Writer: Farid Ebrahim	 (Writer's signature)
Faculty supervisor: Wiktor Waldemar Weibull	
Title of thesis: Converted wave imaging and velocity analysis using elastic reverse-time migration	
Credits (ECTS): 30	
Keywords: Converted waves Multi-component Elastic reverse-time migration Imaging conditions Stack-power optimization Co-depthing De-migration Target image fitting	Pages: 102 Stavanger, June 22 nd , 2017

Converted wave imaging and velocity analysis using elastic reverse-time migration

by

Farid Mahmoud Ebrahim

Thesis for the degree of Master of Science

Petroleum Geosciences Engineering

Presented to the Faculty of Science and Technology

University of Stavanger

University of Stavanger

June 2017

“If I have seen further, it is by standing on the shoulders of giants.”

Isaac Newton

“The seeker after truth is not the one who studies the writings of the ancients and, following his natural disposition, puts his trust in them, but rather the one who suspects his faith in them and questions what he gathers from them, the one who submits to argument and demonstration and not the sayings of human beings whose nature is fraught with all kinds of imperfection and deficiency. Thus the duty of the man, who investigates the writings of scientists, if learning the truth is his goal, is to make himself an enemy of all that he reads, and, applying his mind to the core and margins of its content, attack it from every side. He should also suspect himself as he performs his critical examination of it, so that he may avoid falling into either prejudice or leniency.”

Ibn al-Haytham

Acknowledgement

I would like to thank my supervisor Wiktor Waldemar Weibull for the most interesting educational experience I ever had, for his patience and support, for the time he spent helping me even before starting this project, and for sharing his ideas and making me part of this work. In this thesis, the theoretical framework and the algorithms used were provided by Wiktor Waldemar Weibull. I am really grateful for this opportunity and will forever be indebted to his teaching and guidance.

I owe my deepest gratitude to my family, those who have been always supporting me, providing the main reasons for keeping my motivation and purpose.

I would like to thank the University of Stavanger for this fantastic and personally rewarding experience. I thank Annette and Øystein for the interesting talks and the friendly atmosphere in our lab. It was a great pleasure to meet all the great people in petroleum geosciences engineering department; Amrizal, Anastasiia, Andres, Angelica, Bilal, Eirik, Ivan, Isaias, Javed, Juan Carlos, Sayyid, Xiaoan, to name but a few. Special thanks go to my friends Amr, Hakar, Ibrahim, Laith, Malik, Osama and Rami for the magnificent time we had together along the last two years.

I acknowledge UNINETT Sigma2 project and its consortium partners for providing required computational resources. I thank the support teams of Abel, Stallo, and Vilje clusters for their helpful support. I also would like to thank Andreas Habel for providing technical support and the support teams of VISTA® and ProMAX® software.

Abstract

Converted wave imaging and velocity analysis using elastic reverse-time migration

Farid Mahmoud Ebrahim, M.Sc.

The University of Stavanger, 2017

Supervisor: Wiktor Waldemar Weibull

Along the continuous evolution of exploration seismology, the main objective has been producing better subsurface seismic images that lead to lower risk exploration and enhanced production. The unique characteristics of converted (P-S) waves enable retrieving more accurate subsurface information, which made it play a complementary role in hydrocarbon seismic exploration, where the primary method of conventional compressional wave (P-P) data has limited capabilities. Conventional processing techniques of P-S data are based on approximations that do not respect the elastic nature of the subsurface and the vector nature of the recorded wave-fields, which urge the need for accurate modeling of subsurface velocity fields, and elastic imaging algorithm that can overcome the shortcomings following the conventional approximations. In this thesis we presented a novel workflow for accurate depth imaging and velocity analysis for multi-component data. The workflow is based on elastic reverse-time migration as a robust migration algorithm, and automatic wave equation migration velocity analysis techniques. We practically tested novel imaging conditions for elastic reverse-time migration in order to overcome the polarity reversal problem and investigated the cross-talking between wave-modes. For velocity analysis we applied stack-power maximization to produce improved velocity fields that enhance the image coherency, then we applied co-depthing technique based on novel Born modeling/demigration method and target image fitting procedure in order to produce the shear-wave velocity model that result in depth consistent P-S and P-P images. We successfully implemented the workflow on synthetic and field datasets. The results obtained show the robustness and practicality of the workflow to produce enhanced velocity models and accurate subsurface elastic images.

Contents

Acknowledgement	iv
Abstract	v
Contents	vi
List of Figures	viii
List of Equations	xiii
1 Introduction.....	1
1.1 Background	1
1.2 Thesis objectives	2
1.3 Thesis outline	2
1.4 Wave propagation in elastic isotropic media	4
1.5 Converted waves and multi-component data	5
1.5.1 Overview.....	5
1.5.2 Challenges.....	11
2 Fast-track conventional processing of Blackfoot 3C-3D dataset.....	20
2.1 Introduction	20
2.2 Method	21
2.2.1 Processing of vertical component	21
2.2.2 Processing of radial component	24
2.3 Discussion	29
3 Multi-component elastic reverse-time migration in isotropic media.....	31
3.1 Introduction	31
3.2 Theory	32
3.3 Synthetic example	34
3.4 Field data example	37
3.5 Impact of attenuation.....	48
3.6 Discussion	52
4 Multi-component automatic velocity analysis via elastic reverse-time migration	54
4.1 Introduction	54

4.2	Theory	55
4.3	Synthetic data example.....	57
4.4	Field data example	60
4.4.1	2D example	60
4.4.2	3D example	70
4.5	Discussion	74
5	Tomographic co-depthing of P-P and P-S images based on elastic reverse-time de-migration	77
5.1	Introduction	77
5.2	Theory	78
5.3	Synthetic data example.....	81
5.4	Field data example	85
5.5	Discussion	90
6	Conclusions.....	92
	References.....	94

List of Figures

Figure 1.1: Wave-mode conversion with particle motion and propagation directions of compressional and shear waves. Adapted from (Barkved et al., 2004).....	6
Figure 1.2: Ocean bottom cable seismic acquisition. P-S data recorded by a receiver station will represent a different spatial subsurface position than P-P data. Adapted from (Ikelle and Amundsen, 2005).....	6
Figure 1.3: Gas chimney effect over Ekofisk field. Conventional P-P image from 3D streamer data compared to the enhanced P-S image using only the horizontal (X) component from OBC data. Adapted from (Granli et al., 1999).....	8
Figure 1.4: P-P image (left) showing flat spot and associated gas cap above it, and the absence of the feature in the related P-S image (right) confirming the fluid related anomaly. From (Cafarelli et al., 2006)	9
Figure 1.5: An example from Alba field showing the improved reservoir image using converted waves, where the top of reservoir is easily identified leading to efficient well placement. From (MacLeod et al., 1999).....	9
Figure 1.6: Geometrical illustration of P-P reflection data at its midpoint (MP) and P-S reflection data at its conversion point (CP). The P-wave angle of incidence is given by θ and S-wave angle of reflection is given by ϕ . Adapted from (Stewart et al., 2002)	10
Figure 1.7: P-P and P-S reflection coefficients as a function of P-wave angle of incidence. The S-wave velocities for the upper and lower layers are 1750 m/s and 2650 m/s, respectively. Density is constant. Adapted from (Stewart et al., 2002)	10
Figure 1.8: Result of finite-difference forward modeling of three-component geophones response to pressure source (left-side) and to explosive source (right-side). The geophones are oriented according to in-line (X -component) and cross-line (Y -component) directions in plane with the source. Top figures represent data recorded by vertical (Z -component). Middle figures represent data recorded by horizontal (X -component). Bottom figures represent data recorded by horizontal (Y -component).....	13
Figure 1.9: Result of finite-difference forward modeling of three-component geophones response to pressure source (left-side) and to explosive source (right-side) in isotropic media. The geophones are oriented according to in-line (X -component) and cross-line (Y -component) directions with variable source-receiver azimuth. Top figures represent data recorded by vertical (Z -component). Middle figures represent data recorded by horizontal (X -component). Bottom figures represent data recorded by horizontal (Y -component).	14
Figure 1.10: Shear wave splitting to fast shear-wave parallel to maximum horizontal stress (σ_H), and slow shear-wave parallel to minimum horizontal stress (σ_h). Adopted from (Crampin and Peacock, 2005).....	15
Figure 1.11: In isotropic media, the image point offset for P-S data recorded by a receiver station will vary with reflector depth. The dashed lines represent the ray-path geometrical approximations while the solid line represents the true ray-path. Adopted from (Thomsen, 1999).	16

Figure 2.1: Blackfoot 3C-3D acquisition geometry. Red cross represent shot position, blue triangle represent a receiver station.	20
Figure 2.2: Vertical component processing flow.	22
Figure 2.3: Fold map of vertical component with bin size of 30 x 30 <i>m</i> ²	22
Figure 2.4: The result of initial velocity analysis, prior to residual statics.	23
Figure 2.5: Velocity analysis after residual statics application.	23
Figure 2.6: Pre-stack migrated section of vertical component data.	24
Figure 2.7: Radial component processing flow.	25
Figure 2.8: Fold map of radial component with bin size of 30 x 30 <i>m</i> ²	25
Figure 2.9: Receiver gathers of channel number 10. Top left: H1 (East component). Top right: H2 (North component) Bottom left: Radial component. Bottom right: Transverse component.	26
Figure 2.10: Initial velocity analysis for radial component, prior to residual statics.	27
Figure 2.11: Velocity analysis after residual statics.	27
Figure 2.12: Images of cross-line section of radial component. Top left: Brute stack based on initial velocity analysis. Top right: Stack after applying residual statics and enhanced velocity analysis. Bottom left: Post-stack FK-Stolt migrated section. Bottom right: Pre-stack time migration (Kirchhoff migration).	28
Figure 2.13: Correlation between vertical component migrated image (left) to the radial component migrated image.	30
Figure 3.1: Model parameters. Top: density model. Middle: P-wave velocity model. Bottom: S-wave velocity model.	35
Figure 3.2: Shot gathers of vertical component (right) and radial component (left).	36
Figure 3.3: Results of ERTM using proposed imaging conditions. Top: P-P image. Bottom: P-S image.	37
Figure 3.4: Survey geometry with positions of extracted 2D lines. N-S section highlighted in yellow, E-W section highlighted in green.	39
Figure 3.5: Source wavelet used in migration and its amplitude spectrum (Ricker wavelet).	39
Figure 3.6: Ten receiver-gather records of vertical component (top) and horizontal component (bottom) for N-S 2D line.	41
Figure 3.7: Result of ERTM using both vertical and horizontal components for N-S 2D line. Top: P-P image. Bottom: P-S image.	42
Figure 3.8: Result of ERTM using only the vertical component for N-S 2D line. Top: P-P image Bottom: P-S image Note the high amplitudes in P-S image compared to P-P image.	43
Figure 3.9: Result of ERTM the horizontal component data only for N-S 2D line. Top: P-P image. Bottom: P-S image. Note the low signal in P-P image resulting from horizontal component data.	44
Figure 3.10: Shot-gather records of vertical component (top) and radial component (bottom) for E-W 2D line. Note the poor quality of the radial component data in this section.	45

Figure 3.11: Result of ERTM using only the vertical component for E-W 2D line. Top: P-P image. Bottom: P-S image.	46
Figure 3.12: Result of ERTM the horizontal component data only for E-W 2D line. Top: P-P image. Bottom: P-S image.	47
Figure 3.13: Velocity models of synthetic 2D model used to study the effects of attenuation. Top: P-wave true velocity model. Middle: S-wave true velocity model. Bottom: S-wave velocity model with perturbations to enable distinguishing P-S reflectors on images.	49
Figure 3.14: Migrated images of synthetic model in case of elastic data ($Qp = Qs = 100$). Top: P-P (right) and P-S (left) images using true velocity models (True images). Bottom: P-P (right) and P-S (left) images migrated using perturbed S-wave velocity model (Reference images).	50
Figure 3.15: Migrated images with different attenuation scenarios. From top to bottom; 1 st case ($Qp = Qs = 100$); 2 nd case ($Qp = 100, Qs = 20$); 3 rd case ($Qp = 20, Qs = 100$); 4 th case ($Qp = Qs = 20$). The black arrows refer to effect of attenuation on the migrated images.	51
Figure 4.1: Proposed workflow for automatic migration velocity analysis.	56
Figure 4.2: True velocity models used for creating Gullfaks synthetic dataset. Top: True Vp . Middle: True Vs . Bottom: The near-surface perturbations of Vs model.	58
Figure 4.3: Migration Vs models and related images before and after stack-power optimization. Top left: Initial Vs model. Top right: Initial P-S image. Middle left: Vs model updates after 6 iterations of stack-power optimization. Middle right: Enhanced P-S image using updated Vs . Bottom: Difference between final and initial Vs	59
Figure 4.4: Source wavelet used in migration velocity analysis (Ormsby wavelet).	62
Figure 4.5: Extracted wavelets. Top: From vertical component data. Bottom: from radial component data.	62
Figure 4.6: Initial migration velocity models and migration result for N-S section. Top left: Initial Vp . Top right: Initial P-P image. Bottom left: Initial Vs . Bottom right: Initial P-S image.	63
Figure 4.7: Results obtained from stack-power maximization procedure for N-S section. Top left: Vp model updates after 10 iterations. Top right: Migrated P-P image using updated Vp model. Bottom left: Vs model updates after 9 iterations. Bottom right: Migrated P-S image using updated Vs model.	64
Figure 4.8: Results obtained from stack-power optimization procedure for N-S section where updates are limited to near-surface. Top left: Vp model updates after 10 iterations. Top right: Migrated P-P image using updated Vp model. Bottom left: Vs model updates after 9 iterations. Bottom right: Migrated P-S image using updated Vs model.	65
Figure 4.9: Results obtained from stack-power optimization procedure for E-W section. Top left: Initial Vp model. Top right: Initial P-P image. Bottom left: Resulting Vp updates. Bottom right: Enhanced P-P image.	66
Figure 4.10: Amplitude spectrums of vertical component input data. Left: Raw data. Middle: Applied low frequency data recovery technique. Right: Applied low-frequency coherent noise removal with low cut filter at 5Hz.	68

Figure 4.11: Amplitude spectrums of radial component input data. Left: Raw data. Middle: Applied low-frequency data recovery technique. Right: Applied low-frequency coherent noise removal with low cut filter at 5Hz.	68
Figure 4.12: Results obtained from low-cut filtered data. Top: Vp model updates after 10 iterations (left) and Vs model updates after 7 iterations (right). Middle: Initial P-P image (left) and P-S image (right). Bottom: Updated P-P image (left) and P-S image (right).	69
Figure 4.13: Comparison between the error function numerical values for Vs (left) and Vp (right) in cases of enhanced low frequency data (green curve) and filtering low frequency data (red curve).	70
Figure 4.14: Produced Vp model and updates by 3D implementation of stack-power maximization after 8 iterations.	72
Figure 4.15: 3D display of migrated vertical component data with maximum frequency of 20 Hz. Top: Initial P-P image. Bottom: Enhanced P-P image after 8 iterations.	73
Figure 4.16: Error function numerical values for Vp 3D inversion.	74
Figure 5.1: Workflow of P-P and P-S images co-depthing procedure.	80
Figure 5.2: Migration velocity models and produced initial images. Top left: Vp model. Top right: Vs initial model. Bottom left: P-P image. Bottom right: P-S initial image.	82
Figure 5.3: Key reflectors co-depthing procedure. Top: Target P-S reflector image produced using P-P Born modeled data. Middle: Initial forward modeled P-S reflector image showing inconsistent depth. Bottom: Updated P-S reflector image using target image fitting procedure after iterations.	83
Figure 5.4: True Vs model (left) and updated Vs model (right) after 6 iterations using target image fitting procedure.	84
Figure 5.5: Updated P-S image after co-depthing procedure.	84
Figure 5.6: Registration of 4 key reflectors on P-P image (left) and P-S image (right)	86
Figure 5.7: Results of target image fitting procedure. Top left: Produced Vs model after 10 iterations of target image fitting for the low frequency model. Top right: Vs model updates after 10 iterations of target image fitting for the low frequency model. Bottom left: Produced Vs model after 3 iterations of target image fitting for the high frequency model. Bottom right: Vs model updates after 3 iterations of target image fitting for the high frequency model. Note the distribution of the updates over the model edges with positive values in order to compensate for velocity errors produced in stack-power procedure due to poor illumination.	87
Figure 5.8: Produced P-S images. Top: Initial P-S image migrated using Vs model updated by stack-power maximization. Middle: Produced P-S image using Vs updated by target image fitting for the low frequency model. Bottom: Produced P-S image using Vs updated by target image fitting for the high frequency model.	88
Figure 5.9: Target image fitting function numerical values for low frequency model (left) and high frequency model (right).	89
Figure 5.10: Final Vs model updates after 10 iterations of stack-power optimization and the corresponding P-S migrated image.	89

Figure 5.11: Final stack-power maximization error function values..... 90
Figure 5.12: Comparison between initial V_s/V_p ratio (left) and final V_s/V_p ratio (right). 91

List of Equations

1.1 Hooke's law	4
1.2 Hooke's law expressed by the Lamé coefficients.....	4
1.3 Newton's second law	4
1.4 The vector form of elastic wave equation.....	4
1.5 Wave equation for P-wave propagation.....	5
1.6 P-wave propagation velocity.....	5
1.7 Wave equation for S-wave propagation.....	5
1.8 S-wave propagation	5
3.1 Imaging condition for P-P image.....	33
3.2 Imaging condition for P-S image.....	33
3.3 Displacement vector u_i^s computed through a solution to the density normalized elastic wave equation.....	33
3.4 Displacement vector u_i^r computed through a solution to the density normalized elastic wave equation.....	33
4.1 Stack-power maximization objective function	55
5.1 Target image fitting objective function.....	78
5.2 Forward modeling equation to create single scattering 3C P-S data	79
5.3 Born source for P-S data calculation	79

1 Introduction

1.1 Background

Exploration seismology has been significantly contributing to successful hydrocarbon exploration and production. Along the continuous evolution of exploration seismology, the main objective has been producing better subsurface seismic images that lead to lower risk exploration and enhanced production. With the ongoing depletion of resources and less plain prospects, the hydrocarbon exploration becomes progressively challenging. That drives the exploration momentum toward more complex and risky environments than ever before, which requires advanced techniques that can mitigate such challenges. These techniques are mainly focused on acquiring higher-fidelity data, making more accurate approximation of seismic wave propagation and unambiguously correlating the recorded data to the subsurface physical properties.

Most of the seismic exploration techniques were developed assuming an acoustic nature of subsurface, considering that Earth propagates only compressional waves. Despite the simplicity and practicality of such assumption, it is not realistic. The elastic nature of Earth materials allow compressional and shear wave propagation. Adding to that, compressional energy gets mode-converted into shear energy upon reflection from a boundary at non-zero angles of incidence (Aki and Richards, 1980). This mode converted wave helps in accurate characterization of wave propagation, resolving a realistic subsurface image.

Advances in acquisition of converted shear-wave (P-S) data through multi-component seismic recording enabled imaging converted waves, respecting both the elastic nature of Earth materials and the vector nature of the recorded seismic waves. P-S data play a complementary role in hydrocarbon seismic exploration where the primary method of conventional compressional-wave (P-P) data has limited capabilities. P-S data is successfully used for reservoir monitoring, prediction of fluid and lithology (Stewart et al., 2003) and producing significantly better images through gas zones (Granli et al., 1999) and beneath high velocity layers such as salt (Kendall et al., 1998).

P-S data require more demanding processing and sophisticated imaging techniques than conventional P-P data, as a result of the asymmetry of P-S ray-path and the vector nature of the recorded seismic wave-field. The work done by Garotta (1984), Tessmer and Behle (1988), Slotboom (1990) and Harrison

(1992) established the bases for what became a conventional workflow for P-S data processing, and provided insight into the capabilities and challenges of converted wave data. Conventional processing of P-S data requires special analyses as horizontal components rotation shear-wave splitting analysis, shear-wave receiver statics, special binning as common conversion point (CCP), non-hyperbolic velocity analysis and NMO correction. These conventional processing techniques are based on approximations that are not physically accurate most of the time, which urge the need for accurate modeling of shear-wave velocity and elastic imaging algorithm that can overcome the shortcomings following the conventional approximations.

1.2 Thesis objectives

In this thesis we will overview the challenges related to converted wave data processing and imaging in isotropic media and introduce a novel workflow for accurate depth imaging and velocity analysis for multi-component data. The main objective is producing optimized subsurface images from multi-component data. The improvement of converted wave imaging can be accomplished by satisfying 2 main criteria: Firstly, to accurately image P-P and P-S scattering events using all receiver components, avoiding cross-talking of different wave-modes, with no need for polarity reversal corrections. Secondly, to estimate the accurate velocities which result in coherent and depth consistent P-P and P-S images. The workflow is based on elastic reverse-time migration (ERTM) as a robust migration algorithm that provide high quality images in areas with complicated structure and complex velocity parameters.

We propose and practically test novel imaging conditions in order to overcome the polarity reversal problem and investigate the cross-talking between different wave-modes. We apply automatic wave equation migration velocity analysis (WEMVA) techniques based on stack-power optimization and target image fitting procedures, in order to produce the optimal models of compressional wave velocity (V_p) and shear wave velocity (V_s) that result in coherent and depth consistent images.

1.3 Thesis outline

This thesis consists of six chapters including the introduction chapter. Each chapter has its own introduction and discussion. In the introduction chapter we will have an overview of converted waves characteristics and discuss the relevant theoretical background of multi-component data conventional processing and imaging techniques, focusing on the related challenges.

In the second chapter we show a fast-track implementation of conventional multi-component data processing and pre-stack Kirchhoff time migration. The field dataset used in this study is the Blackfoot 3D-3C dataset available for purchase at the Society of Exploration Geophysicists bookstore. The main objective for this chapter is to get hands-on experience of the challenges and problems following the conventional techniques, and to have an idea about the expected image of Blackfoot dataset. The software used in processing the data is VISTA® seismic data processing.

The third chapter discusses imaging multi-component data using elastic reverse-time migration in isotropic media. We introduce new imaging conditions, where the main objective is to image P-P and P-S scattering events using all receiver components with no need for polarity reversal correction. The approach is tested on 2D synthetics and field dataset. The results are analyzed and further assessment of geophone coupling and attenuation (Q) effects are discussed. We used Madagascar software package (Fomel et al., 2013) for the work done in this chapter and the following ones.

In the fourth chapter we introduce wave equation migration velocity analysis technique based on elastic reverse-time migration. The migrated images are used in an automatic stack-power maximization procedure to estimate enhanced (V_p) and (V_s) migration velocity models that produce focused and coherent images. The method is tested on the same 2D synthetics and field dataset used in the previous chapter. Adding to that a 3D implementation for (V_p) inversion was successfully achieved. Part of this work has been presented at the 79th EAGE Conference and Exhibition in Paris under title “Elastic reverse-time migration and velocity analysis using multi-component geophone data”.

In the fifth chapter we tackle the problem of depth consistency between P-P and P-S images constructed using elastic reverse-time migration and velocity models produced from stack-power maximization in the previous chapter. We introduce a tomographic co-depthing method based on manual interpretation of key reflectors of the initial P-P and P-S images and then automatically determining the velocities that will optimally match these reflectors in depth. In this process we use a novel Born modeling/demigration method to create synthetic single scattering P-S data from the interpreted reflector models. The work discussed in this chapter will be presented at the 87th SEG annual meeting in Houston under title “Tomographic co-depthing of reflectors in P-P and P-S elastic reverse-time migrated images”.

1.4 Wave propagation in elastic isotropic media

In this section we briefly discuss the mathematical background of wave equation that describes the wave propagation in elastic isotropic media. A medium is considered elastic when it returns to its original non-deformed state after external forces are removed from the medium. Linear elastic material is defined as one in which each component of stress σ_{ij} is linearly dependent upon every component of strain ϵ_{kl} .

Stress σ and strain ϵ are related by Hooke's law:

$$\sigma_{ij} = - \sum_{k=1}^3 \sum_{l=1}^3 c_{ijkl} \epsilon_{kl} \quad 1.1$$

where c corresponds to the elastic stiffness tensor and $i, j = 1, 2, 3$.

Equation 1.1 can be expressed by the Lamé coefficients λ and μ as seen in equation 1.2, where μ is also known as the shear modulus or rigidity.

$$\sigma_{ij} = \lambda \delta_{ij} \epsilon_{kk} + 2\mu \epsilon_{ij} \quad 1.2$$

Newton's second law gives the equation of motion for wave propagation:

$$\rho \frac{\partial^2 u_i}{\partial t^2} = \partial_j \sigma_{ij} \quad 1.3$$

where ρ is the mass density t is time and u is the displacement vector.

Using equations 1.2 and 1.3, we can derive the equation of motion in terms of displacement and stress.

The vector form of elastic wave equation may be written as:

$$\rho \frac{\partial^2 u}{\partial t^2} = (\lambda + 2\mu) \nabla(\nabla \cdot u) - \mu \nabla \times (\nabla \times u) \quad 1.4$$

From the equation 1.4 it is possible to derive the wave equation for both P-wave and S-wave propagation.

Taking the divergence of the equation of motion 1.4, and applying vector identities, we obtain the wave equation for P-wave propagation, as equation 1.5.

$$\nabla^2(\nabla \cdot \mathbf{u}) = \left(\frac{\rho}{\lambda + 2\mu}\right) \frac{\partial^2}{\partial t^2}(\nabla \cdot \mathbf{u}) \quad 1.5$$

P-wave propagation velocity can be described as following:

$$v_p^2 = \frac{\lambda + 2\mu}{\rho} \quad 1.6$$

Taking the curl of the equation of motion 1.4 and applying vector identities, we obtain the wave equation for S-wave propagation as equation 1.7.

$$\frac{\rho}{\mu} \frac{\partial^2(\nabla \times \mathbf{u})}{\partial t^2} = \nabla^2(\nabla \times \mathbf{u}) \quad 1.7$$

S-wave propagation velocity can be described as following:

$$v_s^2 = \frac{\mu}{\rho} \quad 1.8$$

Equation 1.6 shows the dependency of shear velocity on rigidity μ .

1.5 Converted waves and multi-component data

1.5.1 Overview

Elastic conversion of energy occurs at every discontinuity within an elastic body with non-zero angles of incidence. Part of the compressional P-wave energy converts to shear S-wave and vice versa, resulting in converted wave-modes P-S and S-P (Aki and Richards, 1980). In elastic isotropic media there are 4 main possible single scattering reflection wave-modes P-P, P-S, S-P and S-S. There are other possible types of energy conversion that are transmitted or multiple converted with negligible amplitudes compared to reflection converted modes (Rodriguez Suarez, 2000).

The term converted wave in seismic exploration is referring to the particular conversion of P-wave propagating downward to an S-wave at the deepest point of penetration and reflected upward as P-S wave-mode (Stewart et al., 2002). P-S waves have a polarization vector transverse to their propagation, where particle motion is perpendicular to propagation direction. Figure 1.1 shows the senses of particle motion and the difference in reflection and transmission angles of compressional and shear waves.

Advances in data acquisition through multi-component receivers propelled the development of P-S data processing and imaging applications. A big step in this development was implementing ocean bottom seismic technology (OBS) in marine data acquisition. As seen in equation 1.8, shear-waves cannot travel through fluids as it depends on physical property of rigidity. Accordingly, it cannot be acquired by conventional streamer techniques. Figure 1.2 describes ocean bottom cable (OBC) acquisition technique, where cables of four-component-receiver stations are deployed over the sea bottom, each station is composed of three orthogonally oriented geophones (horizontal X , horizontal Y , vertical Z) and one hydrophone (P).

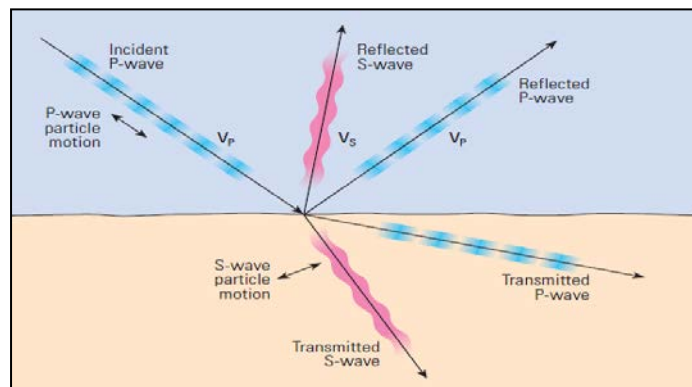


Figure 1.1: Wave-mode conversion with particle motion and propagation directions of compressional and shear waves. Adapted from (Barkved et al., 2004)

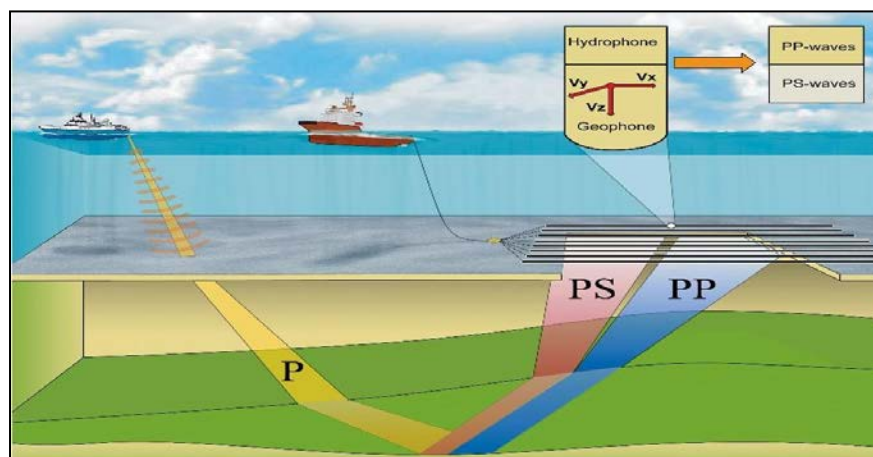


Figure 1.2: Ocean bottom cable seismic acquisition. P-S data recorded by a receiver station will represent a different spatial subsurface position than P-P data. Adapted from (Ikelle and Amundsen, 2005)

The unique characteristics of P-S waves enable retrieving more accurate subsurface information, and made it play a complementary role in hydrocarbon seismic exploration where the primary method of conventional P-P data has limited capabilities. However, these unique characteristics made P-S data processing and imaging very challenging in practice and more sophisticated than P-P data.

P-S data provide an image constrained to the rock properties. The independency of fluid content gave P-S data the advantage of imaging through gas zones (Granli et al., 1999) as shown in Figure 1.3. It also enabled calibrating hydrocarbon indicators resulting from fluid effects on P-P images, such as flat and bright spots. Figure 1.4 shows an example for P-P image with flat spot and the related P-S image which is not affected by the fluid change, validating the presence of flat spot.

In reservoirs with low P-wave impedance contrast, P-S images can produce accurate maps of reservoir architecture which leads to enhanced reservoirs development and production (MacLeod et al., 1999). In Figure 1.5 we notice how P-S data can significantly improve the reservoir interpretation in comparison to conventional P-P streamer data, which reduce the risk of placing production and development wells in inaccurate position. Adding to that, the accurate estimation of S-wave velocity (V_s) and (V_p/V_s) ratio from which Poisson's ratio can be calculated, leads to enhanced lithology identification (Stewart et al., 2003).

The lower velocity of shear waves results in smaller reflection angle than the angle of incidence which is described by Snell's law. That leads to asymmetric ray-path of P-S data propagation. Due to the asymmetry of P-S ray-path, recorded P-S data by a receiver will represent the conversion point (CP) of the reflector, which is geometrically closer to the receiver than the mid-point (MP) represented by P-P data as demonstrated in Figure 1.6. That gives rise to recording spatially different data by the same receiver station, which requires different binning techniques for P-S data than the ones used for P-P data. The asymmetric travel paths of P-S data can allow a better illumination of subsalt targets than P-wave travel paths allow (Kendall et al., 1998). Adding to that, P-S waves have shorter wavelength compared to P-P waves. The shorter wavelength P-S waves have, can theoretically produce higher resolution data compared to P-P. However, in practice P-S waves suffer stronger attenuation than P-P (Kristensen and Hovem, 1991; Bale and Stewart, 2002).

Correlating P-P and P-S data in time domain is difficult, due to the longer propagation time P-S waves take compared to P-P data. Moreover, the characteristics of P-S reflectivity are different from P-P,

where the same subsurface event can have different response on both data. Aki and Richards (1980) described the P-S reflectivity in their approximation to Zoeppritz equations as a function of offset. Figure 1.7 illustrates how reflection coefficients for P-P and P-S waves vary with offset, indicating the conversion to P-S energy with P-wave angle of incident.

These advantages and the challenging nature of converted waves provided sheer motivation for number of research groups to further develop the technology. The work done by Garotta (1985), Tessmer and Behle (1988), Slotboom (1990) and Harrison (1992) established the bases for what became conventional workflows for P-S data processing, and provided an early insight into the capabilities and challenges of converted wave data. Most of P-S data processing techniques are based on assumptions which might seem practically sufficient, but not physically accurate. In addition to that, conventional P-S imaging techniques are based on approximations borrowed from acoustic wave equation imaging algorithm that do not respect the vector nature of elastic waves. In the following section we will closely consider these assumptions in order to better understand the challenges facing converted waves processing and imaging.

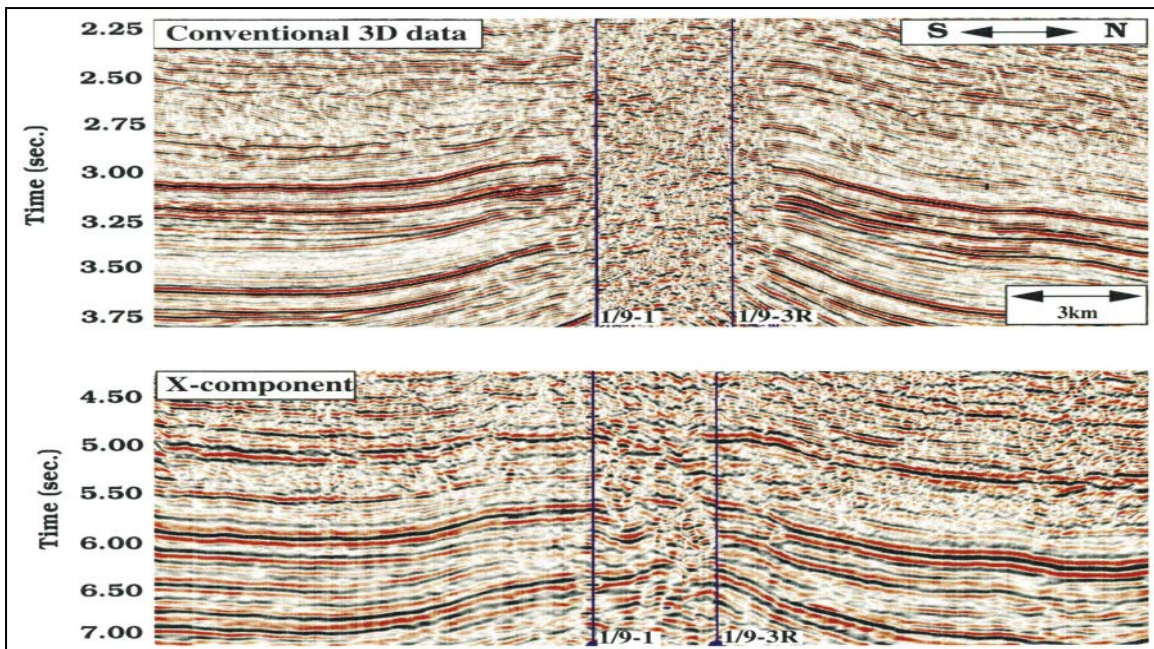


Figure 1.3: Gas chimney effect over Ekofisk field. Conventional P-P image from 3D streamer data compared to the enhanced P-S image using only the horizontal (X) component from OBC data. Adopted from (Granli et al., 1999)

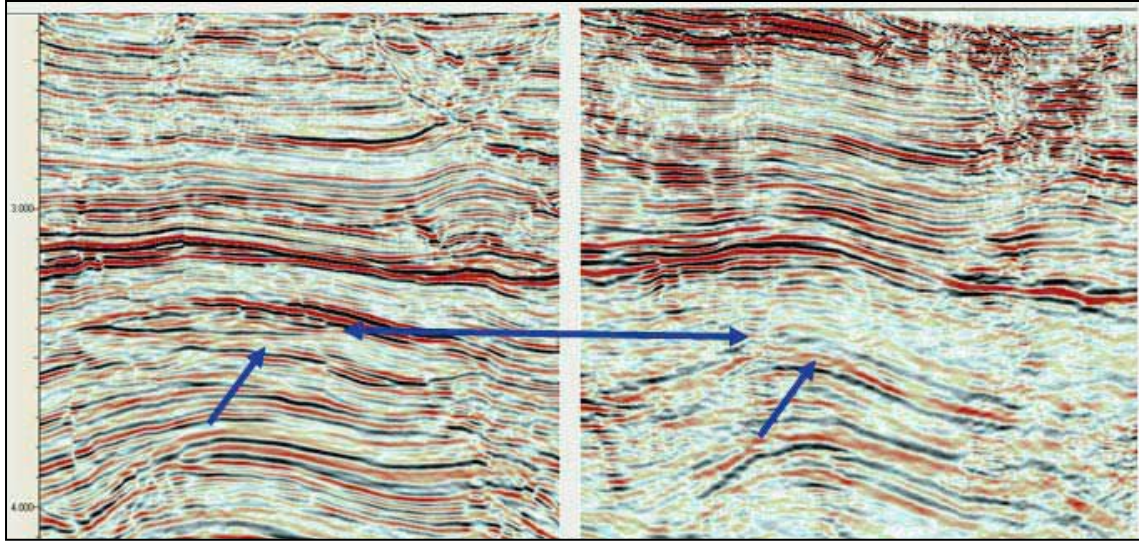


Figure 1.4: P-P image (left) showing flat spot and associated gas cap above it, and the absence of the feature in the related P-S image (right) confirming the fluid related anomaly. From (Cafarelli et al., 2006)

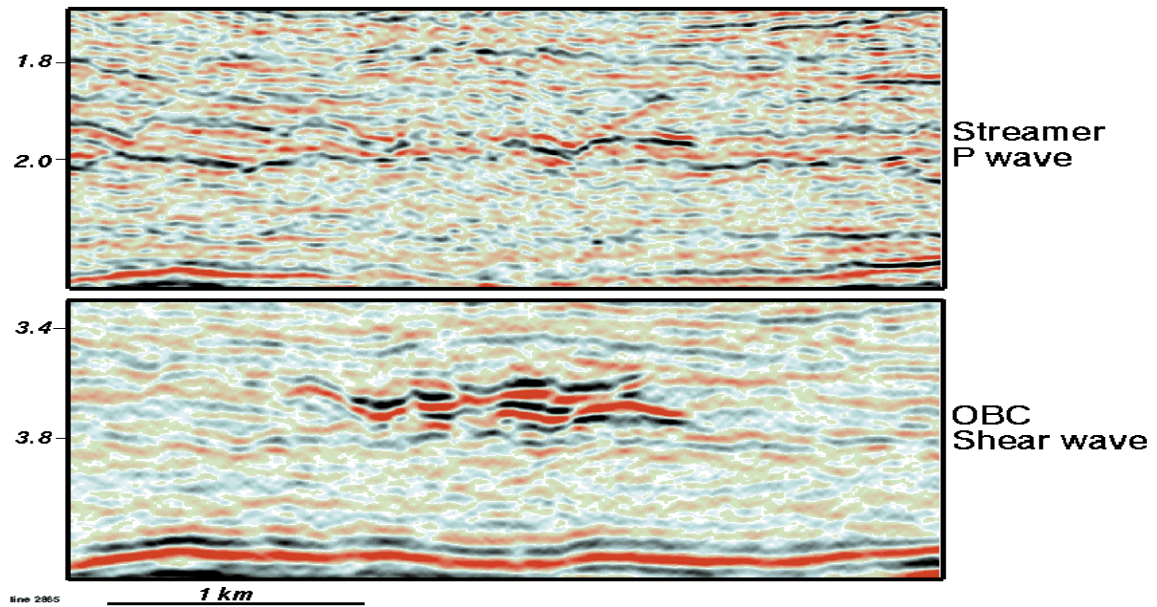


Figure 1.5: An example from Alba field showing the improved reservoir image using converted waves, where the top of reservoir is easily identified leading to efficient well placement. From (MacLeod et al., 1999)

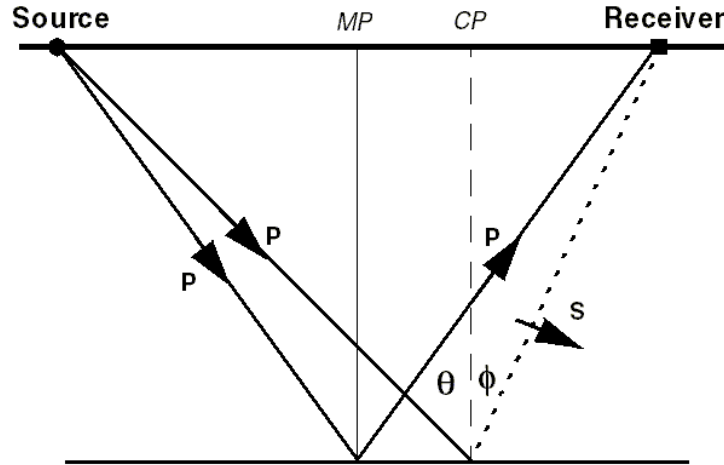


Figure 1.6: Geometrical illustration of P-P reflection data at its midpoint (MP) and P-S reflection data at its conversion point (CP). The P-wave angle of incidence is given by θ and S-wave angle of reflection is given by ϕ . Adopted from (Stewart et al., 2002)

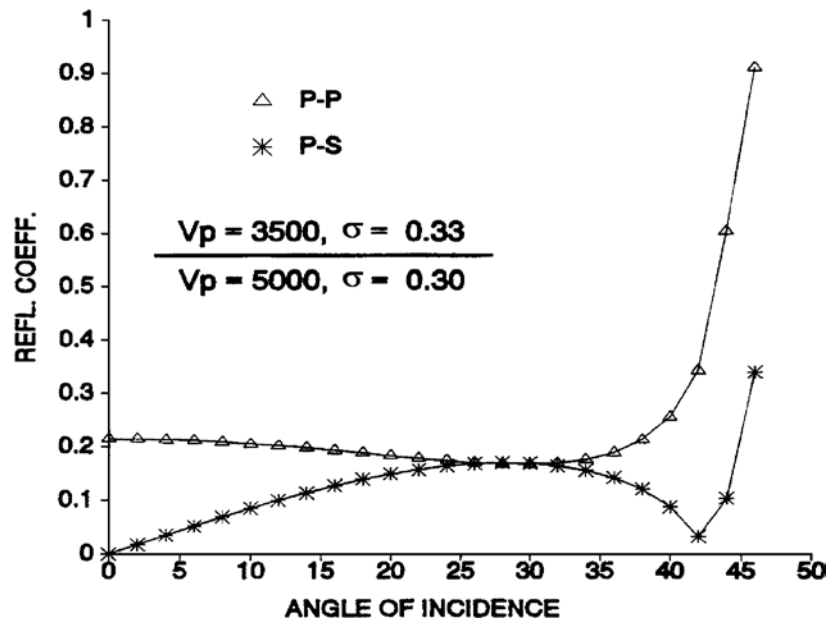


Figure 1.7: P-P and P-S reflection coefficients as a function of P-wave angle of incidence. The S-wave velocities for the upper and lower layers are 1750 m/s and 2650 m/s, respectively. Density is constant. Adopted from (Stewart et al., 2002)

1.5.2 Challenges

1.5.2.1 Acquisition and pre-processing

The main advantage of multi-component data acquisition is the ability to record actual vector information (vector fidelity), using at least three mutually-perpendicular receivers, one vertical (Z) receiver and two horizontal (X, Y) orthogonally deployed receivers. The two horizontal components are usually oriented in acquisition coordinate system of in-line and cross-line, with notations of H_1 and H_2 , respectively.

An assumption that has been followed for a long time in dealing with multi-component data is considering the vertical component as the only representation of P-P wave record, while the orthogonal horizontal components represent the P-S wave record. This assumption ignores the vector nature of the elastic waves recorded, and the fact that all the wave-modes are recorded on all the components in a certain degree, especially with wide angles. Based on this assumption, each wave-mode can be separated directly from receiver components and processed independently to produce a scalar image.

1.5.2.1.1 Geophone coupling and vector fidelity

Adequate coupling is vital for P-S data recording. Coupling quality controls the accuracy with which the receivers measure the actual wave-field, affecting the spectral response of the recorded signal component in amplitude and phase. Accordingly, bad coupling can have crucial implications on the vector fidelity of the recorded multi-component data (Tree, 1999). If the geophone response differs from one component to another, data from the components cannot be combined optimally (Stewart et al., 2002). Different approaches were investigated in order to balance the geophone response, some of this approaches were directed toward the acquisition design and geophone specifications (Krohn, 1984; Cieslewicz, 1999; Bland et al., 2004), others were directed toward a processing solution approach (Gaiser, 1998; Gaiser et al., 2000).

1.5.2.1.2 Receiver orientation and data rotation

The transverse polarization vector of P-S waves particle motion to their propagation vector requires knowledge of acquisition coordinate system. Horizontal components are addressed as radial and transverse components (the processing coordinate system) based on the geometrical position in respect to the source-receiver azimuth. The radial component represents the horizontal particle motion in-line with source-receiver plane, while the transverse component represents the data recorded orthogonally to the

radial. In this case, accurate receiver orientation data is required to successfully separate the radial and transverse components and to obtain the correct recorded data polarity for P-SV and P-SH waves..

Synthetic example of multi-component geophones response in isotropic media is shown in Figure 1.8 and Figure 1.9. This example is a result of finite difference forward modeling for a survey consisting of one shot at the center and number of receivers deployed in 3D grid array with 20 meters receiver-station spacing. The horizontal components are oriented according to in-line direction (X -component) and cross-line direction (Y -component). In Figure 1.8 we show in-line and cross-line records with no azimuth to the source. In such case, X -component will represent the radial component on the in-line, while Y -component will represent the radial component on the cross-line. It is obvious how the transverse component show no data record. The vertical component is irrelevant to the receiver orientation and shows data recorded on in-line and cross-line. In Figure 1.9 the in-line and cross-line are positioned with variable azimuth to the source. The variation in source azimuth with receiver position results in recording the wave-field energy on both horizontal components whether on in-line or cross-line records. It is also noticed how the recorded data polarity changes in respect to source position. In addition to that, by comparing the arrival time of the data recorded by the vertical component and that recorded by horizontal components we can distinguish between P-P and P-S modes that are present in all the components. This example showed the need for data rotation to correct the data polarity and convert it from acquisition coordinate system (X, Y) to the processing coordinate system (Radial, Transverse). It also showed how the energy of both P-P and P-S wave-modes can be detected by all the geophone components.

1.5.2.1.3 Anisotropy and shear wave splitting

In case of anisotropic media with a preferential direction of stress (polar anisotropy), the converted S-waves will split into fast ($S1$) and slow ($S2$) shear waves which are polarized parallel and perpendicular to the anisotropy plane respectively (Figure 1.10). The analysis of shear wave splitting into fast and slow orthogonal components provides information on the subsurface azimuthal anisotropy. The measurement of S-wave splitting has been used successfully to investigate the fractures in reservoirs. Crampin and Peacock (2005) provided a thorough review on shear wave splitting and its applications. In such anisotropic case, instead of recording one converted wave-mode, the receivers record the fast P-S1 and slow P-S2 wave-modes. This issue has been addressed by several authors (e.g., Alford, 1986; Harrison, 1992; Lou et al., 2000) in order to provide sufficient shear splitting analysis techniques that can accurately separate the two events.

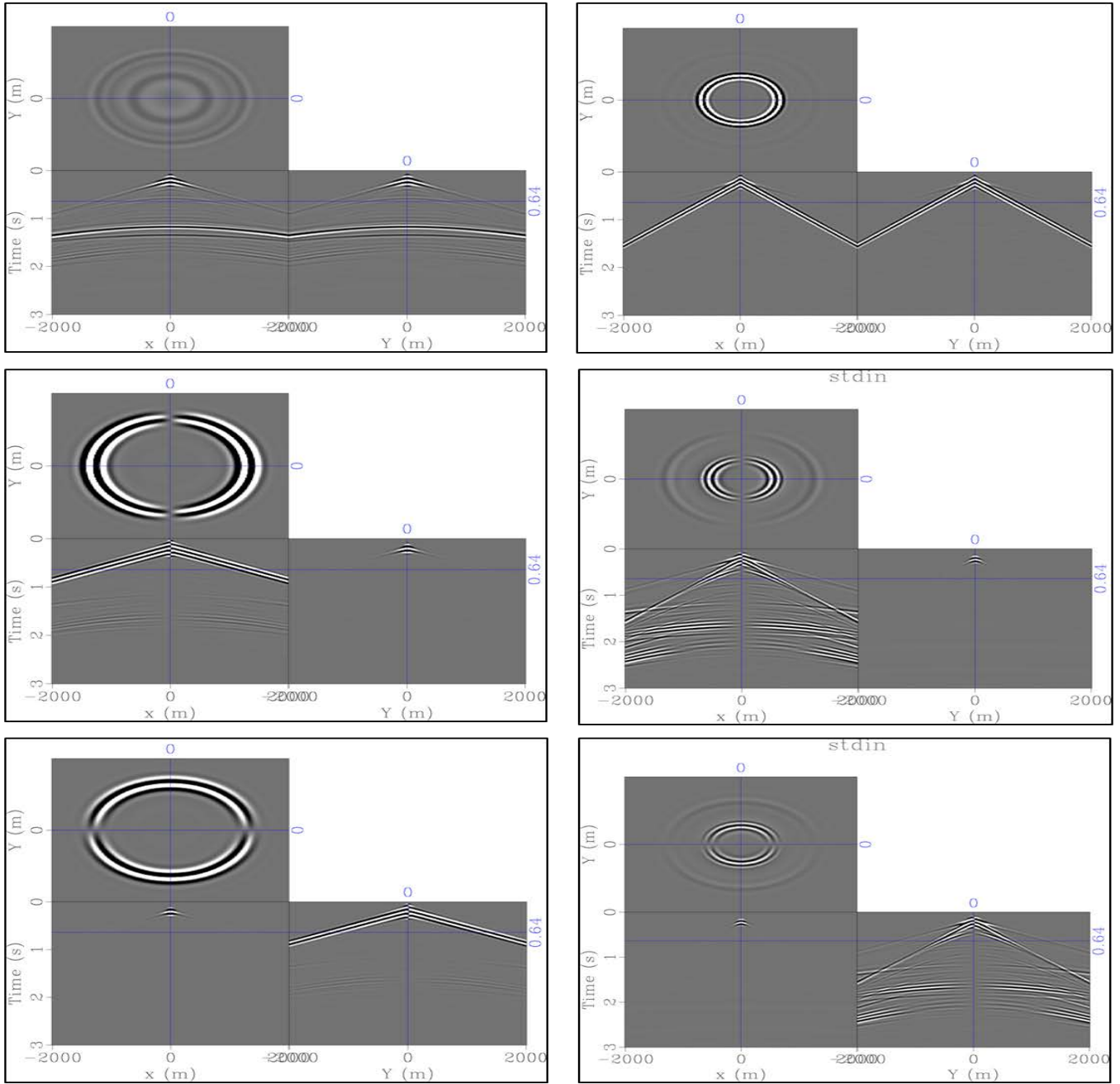


Figure 1.8: Result of finite-difference forward modeling of three-component geophones response to pressure source (left-side) and to explosive source (right-side). The geophones are oriented according to in-line (X-component) and cross-line (Y-component) directions in plane with the source.

Top figures represent data recorded by vertical (Z-component).

Middle figures represent data recorded by horizontal (X-component).

Bottom figures represent data recorded by horizontal (Y-component).

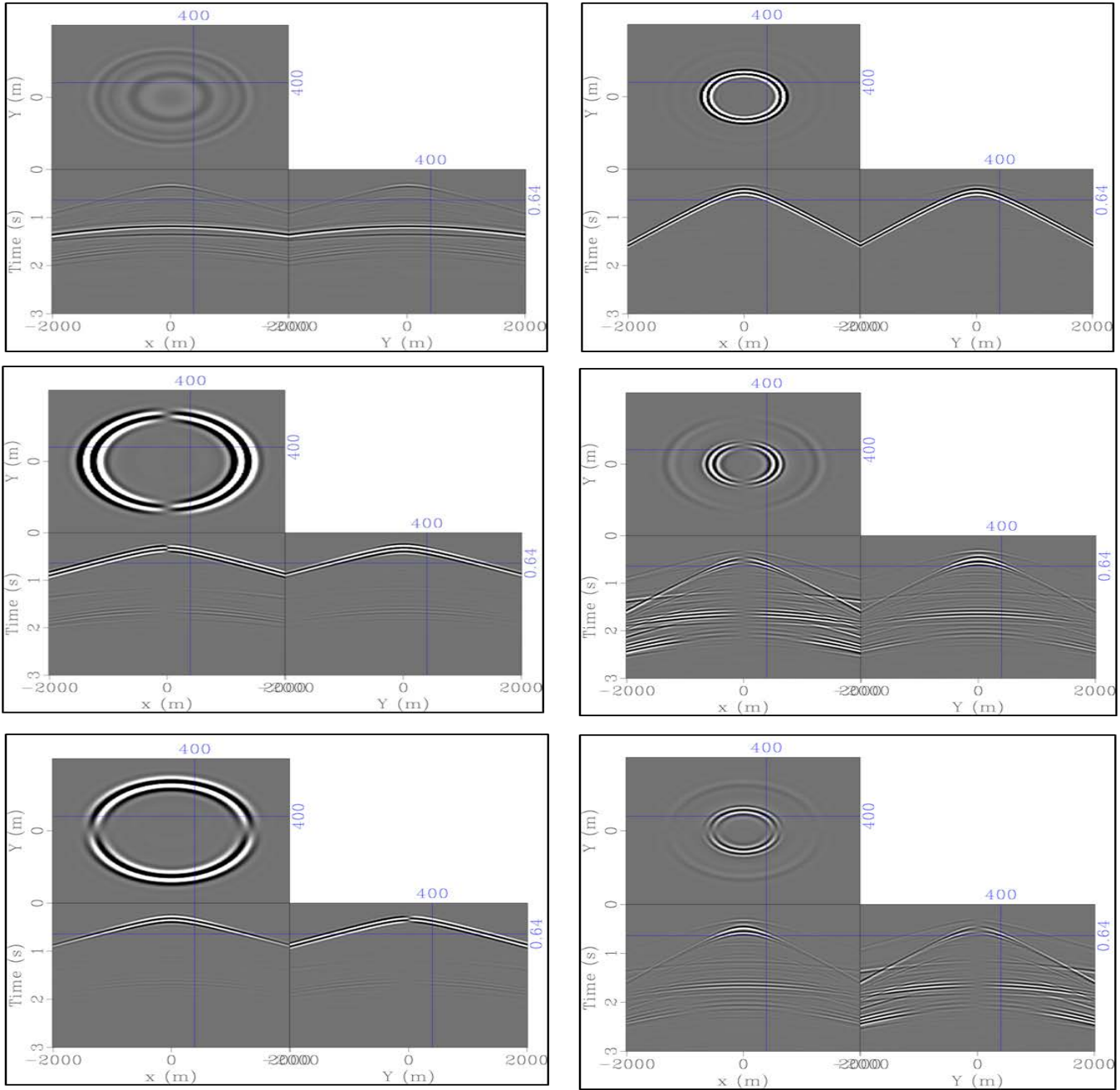


Figure 1.9: Result of finite-difference forward modeling of three-component geophones response to pressure source (left-side) and to explosive source (right-side) in isotropic media. The geophones are oriented according to in-line (X-component) and cross-line (Y-component) directions with variable source-receiver azimuth.

- Top figures represent data recorded by vertical (Z-component).
- Middle figures represent data recorded by horizontal (X-component).
- Bottom figures represent data recorded by horizontal (Y-component).

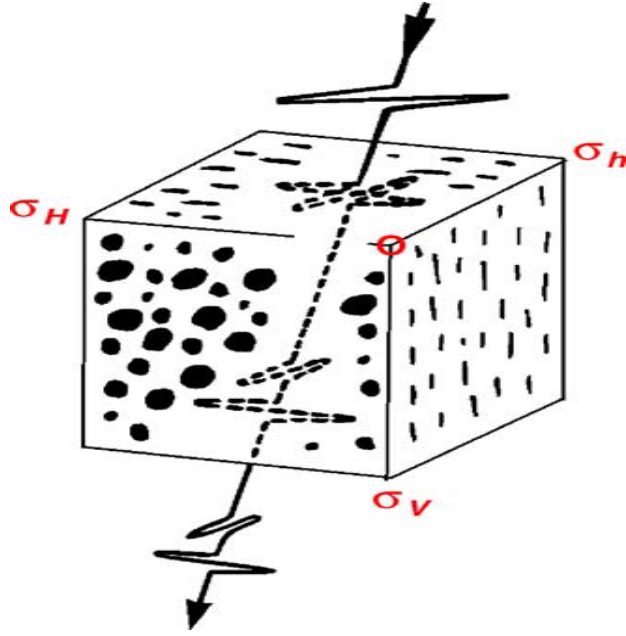


Figure 1.10: Shear wave splitting to fast shear-wave parallel to maximum horizontal stress (σ_H), and slow shear-wave parallel to minimum horizontal stress (σ_h). Adopted from (Crampin and Peacock, 2005).

1.5.2.2 Processing, velocity analysis and imaging

P-S data processing requires physical assumptions that are more realistic than the geometrical assumptions used for P-P data processing (Thomsen, 1999; Stewart et al., 2002). The offset of the conversion point, the required moveout correction which is no longer hyperbolic, and the S-wave static correction are all dependant on the geophysical elastic parameters of the media as (V_p) and (V_s) velocity fields. At the same time, deducing such physical properties of the media is depending on the accuracy of data processing and velocity analysis (Garotta et al., 2000). This mutual dependency problem resulted in the principle difficulties facing P-S data processing and imaging. In this section we will review the conventional approximations commonly used in P-S data processing and the related limitations.

1.5.2.2.1 Binning

Due to the asymmetric ray-path of P-S waves, the P-S data recorded by a receiver station will be represented by the conversion point (CP) on the reflector, which is shifted from the mid-point (MP) represented by P-P data for the same reflector, as shown in Figure 1.6. Adding to that, the conversion point position is not just a function of source-receiver offset and V_p/V_s velocity ratio, but also it varies with the reflector depth. That adds more complications in spatially binning the recorded data (Tessmer and

Behle, 1988). Figure 1.11 demonstrate the effect of reflector depth on the conversion point positioning, with the main geometrical approximations used to solve this problem. Asymptotic binning (ACP) is the most basic P-S data binning, based on average V_p/V_s ratio (Garotta, 1985; Harrison, 1992). It can be seen that ACP binning is less accurate with shallow depths. Another more accurate technique is the depth-variant common conversion point (CCP) binning method, which can be applied with different geometrical approximations (Tessmer and Behle, 1988; Eaton et al., 1990; Thomsen, 1999).

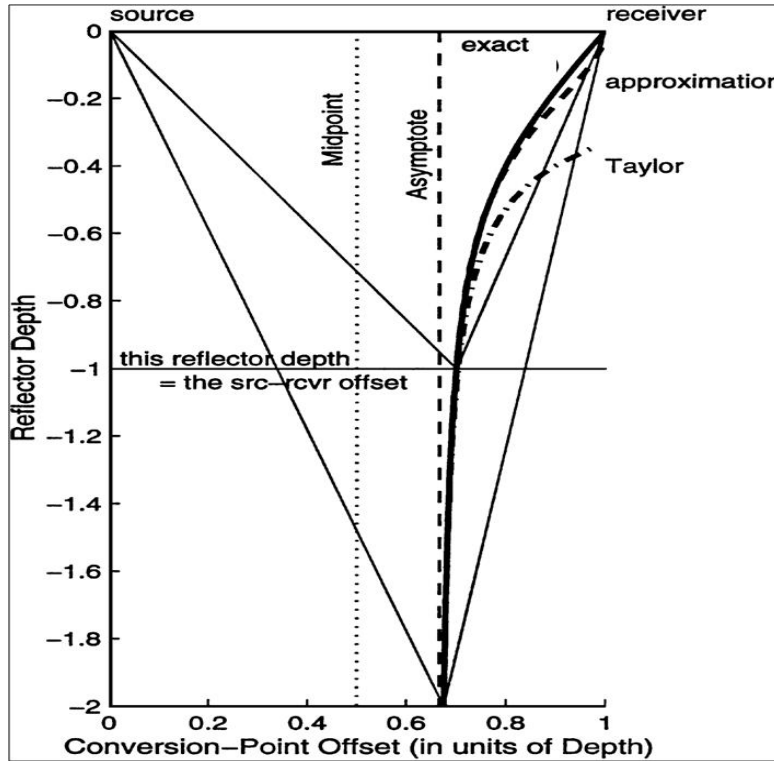


Figure 1.11: In isotropic media, the image point offset for P-S data recorded by a receiver station will vary with reflector depth. The dashed lines represent the ray-path geometrical approximations while the solid line represents the true ray-path. Adopted from (Thomsen, 1999).

1.5.2.2.2 Static corrections and near-surface low velocity layer

Static effects are represented by the difference in reflections arrival time due to near-surface complexities. The conventional procedure followed in P-S data static correction is to first obtain the source static corrections calculated for P-P data, and then the receiver statics can be estimated. Lack of near-surface S-wave velocity is a fundamental difficulty when processing converted P-S data. Receiver elevation statics suffer from the high uncertainty of the S-wave velocity and the thickness of the near-surface model. Several techniques were developed in order to solve the receiver statics problem. Most of the

developed techniques for solving receiver statics problem are based on interpretational approach. Refraction statics technique based on first arrival time picking is effective for P-wave statics but less common for S-wave statics, as it is difficult to pick S-wave refractions (Vaezi and DeMeersman, 2014). Other techniques try to match structure features of P-S data to P-P data on receiver stacks or even to assess the coherency of common receivers gathers, based on the assumption that all the PS-wave events of a common receiver gather are affected by the same S-wave statics (Guevara et al., 2015). Surface consistent residual statics techniques such as stack-power approach (Ronen and Claerbout, 1985; Eaton et al., 1991) can provide better results. However, great caution should be exercised as residual statics algorithms often produce numerous cycle skips when attempting to resolve very large statics (Cary and Eaton, 1993). In addition to that, the uncertainty inherited from the P-wave and S-wave elevation and/or refraction statics still can affect the efficiency of residual statics techniques.

It is important to take into consideration that applying P-wave statics on the vertical component and applying S-wave statics on horizontal components will result in different time shifts between the different components. That will definitely distort the elastic waveform which is recorded by all the components as discussed before. Another undesirable effect of the near-surface layer is attenuation. As mentioned before, P-S waves suffer stronger attenuation than P-P (Kristensen and Hovem, 1991; Bale and Stewart, 2002). Attenuation analysis has been a limitation in P-S data processing that needs to be addressed, where seismic quality factor (Q) modeling will improve the data quality and help in accurately process the data (Stewart et al., 2002). The attenuation effect on elastic wave-modes is investigated in chapter three of this thesis.

1.5.2.2.3 Velocity analysis and non-hyperbolic NMO

As mentioned earlier in binning section, P-S conversion point position is a function of source-receiver offset, reflector depth and V_p/V_s velocity ratio. That makes procedures used with P-P data for velocity analysis and hyperbolic moveout inapplicable. The accuracy of P-S wave velocity analysis is sensitive toward the binning method used to generate conversion point, the initial V_p/V_s ratio used in binning and the accuracy of static corrections applied. All this error-prone approximations make conventional P-S wave velocity analysis a challenging indirect process. In conventional way, velocity analysis for P-S data is usually done by assuming an initial V_p/V_s ratio to bin the data according to it. After binning, velocity analysis can be initiated to pick a reasonable stacking P-S wave velocity that is then used for better binning and static correction of the data. Other rounds of velocity analysis should be done till reach-

ing a reasonable results. The resulting velocity model represents the P-S wave stacking velocity, which can be used with the P-wave velocity information to deduce S-wave velocity. Stewart and Ferguson (1996) presented a method to find an S-wave interval velocity from P-S stacking velocities using the Dix assumption that the stacking velocity is equal to the (rms) velocity. Another technique to obtain V_p/V_s velocity ratio is by correlating key events time on P-P and P-S migrated images, which can be highly uncertain. Moreover, the velocity analysis is affected by the moveout correction technique used. Solution for the problem of moveout correction for P-S data in isotropic media was presented by Slotboom (1990) where he derived a shifted hyperbola equation for moveout correction that can correct the offset travel times more accurately. Alkhalifah (1997) and Thomsen (1999) addressed the issue of velocity analysis using non-hyperbolic moveout in anisotropic media. These difficulties and uncertainties of the approximations used in conventional P-S data velocity analysis impel the need for a velocity analysis technique that accurately respects the physical properties of the subsurface.

1.5.2.2.4 Imaging

Imaging multi-component data is an active research area and still developing. Imaging of multi-component data depend on the fidelity of recorded data and the accuracy of (V_p) and (V_s) velocity models. We have discussed in this chapter how difficult it is to obtain such information using conventional techniques. Vector wave-field separation to P-P and P-S wave-modes has been one of the main challenges in multi-component data imaging. For isotropic media, the most straightforward way to image multi-component data is based on the assumption that P-P and P-S wave modes are represented by the recorded vertical and radial-horizontal components, where each mode can be imaged independently with procedures borrowed from acoustic wave equation imaging algorithms. This approach is not usually correct due to the vector nature of elastic waves (Etgen, 1988; Zhe and Greenhalgh, 1997), where the elastic wave-fields are recorded by the different receiver components.

Adding to that the migration algorithm used for P-S data imaging should respect the asymmetric ray-path and the nature of the elastic wave-fields. Ray-based migration algorithms (e.g., Kirchhoff migration) are simple, fast and can deal with steep dipping structures. However, they are restricted when it comes to deal with asymmetric ray-paths with complex geology and velocity variations. The reason for that is the high frequency asymptotic approximation that Kirchhoff migration uses and the incapacity to handle unlimited number of ray-paths (Gray et al., 2001). Wave equation migration can overcome the ray-based migration drawbacks and generate accurate images as it naturally models the finite-frequency

effects of wave propagation such as multi-pathing that cause problems in structurally complex areas (Rickett and Sava, 2002).

Another point to consider is the high uncertainty in correlating P-P and P-S images in time domain. The main reasons for that are the differences in P-S waves propagation time compared to P-P waves reflected from the same subsurface event, and the different reflectivity of P-S waves compared to P-P waves. In addition to that, applying different static shifts on different receiver components increase the possibility of miscorrelation. Accordingly, using depth migration algorithm will be the optimum solution for this problem. Yan and Sava (2008) provided a thorough review on the preceding development of multi-component imaging techniques and discussed the advantages and challenges of elastic imaging using elastic-reverse time migration. Elastic reverse-time migration is discussed in more details in chapter (3) of this thesis.

2 Fast-track conventional processing of Blackfoot 3C-3D dataset

2.1 Introduction

In this chapter we show a fast-track implementation of conventional multi-component data processing and apply pre-stack Kirchhoff time migration on Blackfoot 3D-3C land dataset. The main objective of this chapter is to get hands-on experience of the challenges and problems following the conventional processing techniques discussed in the introduction chapter, and to have an idea about the expected sub-surface image of Blackfoot dataset. Blackfoot 3D-3C dataset has been a subject of extensive studies dedicated to develop multi-component data acquisition, processing and imaging, conducted by CREWES research group (e.g., Lawton et al., 1995; Simin et al., 1996; Miller, 1996; Lu and Margrave, 1998; Gulati et al., 1998). This available information made Blackfoot dataset suitable for testing new approaches and algorithms.

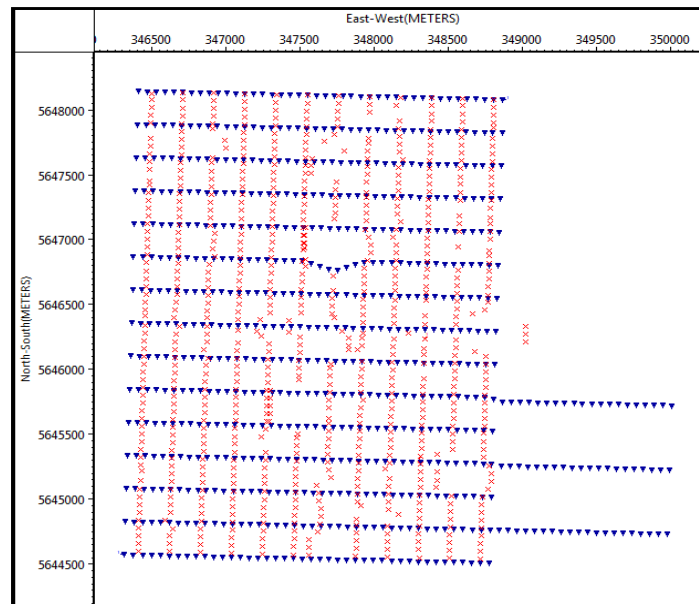


Figure 2.1: Blackfoot 3C-3D acquisition geometry. Red cross represent shot position, blue triangle represent a receiver station.

The data was acquired in 1995 over the Blackfoot field, Alberta, Canada. The survey was designed in 3D in-line array with 60 m source interval and 210 m source-line spacing and 60 m group interval with 255 m receiver-line spacing. The acquisition geometry is shown in Figure 2.1, where receiver lines are oriented in East-West direction and source line is oriented North-South. The data have 708 shots 2070

channels where 690 channels were used per component. The horizontal geophone components are oriented according to in-line direction (East component) and cross-line direction (North component). The source used was 4 *kg* dynamite charges planted down to 18 *m* depth. The data sampling rate is 2 *ms* with recording frequency spectrum of 3-207 *Hz*. The data is available for purchase at the Society of Exploration Geophysicists bookstore. The provided vertical component record length was truncated at 2 *s* while the horizontal components record was truncated at 3 *s*.

2.2 Method

As our main objective is to address the challenging nature of P-S waves, we apply fast-track processing flow that does not address the issues of random noise removal, amplitude attenuation or multiple removal. We are only concerned with the data binning, rotation, static correction, velocity analysis, and migration. The data was processed using VISTA® seismic data processing software. Initial phase of this work was done using ProMAX® software, but for license technical issues we had to shift to VISTA®.

Visual quality control of the recorded shots for the three geophone components showed less quality of the horizontal records compared to the vertical record, with lower signal to noise ratio. In order to increase signal to noise ratio, editing of bad traces and inner mute of ground roll were applied on all the components. Adding to that air blast attenuation process was applied to remove the air blast noise especially from near offset receivers. For residual static calculations we used stack-power maximization algorithm (Ronen and Claerbout, 1985; Eaton et al., 1991). The technique is based on cross-correlation between traces of the same CDP iteratively in order to find the best static model that optimize the stack-power. All the static corrections are calculated based on 1000 *m* constant elevation datum. All the seismic sections presented in this chapter were subjected to time gain (t^3) and frequency bandwidth was limited to 5-50 *Hz* for better data display. Prior to pre-stack Kirchhoff migration, AGC filter with operator length of 300 *ms* was applied on both data of radial and vertical components.

2.2.1 Processing of vertical component

Processing flow for vertical component is displayed in Figure 2.2. Geometry was assigned to the data, with bin size of 30 *m* by 30 *m*. The fold map is displayed by Figure 2.3 with maximum fold of 175. Elevation statics were estimated with P-wave replacement velocity of 3000 *m/s*. After initial velocity analysis and NMO correction, residual statics were calculated. Stack-power optimization resulted in more coherent CDP gathers. Another round of velocity analysis was required to pick more accurate stacking

velocity. By comparing Figure 2.4 to Figure 2.5, we can see how residual statics enhanced the CDP gather coherency. The result of pre-stack Kirchhoff time migration is shown in Figure 2.6.

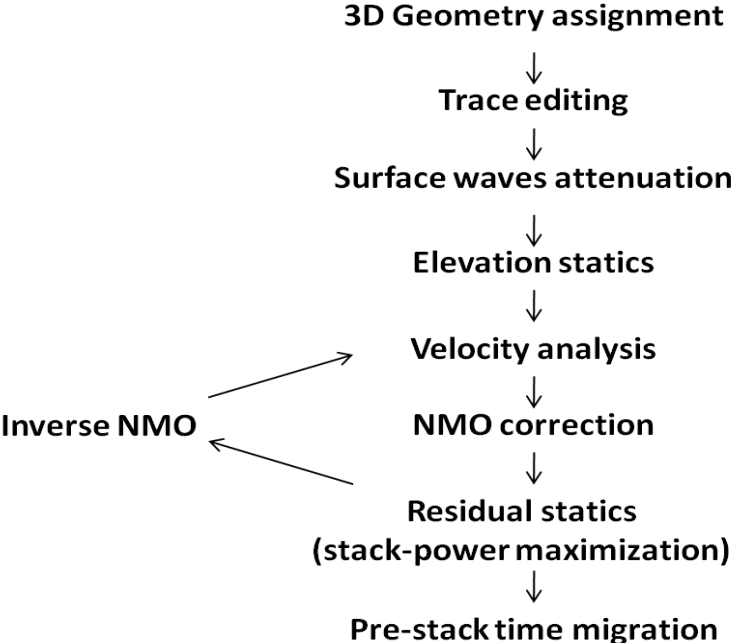


Figure 2.2: Vertical component processing flow.

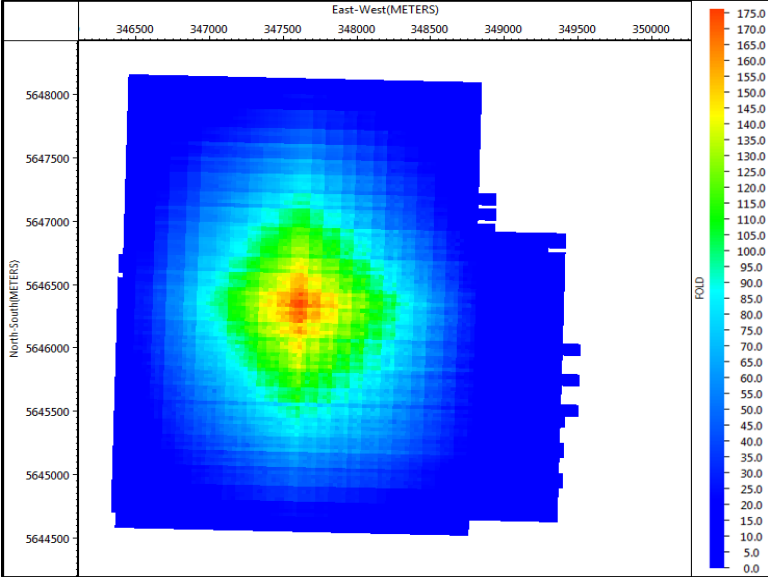


Figure 2.3: Fold map of vertical component with bin size of 30 x 30 m².

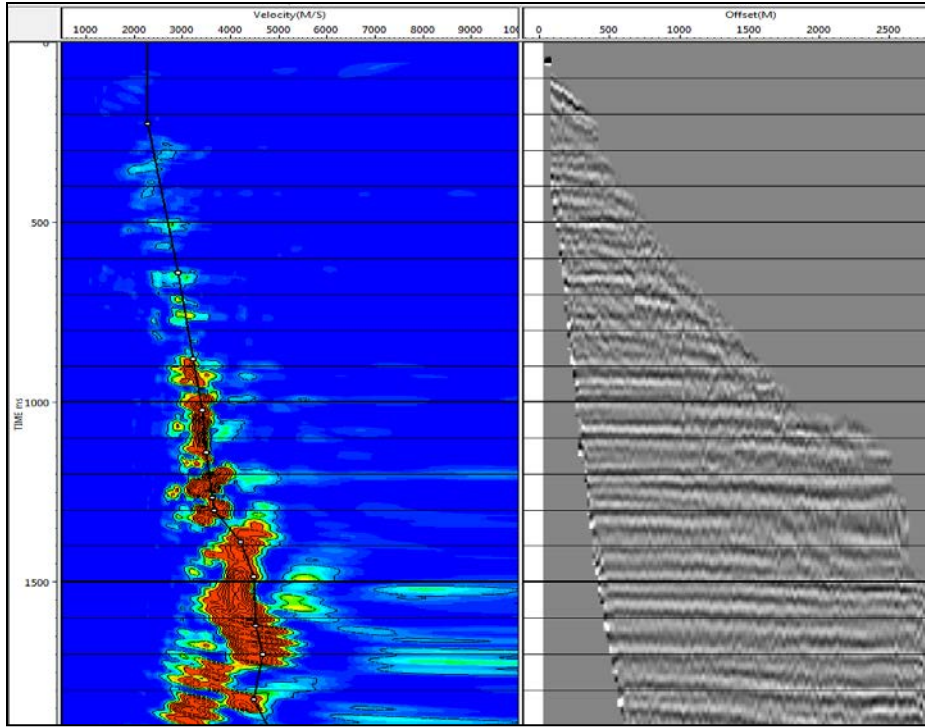


Figure 2.4: The result of initial velocity analysis, prior to residual statics.

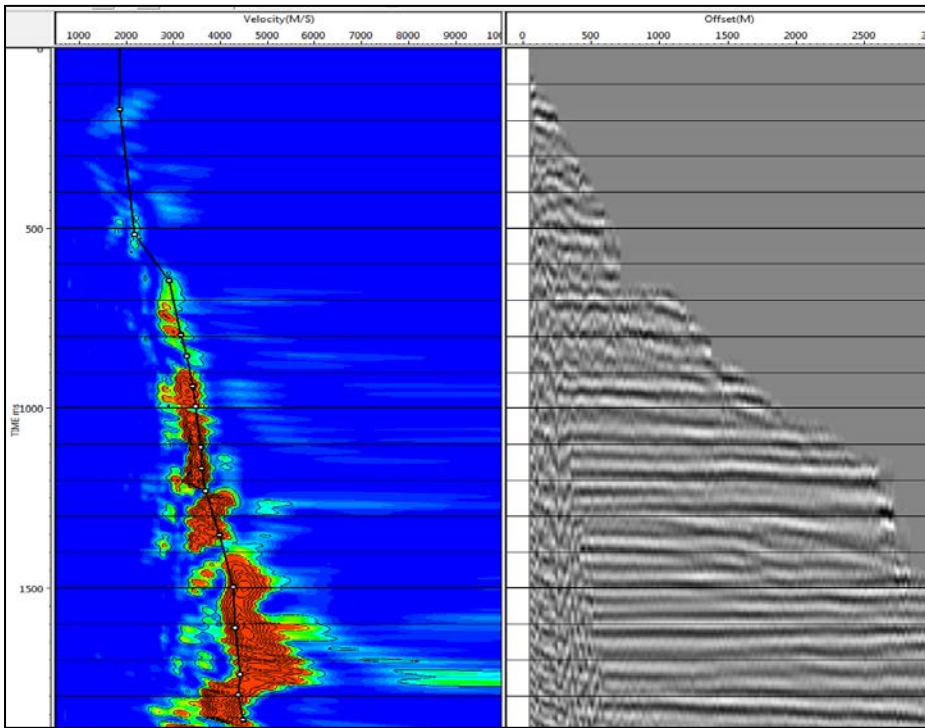


Figure 2.5: Velocity analysis after residual statics application.

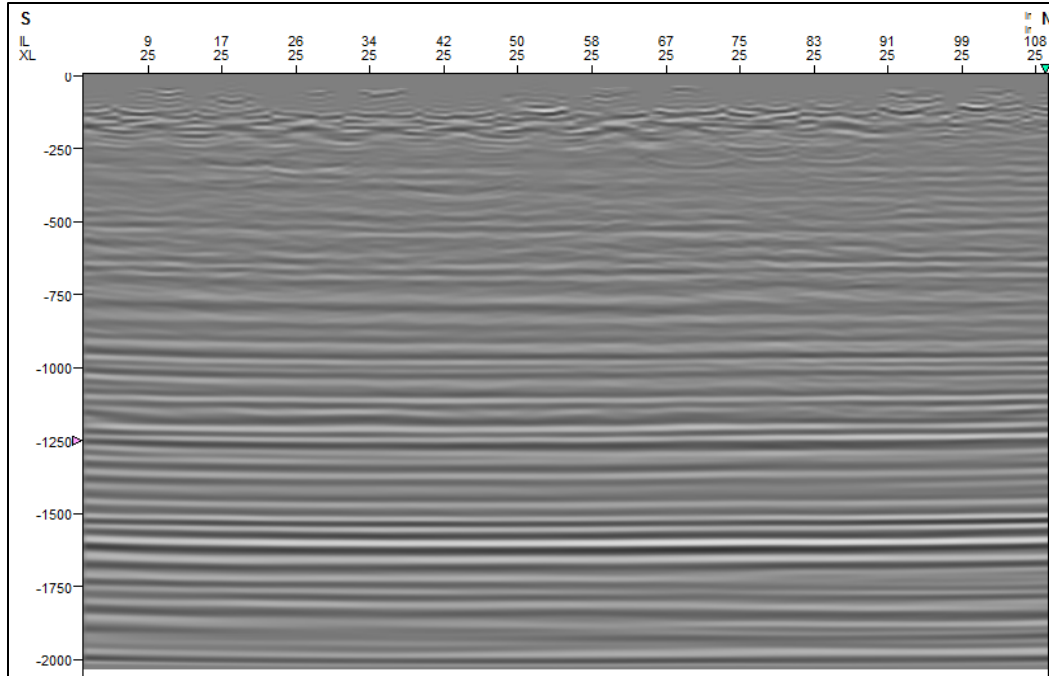


Figure 2.6: Pre-stack migrated section of vertical component data.

2.2.2 Processing of radial component

Radial component processing flow is illustrated in Figure 2.7. Asymptotic binning method was used with velocity ratio ($V_p/V_s = 2$). Figure 2.8 display the resulting fold map of asymptotic binning, with maximum fold of 108. First step is to apply components rotation according to source-receiver azimuth, in order to produce radial and transverse components. The orientation result is presented in Figure 2.9. The receiver gathers of the horizontal components show signal recorded by both components and polarity changes along the traces are observable. After components rotation, the radial component represents the data recorded in source-receiver plane and show consistent polarity. The transverse component does not show a detectable reflection signal, indicating insignificant S-wave splitting. This was also observed by previous processing studies of Blackfoot dataset done by Simin et al. (1996) and Lu and Margrave (1998). Accordingly no S-wave splitting analysis was conducted.

Source elevation statics were taken from vertical component statics. Receiver elevation statics were calculated based on shear wave velocity of 1500 m/s . Initial converted wave velocity analysis and non-hyperbolic moveout correction according to Slotboom (1990) approach is displayed in Figure 2.10. Based on initial velocity, stack-power optimization was applied. After applying residual statics, velocity spectrum was tremendously improved and ACP gathers became more coherent as noticed by comparing

Figure 2.10 with Figure 2.11. In Figure 2.12 we compare between the produced stacked images of the data before and after residual statics, and the migrated images using Kirchhoff pre-stack time migration and post-stack Stolt migration, exhibiting the advantage of pre-stack migration.

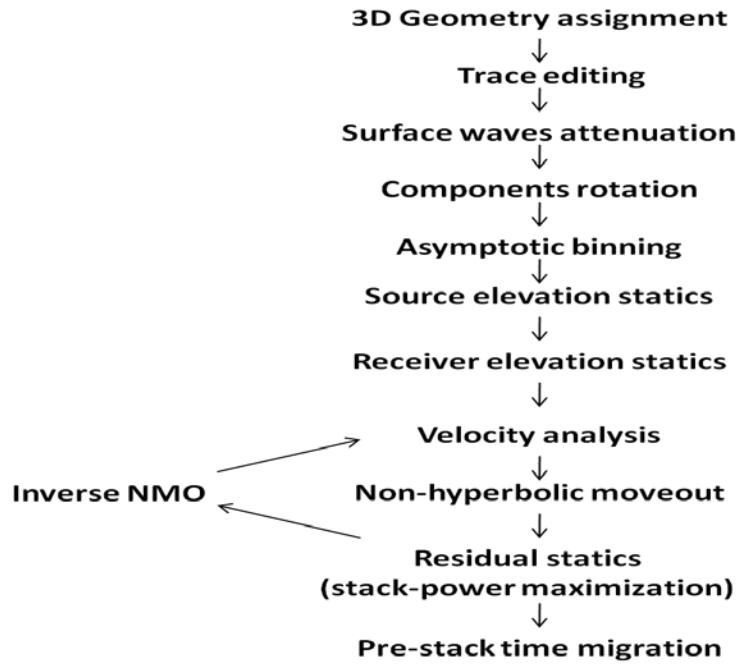


Figure 2.7: Radial component processing flow.

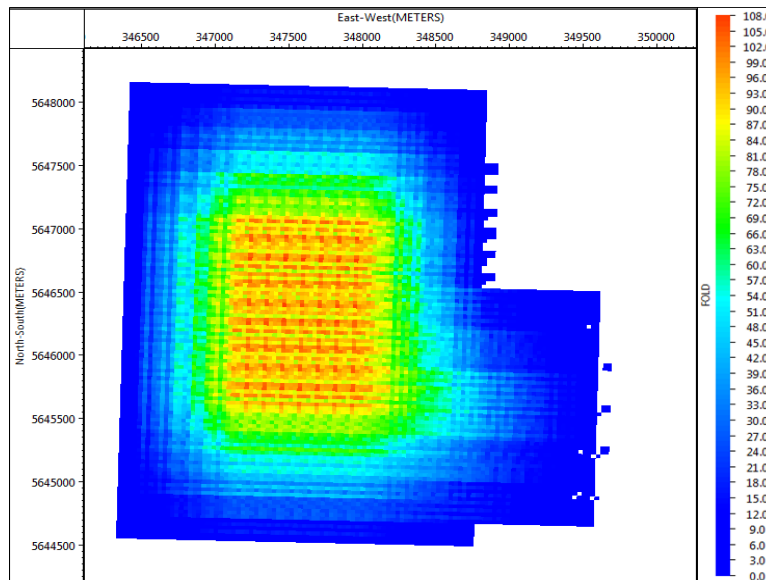


Figure 2.8: Fold map of radial component with bin size of $30 \times 30 \text{ m}^2$.

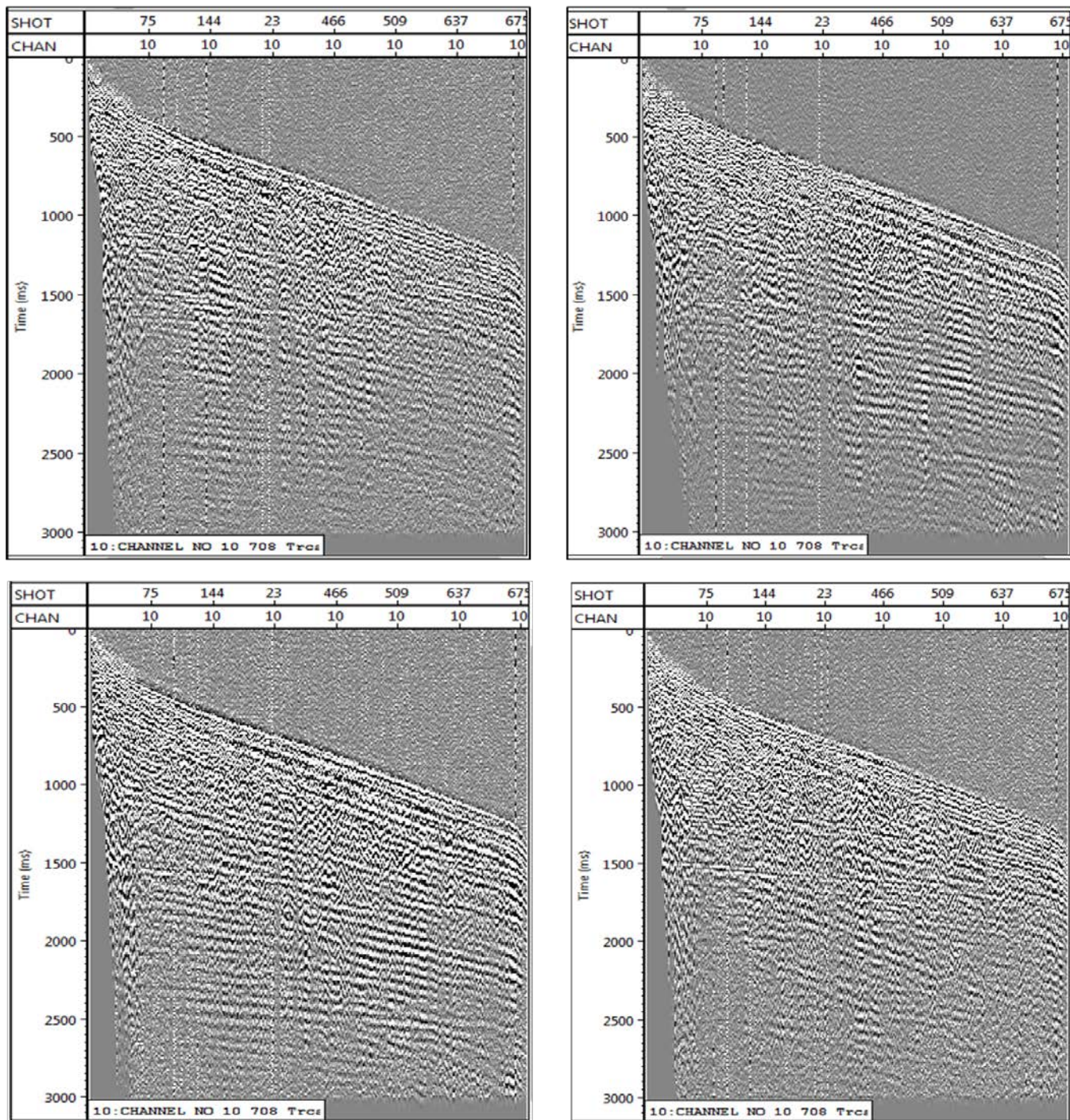


Figure 2.9: Receiver gathers of channel number 10.

Top left: H1 (East component).

Top right:H2 (North component)

Bottom left: Radial component.

Bottom right: Transverse component.

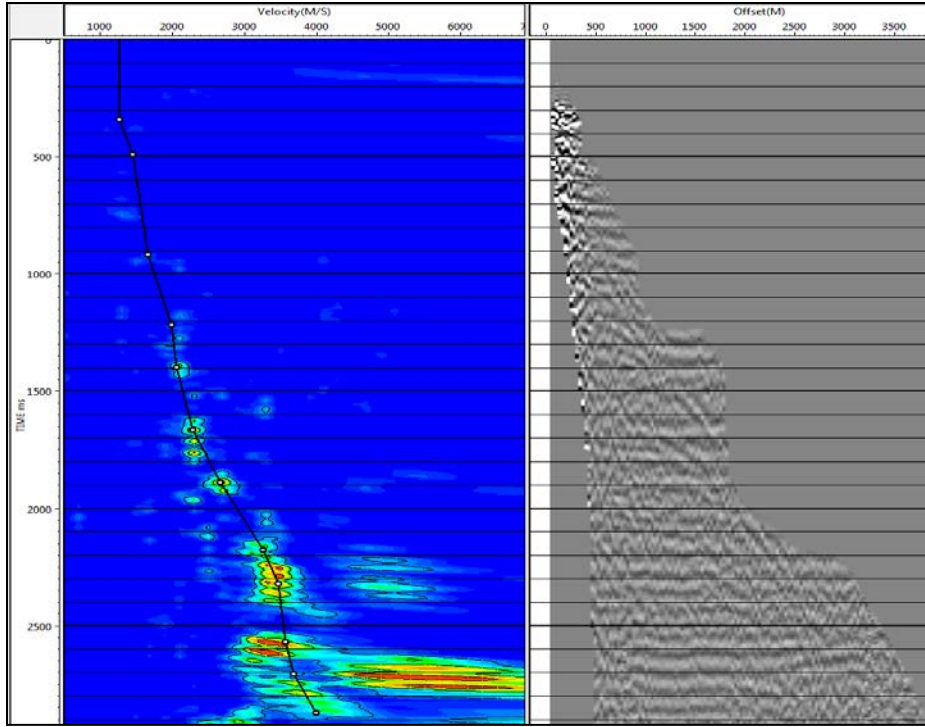


Figure 2.10: Initial velocity analysis for radial component, prior to residual statics.

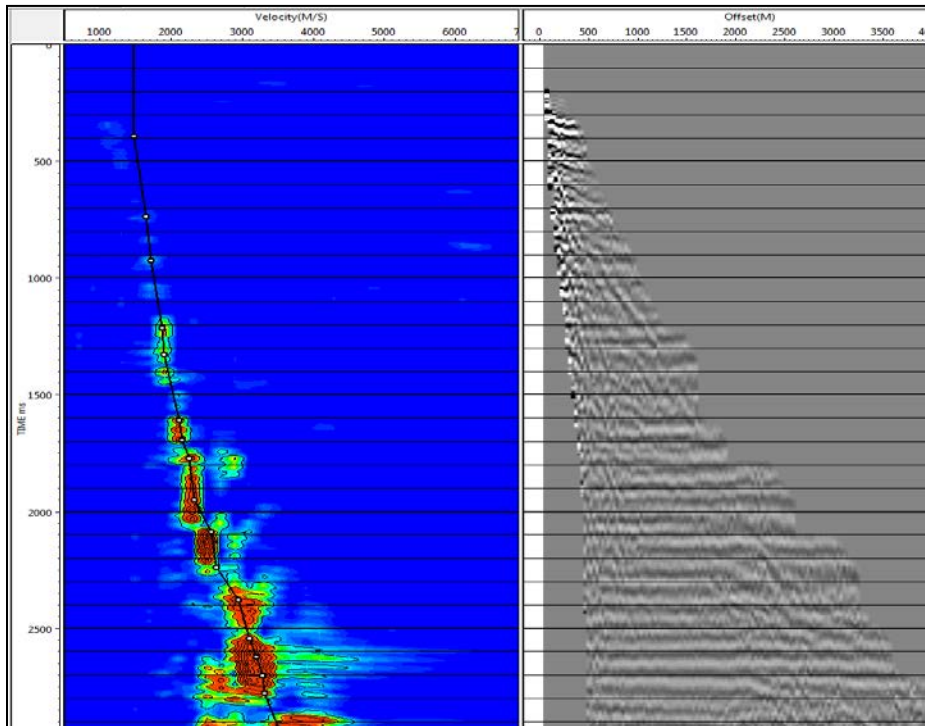


Figure 2.11: Velocity analysis after residual statics.

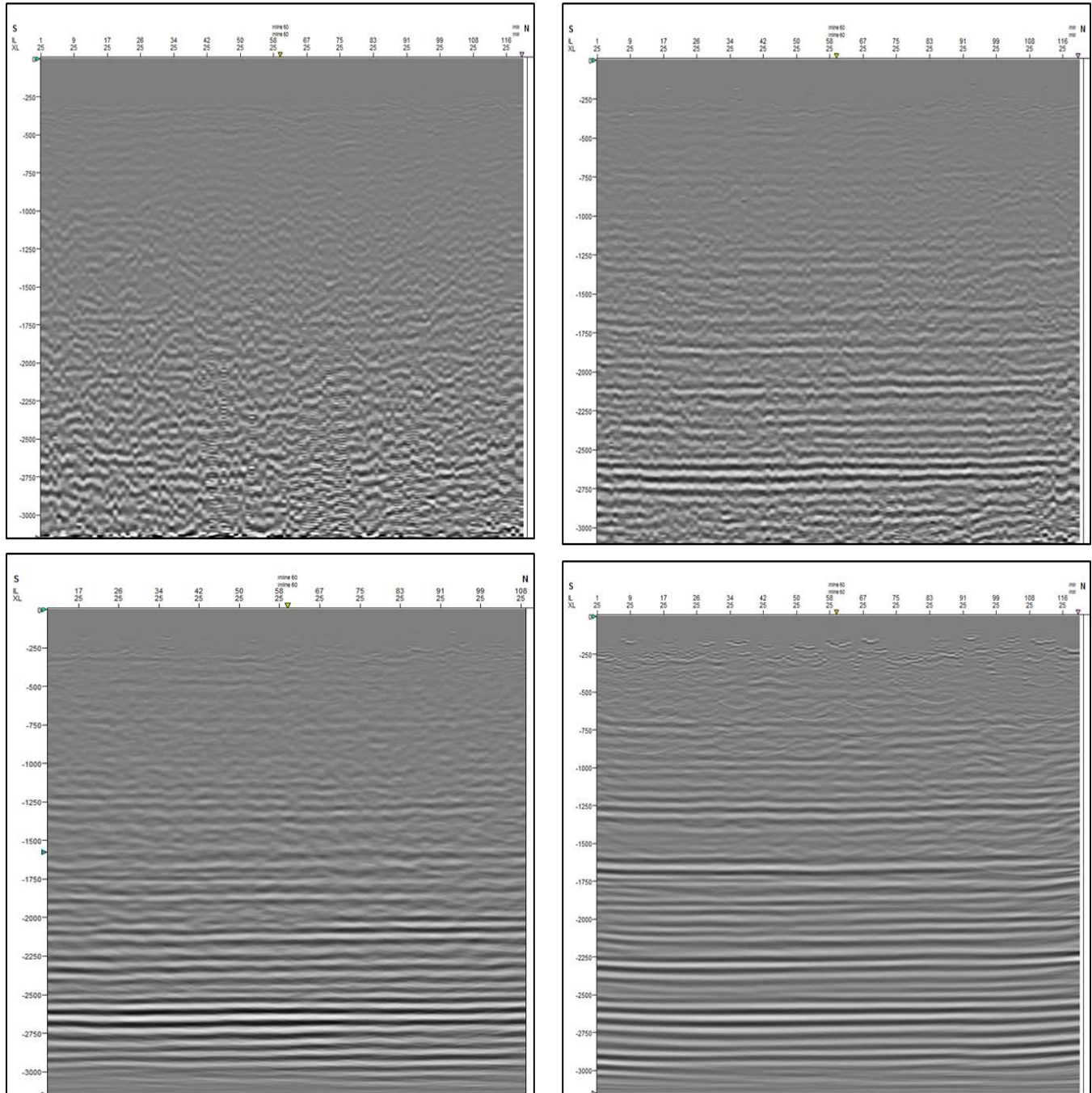


Figure 2.12: Images of cross-line section of radial component.

Top left: Brute stack based on initial velocity analysis.

Top right: Stack after applying residual statics and enhanced velocity analysis.

Bottom left: Post-stack FK-Stolt migrated section.

Bottom right: Pre-stack time migration (Kirchhoff migration).

2.3 Discussion

In this chapter we practically investigated the main challenges of conventional multi-component data processing, which mainly are tackled by horizontal component rotation, repeated velocity analysis and refining static corrections. Velocity analysis of radial component result in reasonable converted wave stacking velocity, but still this velocity is not physically correct to represent the subsurface and require further approximation to obtain shear wave velocity information.

With Blackfoot data, the migrated vertical and radial images show nearly flat reflectors. Comparing the two migrated images shows how difficult it is to correlate the images in time domain. In Figure 2.13 we display a correlation between both images, where the red arrows indicate the key reflectors on both images. We observe here what can be a leakage of P-P signal into the radial component image at 1250 *ms*. That reflector indicated by the yellow arrow shows more coherent reflectivity on radial image, while on vertical component image the reflector that should be correlated to it does not show similar coherency. Certainly that can arise from many other different reasons, which leave the door open for more uncertainty.

Conventional imaging of converted waves is restricted to capabilities of the assumptions used in estimating the subsurface parameters. The uncertainties resulting from V_p/V_s ratio, binning method and static corrections will affect the quality of P-S image. Even with support of hard information such as well data, the issues of wave-mode separation and vector fidelity of the recorded data in addition to the uncertain velocity estimation will degrade the reliability of P-S image whatever advanced the migration algorithm is.

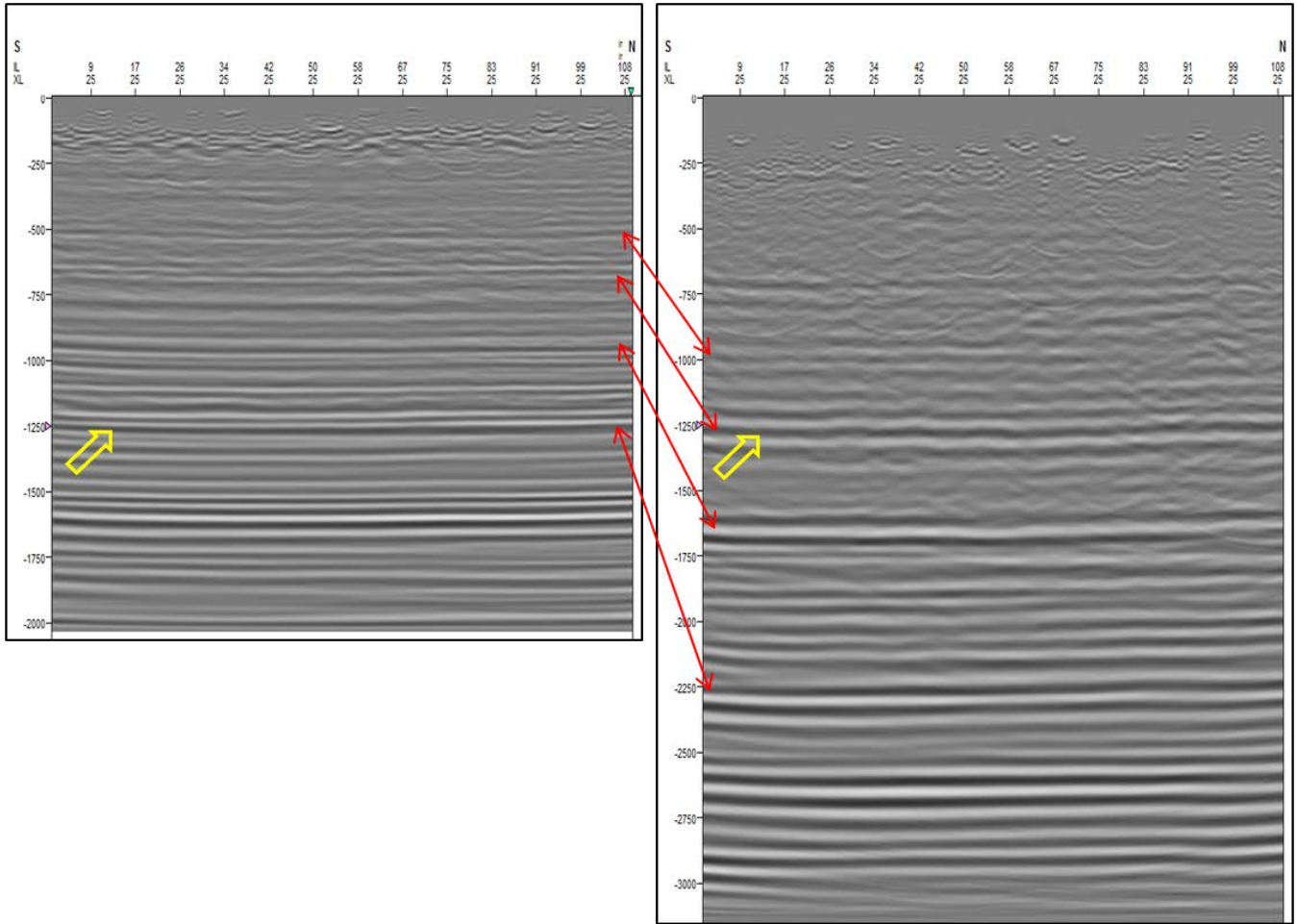


Figure 2.13: Correlation between vertical component migrated image (left) to the radial component migrated image.

3 Multi-component elastic reverse-time migration in isotropic media

3.1 Introduction

Seismic data migration objective is to reconstruct recorded reflection energy to its true subsurface position. Migration algorithms are classified according to the approximate wave equation and the numerical solutions the algorithms are based on. The first main assumption that all the current practical imaging methods share is the single scattering approximation, which is also known as Born approximation. Sava and Hill (2009) and Jones (2015) provided in-depth reviews on migration algorithms and classifications. Imaging procedure efficiency is limited by the capabilities and physical accuracy of the algorithm used. Adding to that, the imaging efficiency will be influenced by the data quality and the subsurface parameters including seismic wave velocity, anisotropy parameters and attenuation (Q).

Reverse-time migration (Baysal et al., 1983) is an advanced migration algorithm for seismic depth imaging based on solving the two-way wave equation, where the down-going source wave-field is forward extrapolated and the up-going wave-field (recorded wave-field) is backward extrapolated in time through the earth model. This forward modeling exercise is a fundamental element of Reverse-time migration. The reflectivity in the subsurface is mapped by applying imaging conditions that evaluate the match between reconstructed wave-fields at each time step of the reconstruction by the cross-correlation of an up-going and a down-going wave-field (Claerbout, 1971; Rickett and Sava, 2002). Reverse-time migration provides improved images in areas where complex geology violates the assumptions made in ray-based (e.g., Kirchhoff) or one-way wave equation migration, where it combines the strengths of Kirchhoff migration for steep-dip resolving as it has no dip limitation, and the advantages of one-way wave equation migration for multi-pathing and handling complex velocity variations.

As discussed before in introduction chapter, the vector nature of P-S wave-field and related challenges of multi-component data urge the need for a robust migration algorithm that can handle these challenges and produce less uncertain images. Application of elastic reverse-time migration (ERTM) (Sun and McMECHAN, 1986; Chang and McMechan, 1987) for elastic wave imaging of multi-component data has been the main interest of many researchers. Yan and Sava (2008) provided a thorough review on the preceding development of multi-component imaging techniques and discussed the challenges of elastic wave-mode separation and elastic wave-field imaging using elastic reverse-time migration. The main focus of many publications was directed on wave-mode separation techniques. The separation of wave

modes from isotropic elastic wave-field is usually done using Helmholtz potentials decomposition in order to separate the wave-modes prior to applying imaging conditions (Dellinger and Etgen, 1990; Yan and Sava, 2007; Zhu, 2017) or using elastic displacement imaging conditions (Etgen, 1988; Zhe and Greenhalgh, 1997; Yan and Sava, 2007; Denli and Huang, 2008; Artman et al., 2009). These techniques can suffer from polarity reversal problem due to changes in the elastic wave-field polarization along incidence direction, which require polarity correction. Besides that, the produced images can suffer from inter-mode cross-talking artifacts. Accordingly, the research efforts are directed to find imaging conditions that can overcome the polarity reversal problem and reduce the related cross-talking artifacts between the two wave modes (Yan and Sava, 2008; Yan and Xie, 2009; Du et al., 2012; Duan and Sava, 2014; Duan and Sava, 2015; Rocha et al., 2017).

In this chapter we introduce imaging conditions for elastic reverse-time migration in isotropic media, where the main objective is to image P-P and P-S scattering events using all receiver components with no need for polarity reversal correction. We tested the proposed ERTM scheme on synthetic and field data. The influence of data quality and attenuation (Q) on the proposed ERTM scheme is investigated.

3.2 Theory

The main purpose of using elastic reverse-time migration is to create subsurface images of single-scattering reflections of (P-P, P-S, S-S, S-P). This requires an imaging condition able to distinguish apart the different scattering events.

To make distinct images of these reflection events, we propose imaging conditions based on the gradients of elastic full-wave form inversion (EFWI) with respect to P- and S-wave impedances, where the gradients of the least squares misfit between the observed multi-component seismic data and the single-scattered (Born modeled) reflection data are calculated in isotropic elastic media with smooth velocities V_p and V_s (Mora, 1987). The velocities should consist of the smooth component of the velocity field in order to produce only negligible scattering, a condition that is often violated in practice.

These imaging conditions have been explored by Hokstad et al., (1998) to produce elastic reverse-time migrated images of P-P and P-S reflections from multi-component vertical seismic profiling (VSP) data, and more recently by Alves and Biondi (2016) to create images using 2D synthetic multi-component data.

If we consider that the seismic source is in acoustic medium, or that the source is a pure pressure source, then the only possible single scattering reflection modes are the P-P and the P-S modes and imaging conditions for P-P image and P-S image can be formulated as described in equations 3.1 and 3.2, respectively.

Proposed imaging conditions:

$$I_P(\mathbf{x}) = \sum_s \int dt C_p(\mathbf{x}) \varepsilon_{ii}^s(\mathbf{x}, t; s) \varepsilon_{jj}^r(\mathbf{x}, T - t; s) \quad 3.1$$

$$I_S(\mathbf{x}) = \sum_s \int dt C_s(\mathbf{x}) [\varepsilon_{ij}^s(\mathbf{x}, t; s) \varepsilon_{ij}^r(\mathbf{x}, T - t; s) - \varepsilon_{ii}^s(\mathbf{x}, t; s) \varepsilon_{jj}^r(\mathbf{x}, T - t; s)] \quad 3.2$$

where I_P is the P-P image, I_S is the P-S image, $C_p(\mathbf{x}) = v_p^4(\mathbf{x})$, and $C_s(\mathbf{x}) = v_s^4(\mathbf{x})$ are scaling factors, $\mathbf{x} = (x, y, z)$ is the Cartesian position vector, $\varepsilon_{ij} = \frac{1}{2} \left(\frac{\partial u_i}{\partial x_j} + \frac{\partial u_j}{\partial x_i} \right)$ are the components of the infinitesimal strain tensor, t is the time, and s is the source index. The s and r superscripts refer to the reconstructed source and receiver wave-fields, respectively. The equations are written with an implicit summation over repeated indexes.

The displacements u_i^s and u_i^r are computed through a solution to the density normalized elastic wave equation, using respectively an explosive point source (S), and the time reversed 3C single scattering reflection data (u_i^{obs}) as right hand sides on the equations, as shown below:

$$\frac{\partial^2 u_i^s}{\partial t^2}(\mathbf{x}, t; s) - \frac{\partial}{\partial x_j} \left[a_{ijkl}(\mathbf{x}) \frac{\partial u_l^s}{\partial x_k}(\mathbf{x}, t; s) \right] = \frac{\partial S}{\partial x_i}(\mathbf{x}_s, t; s) \quad 3.3$$

$$\frac{\partial^2 u_i^r}{\partial t^2}(\mathbf{x}, T - t; s) - \frac{\partial}{\partial x_j} \left[a_{ijkl}(\mathbf{x}) \frac{\partial u_l^r}{\partial x_k}(\mathbf{x}, t; s) \right] = \frac{\partial^2 u_i^{obs}}{\partial t^2}(\mathbf{x}_r, T - t; s) \quad 3.4$$

The main advantage of these imaging conditions is that it does not require polarity reversal correction or expensive wave mode separation, besides that they are independent of the complexity of the model. One possible disadvantage is the cross-talking between wave-modes in the cross-correlation process. However, we will show that given proper velocity models and adequate subsurface parameters, the artifacts tend to be stacked away. In this chapter we will focus on the impacts of data quality and vector fidelity of multi-component data. We will also examine ERTM under the influence of attenuation (Q) based on synthetic visco-elastic models. The effect of velocity field accuracy will be discussed in details in chapter 3

3.3 Synthetic example

We show an example of applying the proposed ERTM scheme on synthetic dataset based on a 2D section across the Gullfaks field offshore Norway. The seismic data is simulated using finite difference modeling of the elastic wave equation (Virieux, 1986). Free surface multiples are not modeled. The survey geometry consists of an ocean bottom cable, with a maximum offset up to 4 km. Data recorded consists of both the vertical and radial components of the displacement field. The source is a Ricker wavelet with a center frequency of 10 Hz. The source depths are 10 meters and the receiver depths are 200 m. The Gullfaks synthetic model elastic parameters used for generating the data is shown in Figure 3.1, notice the velocity anomaly on V_p model related to the reservoir at depth near to 2000 m. The S-wave velocity model used had near-surface velocity perturbations, which had its effect on the P-S signal recorded by both vertical and radial component as displayed in Figure 3.2.

Applying ERTM based on the proposed imaging condition using true velocity models successfully produced P-P and P-S images shown in Figure 3.3. The produced images show the special characteristics of P-P and P-S images accurately represented with no wave-modes leakage, where on P-P image we can see the amplitude anomaly related to the reservoir base with no effect on P-S image. Moreover, P-S image has higher resolution when compared to the P-P image, due to the shorter wavelengths of S-wave compared to P-wave.

This example represents a successful application of the proposed workflow. However, in this example we have the correct subsurface parameters with no effects of low signal to noise ratio, poor vector fidelity or wave attenuation.

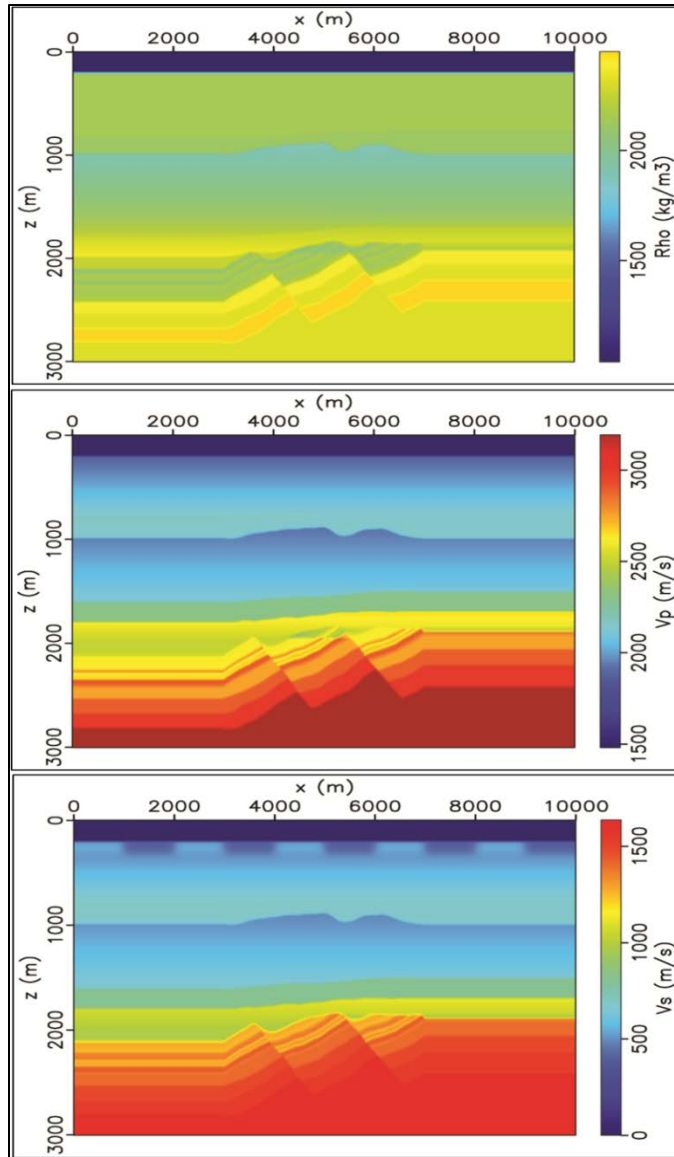


Figure 3.1: Model parameters.

Top: density model.

Middle: P-wave velocity model.

Bottom: S-wave velocity model.

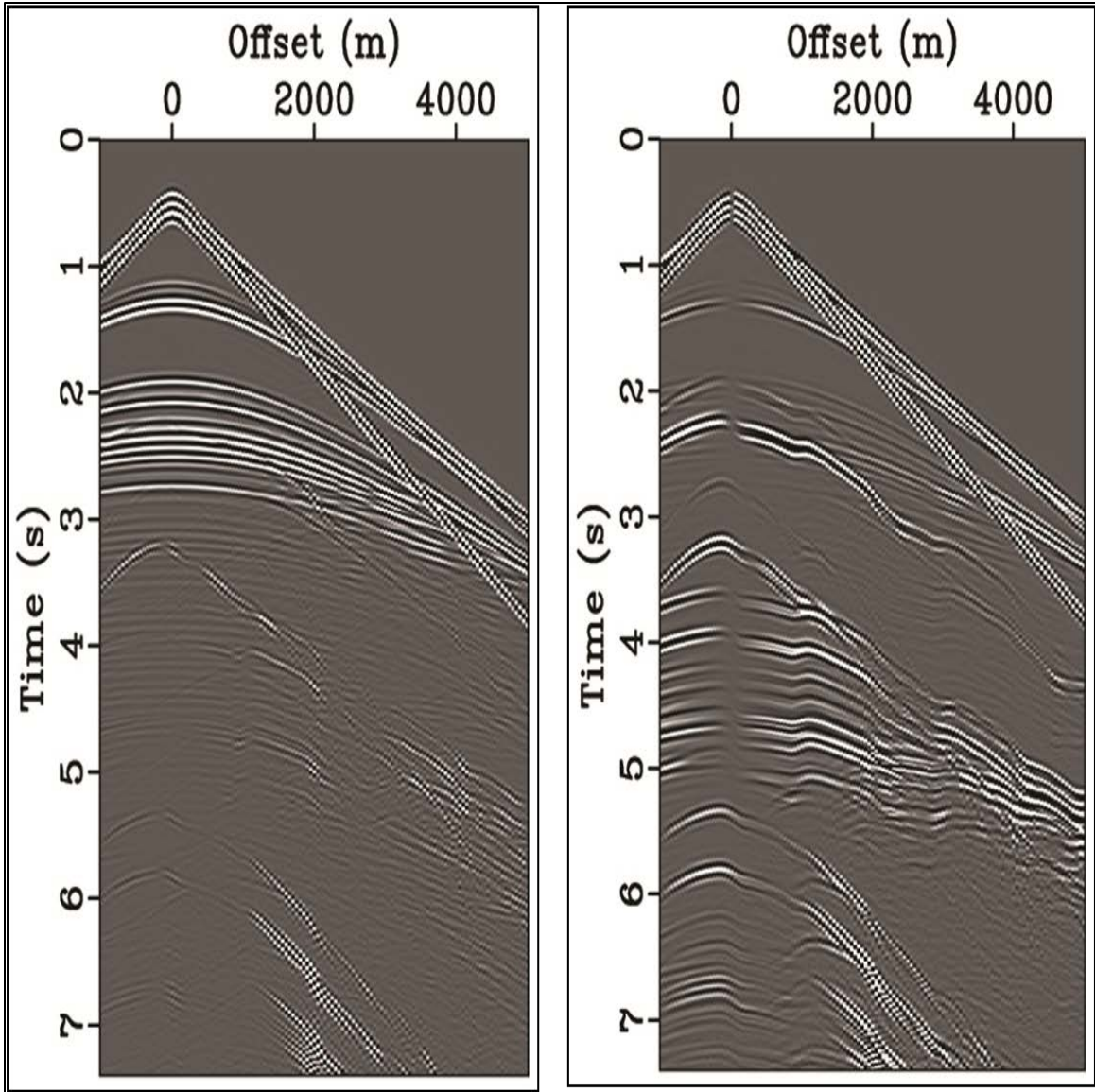


Figure 3.2: Shot gathers of vertical component (right) and radial component (left).

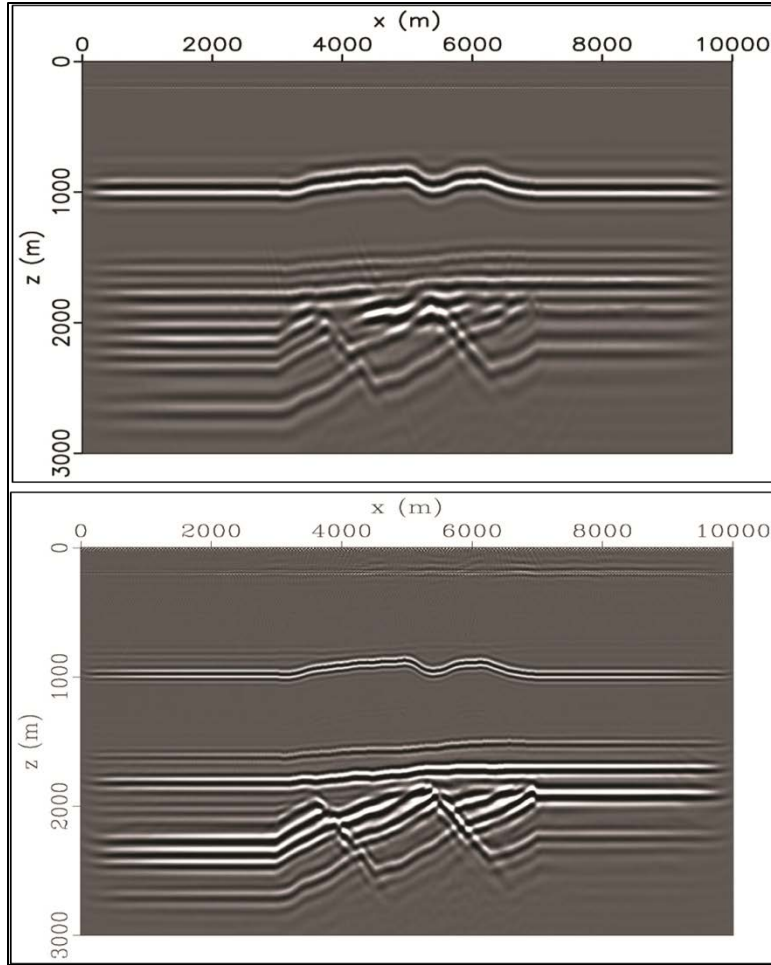


Figure 3.3: Results of ERTM using proposed imaging conditions.

Top: P-P image.

Bottom: P-S image.

3.4 Field data example

In order to have a more realistic assessment of the proposed ERTM scheme robustness, we tested the algorithm on Blackfoot 3D-3C dataset. The dataset specifications were discussed in chapter 2. The main advantage of using Blackfoot is the availability of subsurface information presented in many published studies, which makes it a suitable example in testing new algorithm. However, the different time record truncation of the vertical and horizontal components, at 2 s and 3 s respectively, has its disadvantage of reducing the data consistency, as no P-S signal is recorded on vertical component after 2 s.

ERTM is computationally intensive, for that reason, optimizing the algorithm performance on 2D dataset prior to 3D implementation is required, and it is still sufficient to examine the algorithm robustness. Accordingly, we extracted 2D lines out of the 3D dataset and tested the algorithm on them. The extracted 2D data has very low fold due to the 3D survey nature of the original dataset. In this section we will show the migration results of two orthogonal (N-S and E-W) 2D sections of Blackfoot data. Figure 3.4 display the geometry of the extracted lines. The N-S line has 72 shots with shot interval of 50 *m* and 15 receiver-stations with receiver interval of 255 *m*. As discussed in chapter 2, the data display poor S-wave splitting, so in 2D lines the in-line horizontal geophone (radial) will represent the signal recorded by horizontal components. The E-W line has 23 shots with shot interval of 210 *m* and 52 receiver-stations with receiver interval of 50 *m*.

We applied an inner mute to remove the ground roll and an outer mute to remove refraction and other post-critical events to increase the signal to noise ratio of the data. The data extracted was subjected to a low-pass filter with a high cut at 50 *Hz*. No amplitude correction of any kind was applied prior to migration in order not to affect the original fidelity of the elastic wave-field. No static corrections were applied on the data as the assumptions of vertical propagation and constant replacement velocity violate the wave-extrapolation in ERTM, and the migrated images are leveled on fixed elevation datum of 1000 *m* as zero depth level. The source and receiver true elevations are maintained. For the area of elevation datum we used 3000 *m/s* and 1500 *m/s* as V_p and V_s respectively. For better display, a depth gain (z^3) was applied to the migrated images. In order to recover the low frequencies of the data with correct phase, we applied a deconvolution of the records with the impulse response of a 10 *Hz* geophone (Bertram and Margrave, 2010). The source wavelet has dominant frequency of 30 *Hz* and maximum frequency of 50*Hz* with a time delay of 0.3 *s*, as displayed in Figure 3.5. The velocity models used in migration are initial velocity models based on manual travel-time fitting using VSP data and ray-tracing, adopted from work done by Gulati et al., (1998).

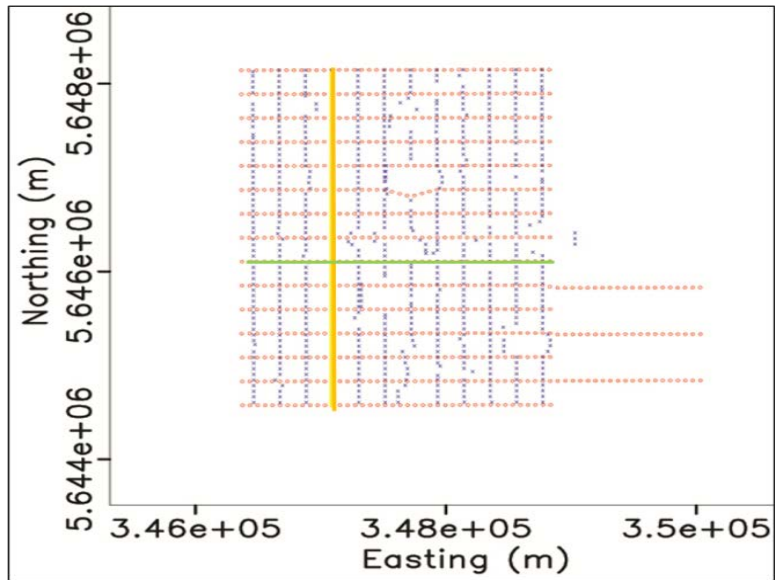


Figure 3.4: Survey geometry with positions of extracted 2D lines. N-S section highlighted in yellow, E-W section highlighted in green.

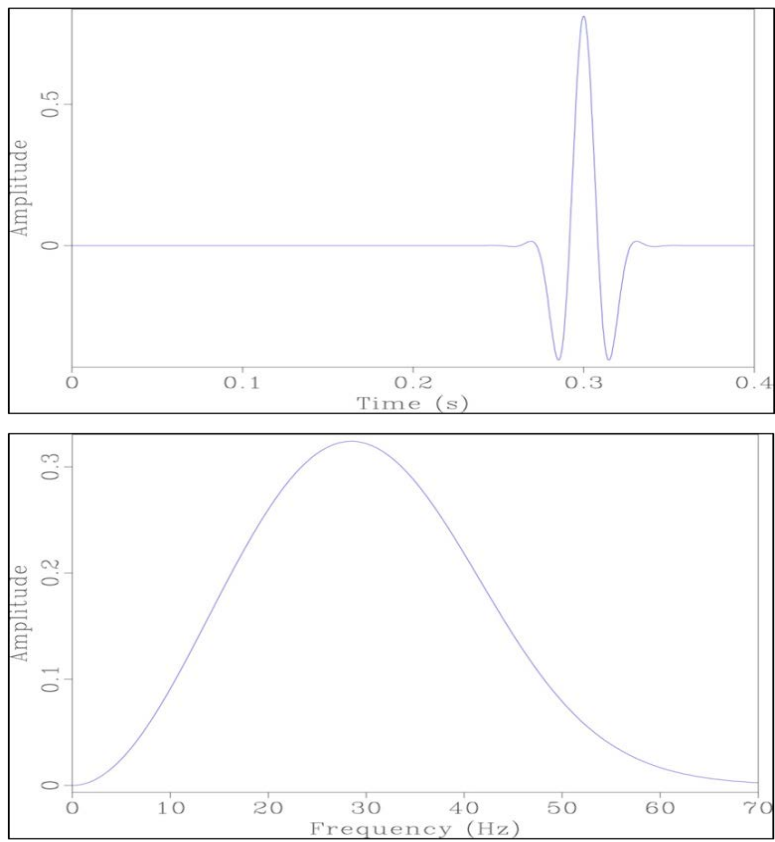


Figure 3.5: Source wavelet used in migration and its amplitude spectrum (Ricker wavelet).

Figure 3.6 shows the receiver gathers of vertical and radial components for N-S section as input data for migration. Using both vertical and radial geophone components for N-S section we obtained P-P and P-S images shown in Figure 3.7. First impression from both migrated images shown in Figure 3.7 is that they nearly look identical. This high similarity raised doubts over the presence of wave-modes cross-talking. In order to check if there is cross-talking between both images, we migrated each component separately from the other, which enabled us to check how much of signal each component will contribute to each image. By using only vertical component, we should expect degraded quality of P-S image in case that most of the P-S signal is coming from the radial component. Instead of that, migration of only the vertical component data produced identical P-S and P-P images (Figure 3.8), nearly the same as in case of using both components. On the other hand, migration of only radial component data produced a reasonable P-S image, while produced P-P image with no significant signal (Figure 3.9).

To check the reproducibility of these observations, we applied migration on E-W section. The data extracted is shown in Figure 3.10, displaying very noisy signal of the radial component, which will have its effect on the migrated image in addition to the very low fold at the section edges. However the main aim was to check if we will get similar response to N-S line case. The produced images shown in Figure 3.11 and Figure 3.12 confirm the results obtained with N-S 2D line.

These observations made us to question the geophone coupling of the horizontal components, an issue that was noticed while conventionally processing the dataset in chapter 32, as we have seen different responses of different components records at the same receiver-station. The poor coupling of horizontal components can severely affect the vector fidelity of the elastic wav-fields recorded. This argument can explain the low P-P signal recorded by radial component, but cannot justify the leakage of P-P wave-mode into P-S image.

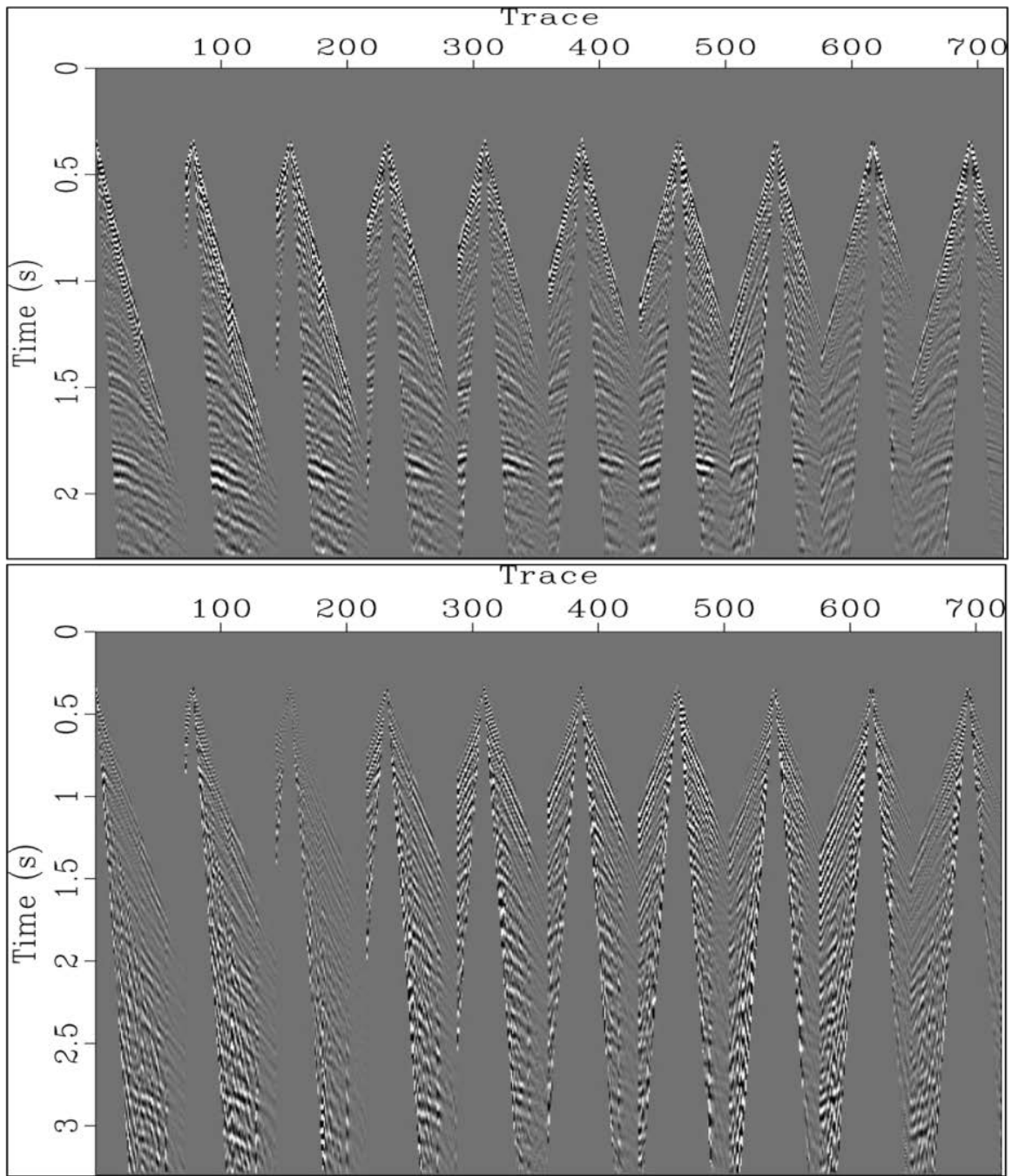


Figure 3.6: Ten receiver-gather records of vertical component (top) and horizontal component (bottom) for N-S 2D line.

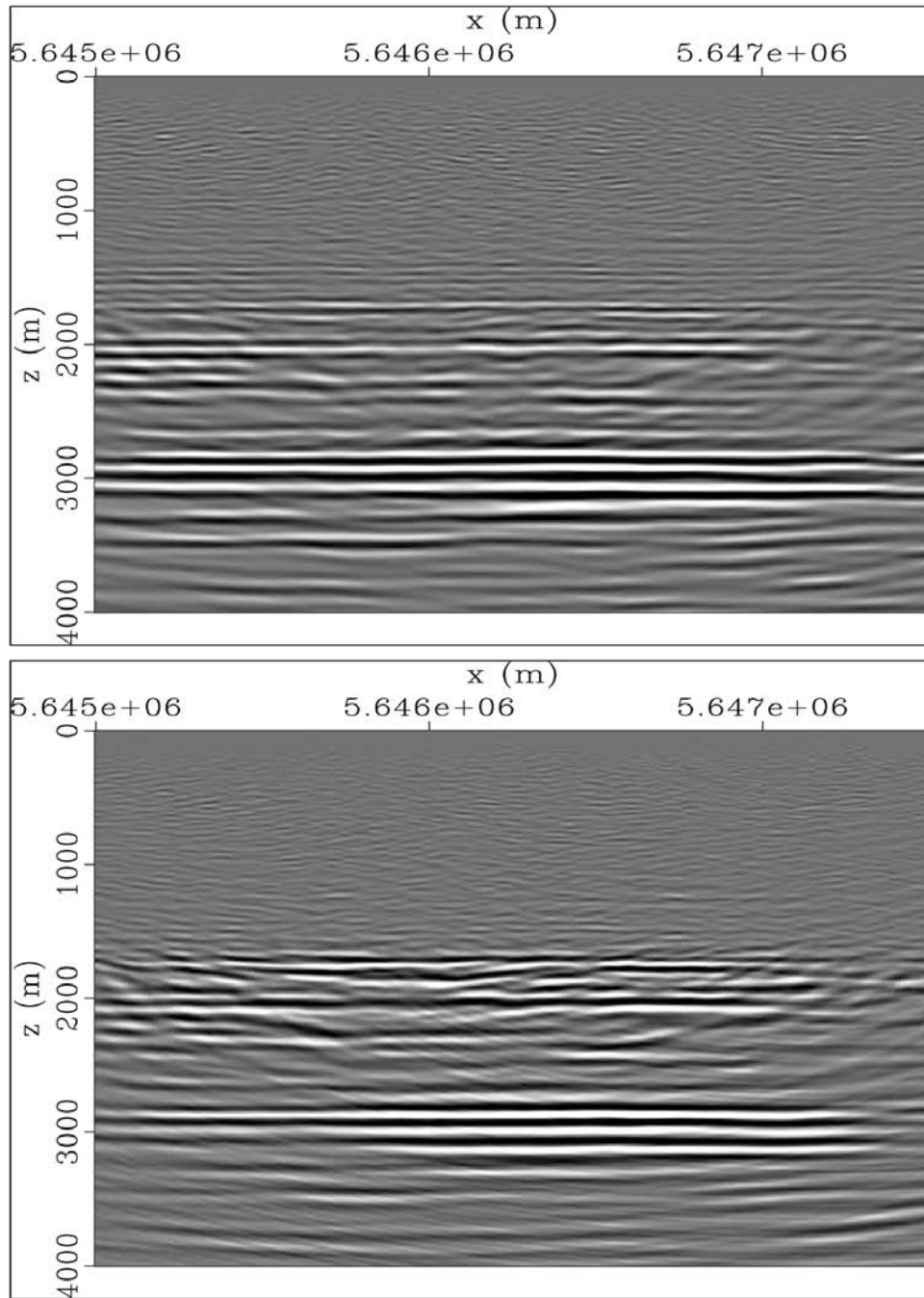


Figure 3.7: Result of ERTM using both vertical and horizontal components for N-S 2D line.

Top: P-P image.

Bottom: P-S image.

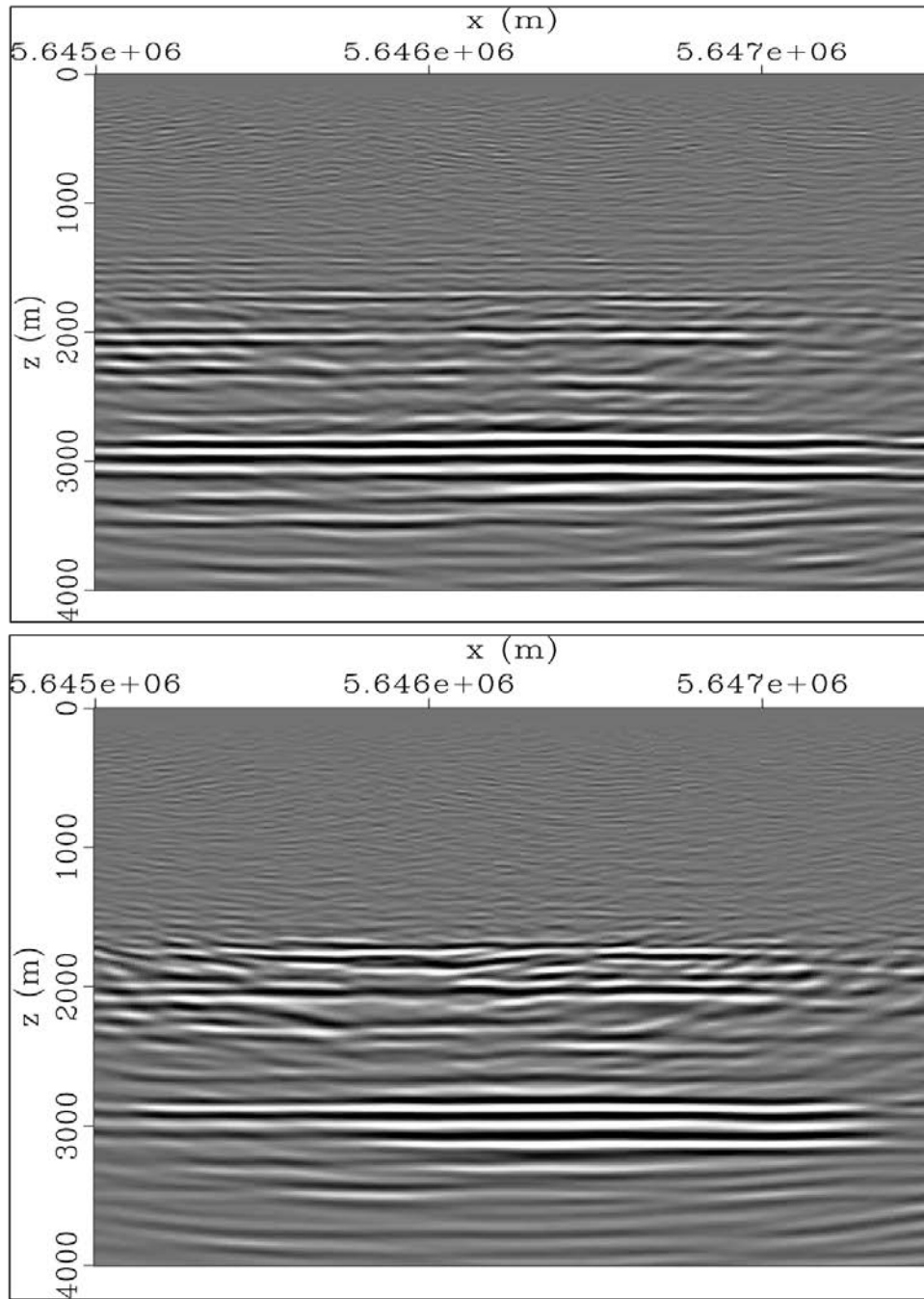


Figure 3.8: Result of ERTM using only the vertical component for N-S 2D line.

Top: P-P image

Bottom: P-S image

Note the high amplitudes in P-S image compared to P-P image.

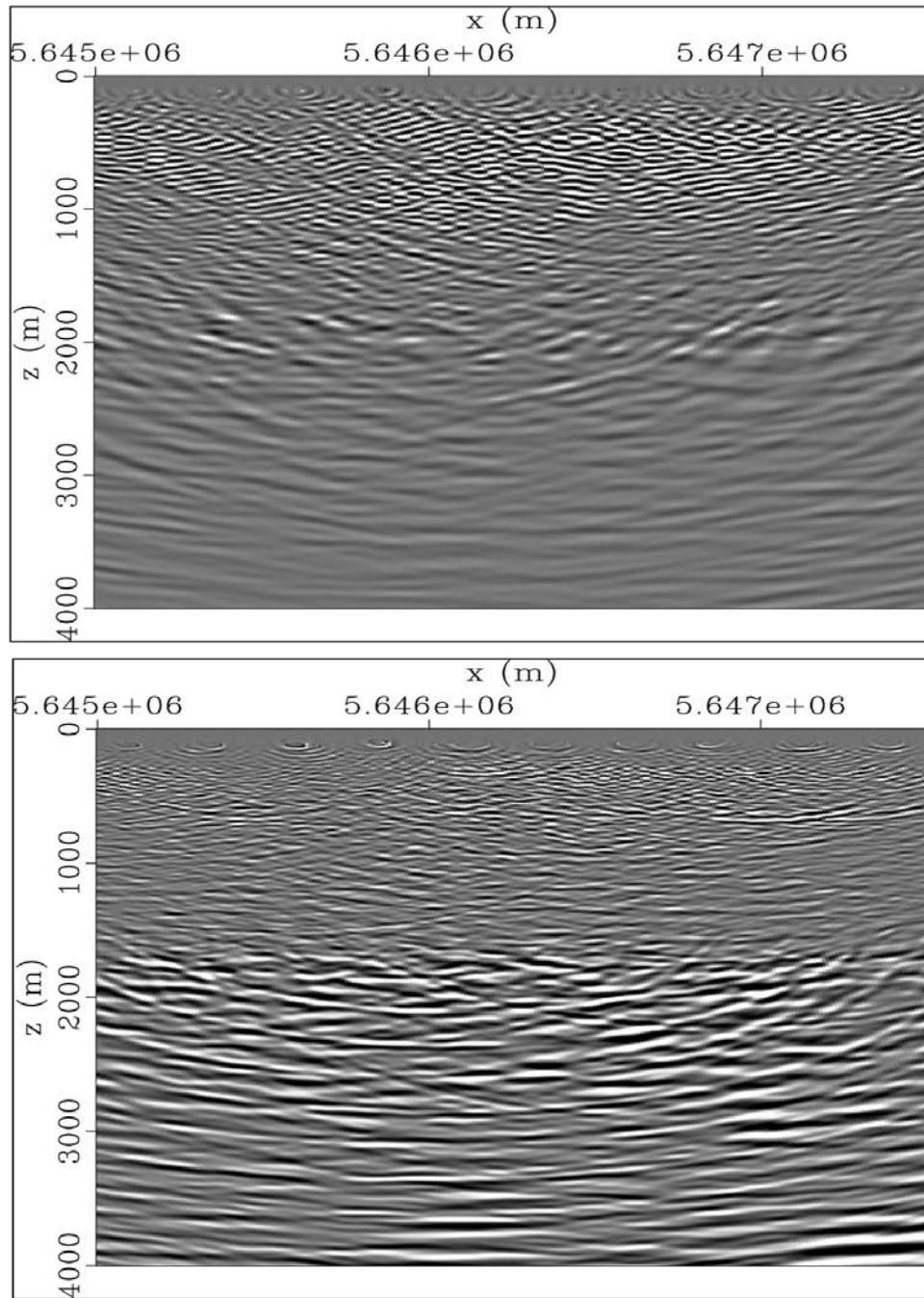


Figure 3.9: Result of ERTM the horizontal component data only for N-S 2D line.

Top: P-P image.

Bottom: P-S image.

Note the low signal in P-P image resulting from horizontal component data.

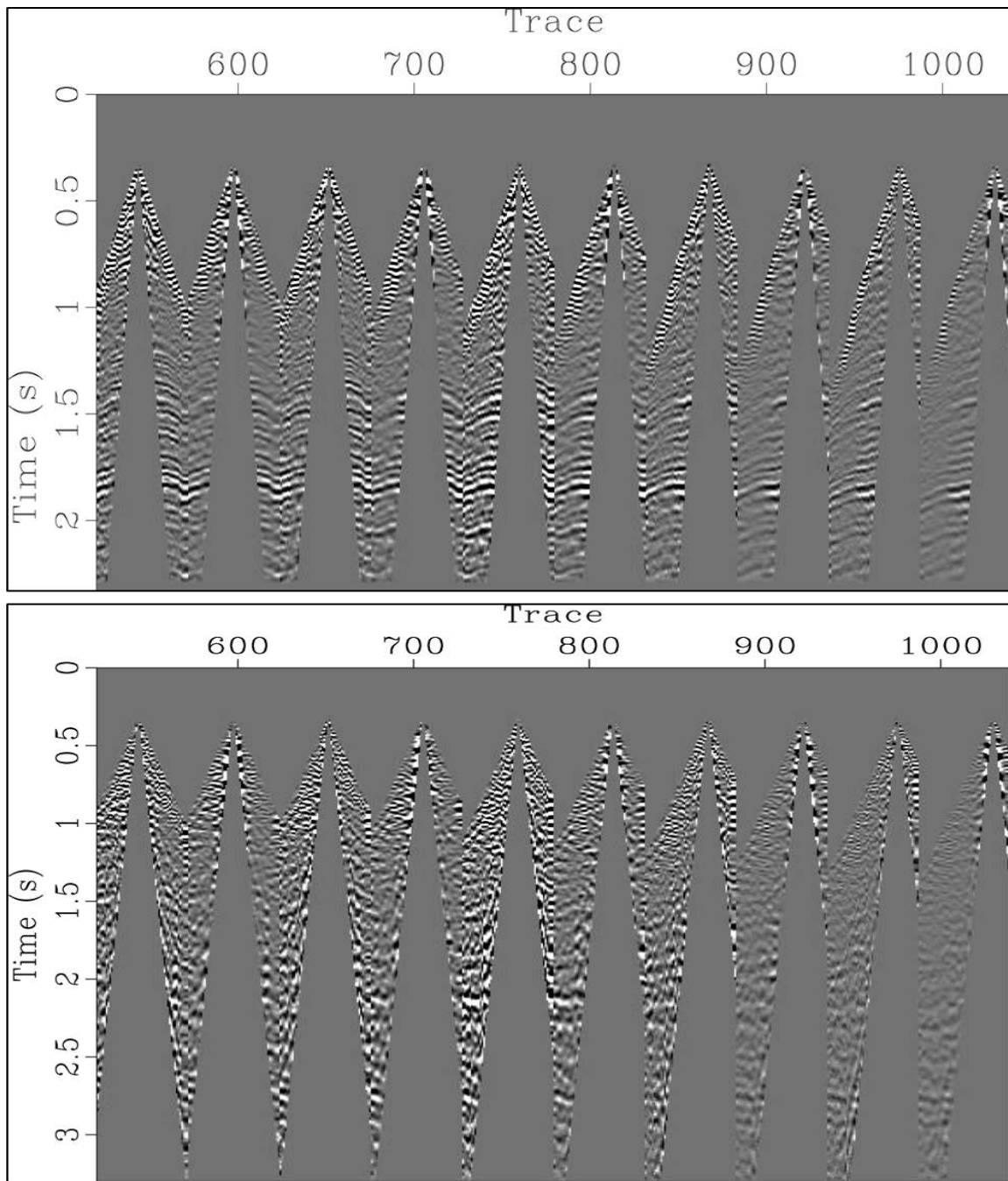


Figure 3.10: Shot-gather records of vertical component (top) and radial component (bottom) for E-W 2D line. Note the poor quality of the radial component data in this section.

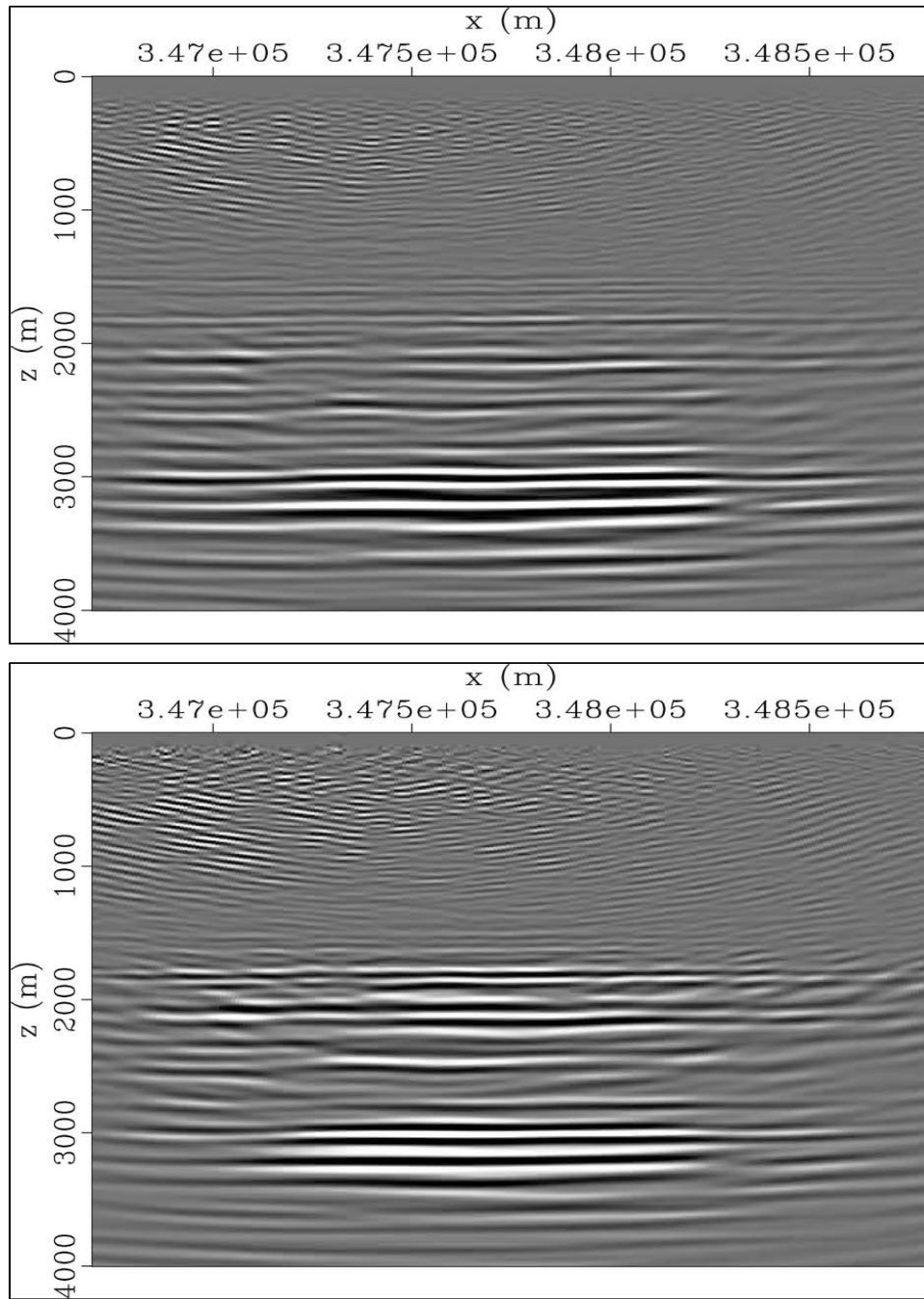


Figure 3.11: Result of ERTM using only the vertical component for E-W 2D line.

Top: P-P image.

Bottom: P-S image.

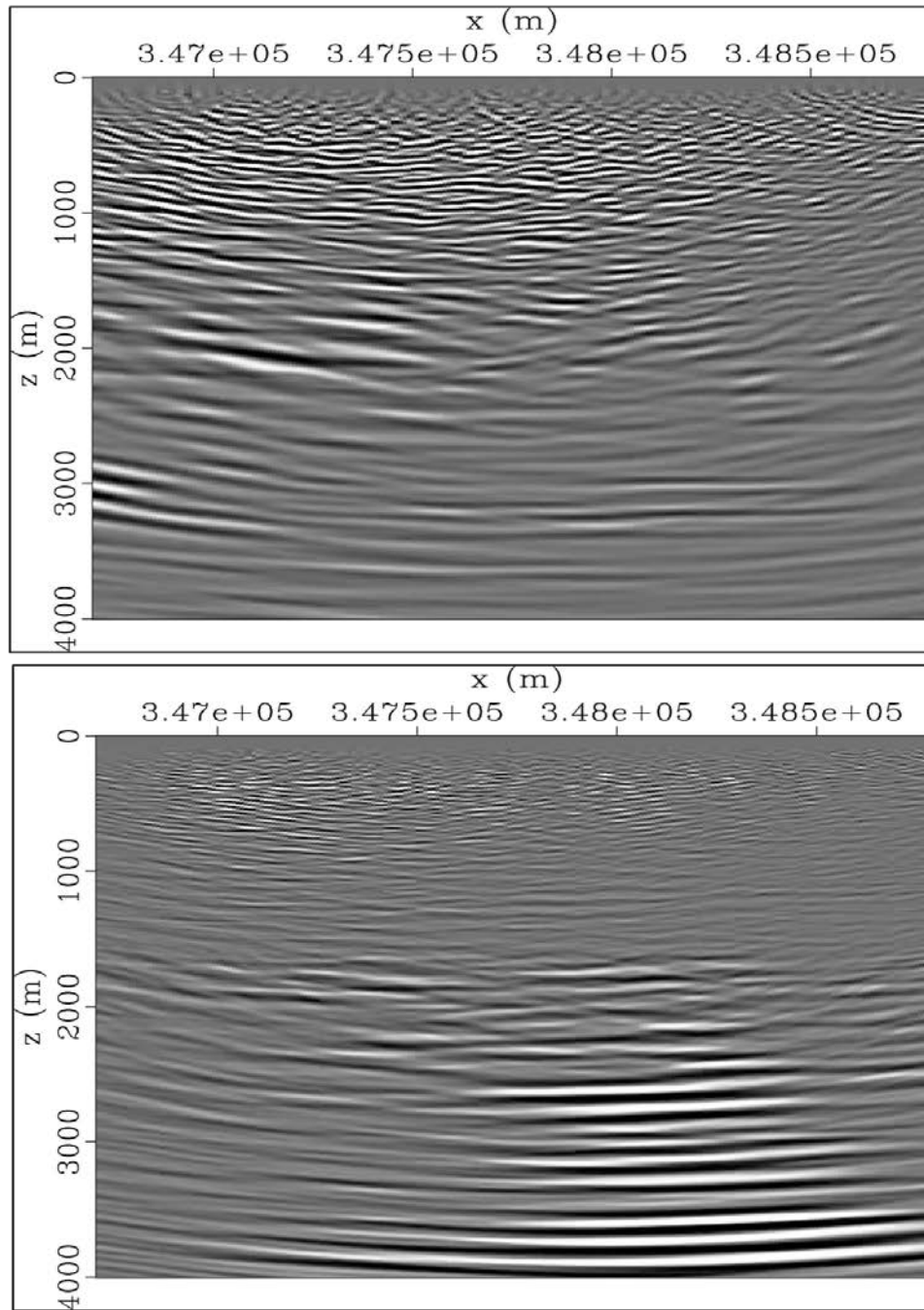


Figure 3.12: Result of ERTM the horizontal component data only for E-W 2D line.

Top: P-P image.

Bottom: P-S image.

3.5 Impact of attenuation

One main subsurface parameter that can help us understand the reason for wave-mode leakage in the field data migrated images is the anelastic attenuation of propagating seismic waves, which is quantified by quality factor (Q). Attenuation affects the seismic wave main characteristics of frequency, amplitude and phase. Accordingly it will affect the quality of cross-correlation process using the imaging conditions proposed in this thesis, as elastic reverse-time migration assumes no attenuation in the subsurface. Impact of attenuation on multi component data frequency and resolution was addressed by Bale and Stewart (2002), where they investigated how different P-wave and S-wave (Q) will result in event correlation errors in data domain. Recently, the issue of anelastic attenuation urged the need for developing (Q) estimation techniques for P-S waves (e.g., Wang et al., 2009; Gaiser, 2013) and required implementing attenuation compensation during migration by adopting visco-elastic based algorithms (Wang and McMechan, 2015; Zhu and Sun, 2017), as well as within the framework of full waveform inversion (Xue et al., 2016).

To develop an idea about the effect of different attenuation factors of P-P waves (Q_p) and P-S waves (Q_s) on the proposed ERTM scheme, we applied the ERTM scheme on synthetic example of visco-elastic data. We built a simple 2D model with ten shots and ten receivers, representing three layers with different V_p and V_s velocities and constant Q_p and Q_s values along the model. Data recorded consists of both the vertical and radial components. The source wavelet has a dominant frequency of 15 Hz.

In order to distinguish between P-P reflector and related P-S reflector, we added perturbations to the V_s model used in data migration. That placed the reflectors on different depth. Figure 3.13 shows the true velocity models used in creating the data, and the perturbed V_s model used in migration. The related elastic images (with no attenuation) are shown in Figure 3.14, where the true P-P and P-S images are compared to the perturbed images.

Data was generated for four different attenuation cases. The first case of no attenuation represents a reference image to be compared to the other cases, where ($Q_p = Q_s = 100$). Second case represents attenuation of S-waves where ($Q_p = 100$) > ($Q_s = 20$). Third case represents attenuation of P-wave where ($Q_p = 20$) < ($Q_s = 100$). The last case represents equal attenuation of both waves where ($Q_p = Q_s = 20$). Figure 3.15 display the results of the four cases, where the main attenuation-related differences between the images are pointed by black arrows.

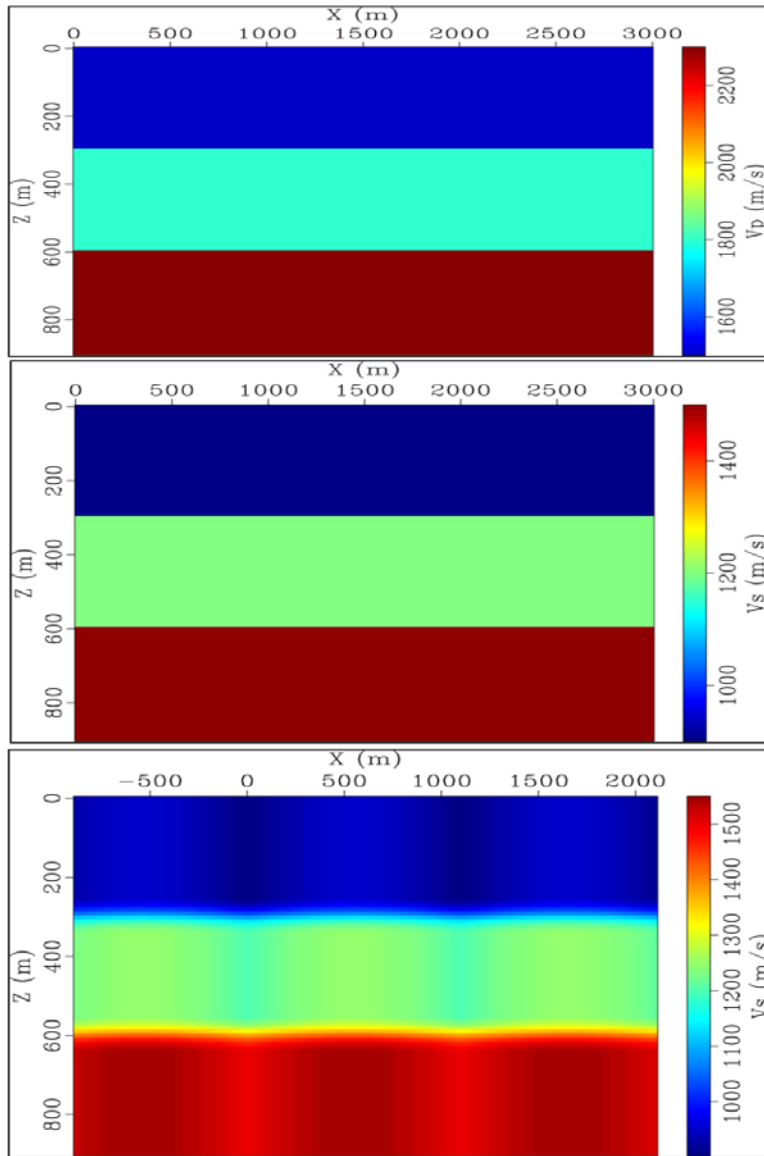


Figure 3.13: Velocity models of synthetic 2D model used to study the effects of attenuation.

Top: P-wave true velocity model.

Middle: S-wave true velocity model.

Bottom: S-wave velocity model with perturbations to enable distinguishing P-S reflectors on images.

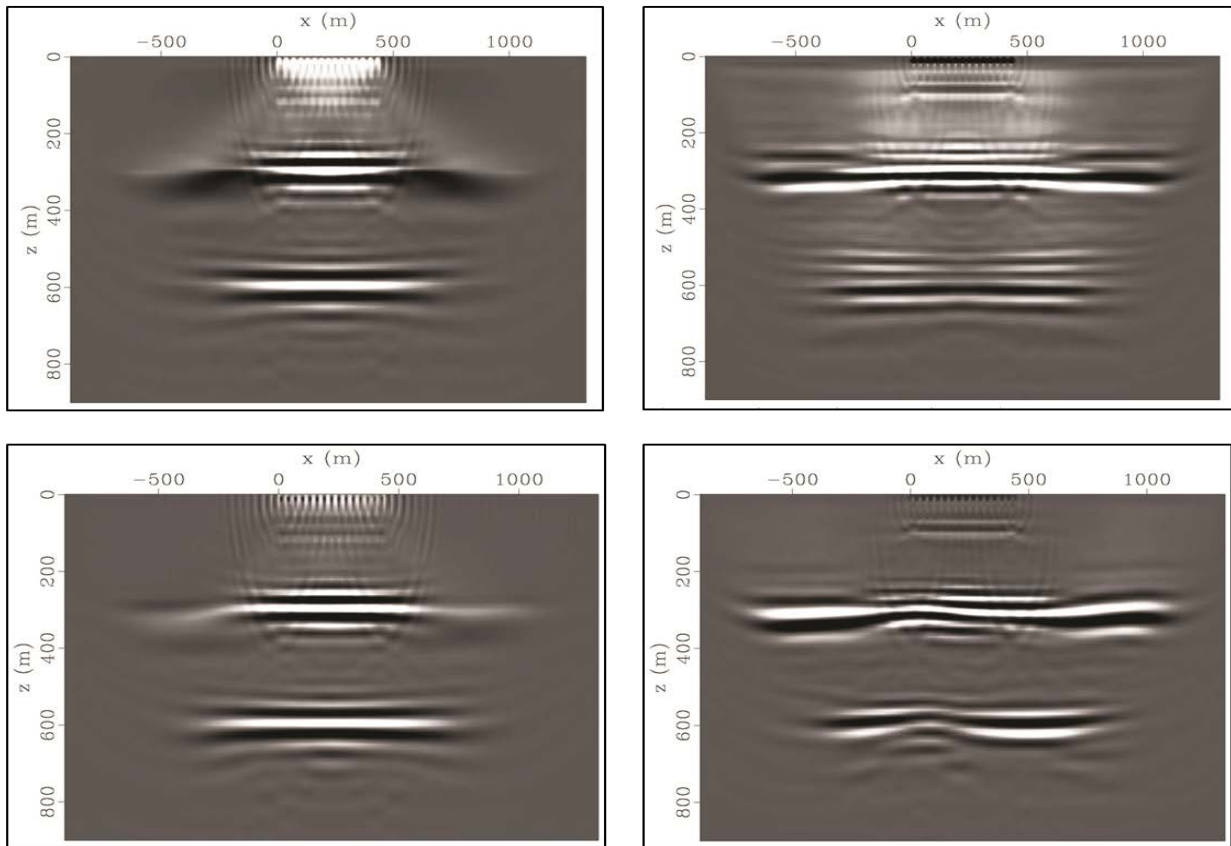


Figure 3.14: Migrated images of synthetic model in case of elastic data ($Q_p = Q_s = 100$).

Top: P-P (right) and P-S (left) images using true velocity models (True images).

Bottom: P-P (right) and P-S (left) images migrated using perturbed S-wave velocity model (Reference images).

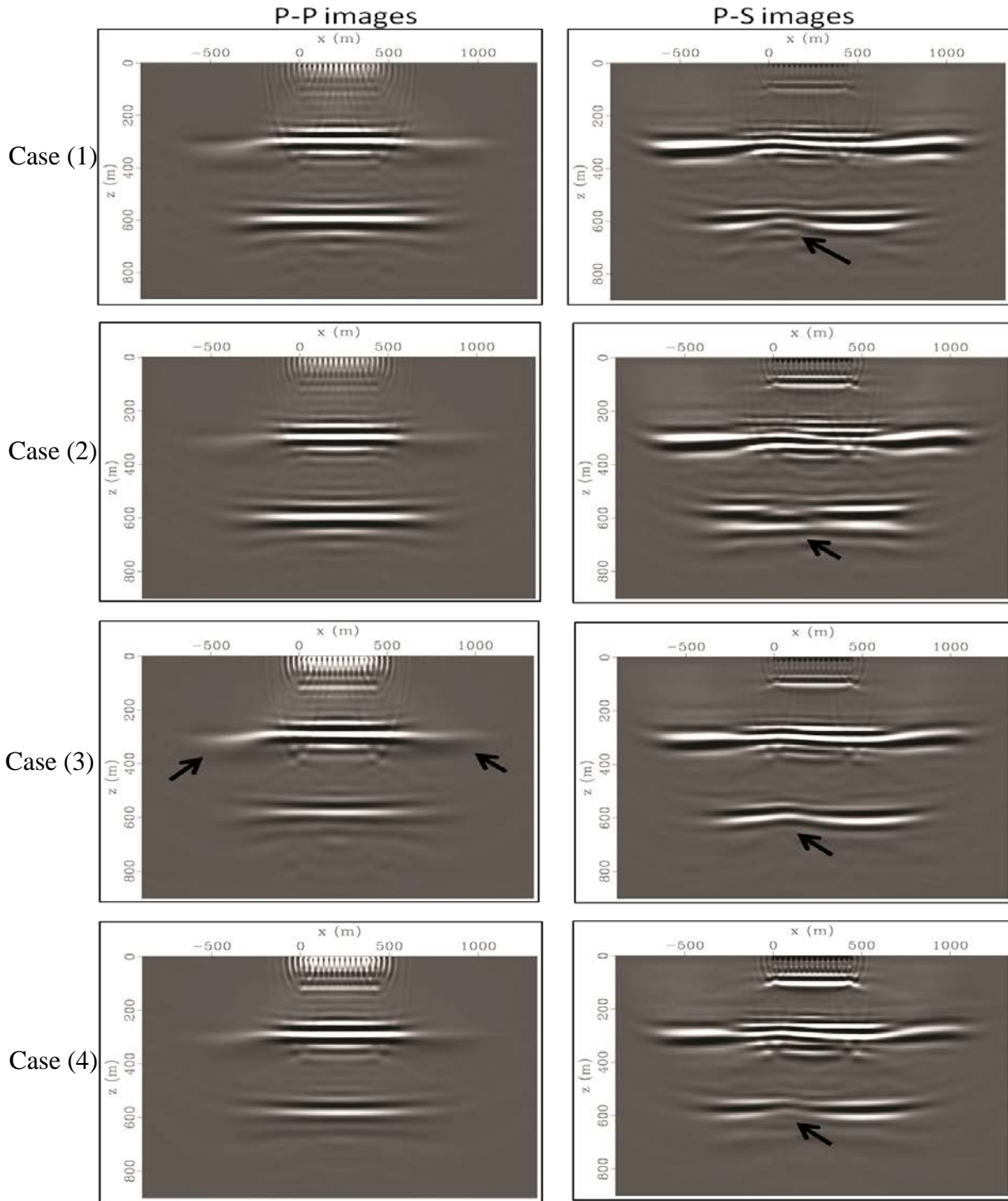


Figure 3.15: Migrated images with different attenuation scenarios.

From top to bottom; 1st case ($Q_p = Q_s = 100$); 2nd case ($Q_p = 100, Q_s = 20$); 3rd case ($Q_p = 20, Q_s = 100$); 4th case ($Q_p = Q_s = 20$). The black arrows refer to effect of attenuation on the migrated

images.

Comparing the images of different attenuation cases to the reference image, we can observe the following:

- In case of equal attenuation factors ($Q_p = Q_s$), the migrated images are accurate with minimum cross-talking between different wave-modes, as in case (4).
- In case of different attenuation factors ($Q_p \neq Q_s$), the image of wave-mode that is more attenuated will suffer from leaked signal of the less attenuated wave-mode, As shown in case (2) and case (3)
- Due to the shorter wavelength S-waves have compared to P-waves over the same frequency range, the leakage of P-P wave-mode is more destructive to the P-S image resolution than in the case of P-S wave-mode leakage into P-P image.
- The main reason we could be able to notify the Leaked P-S signal into P-P image in case (3) is the higher illumination coverage of P-S waves with shorter offsets due to the asymmetric wave propagation.

3.6 Discussion

In this chapter we investigated the issue of elastic wave-field imaging based on elastic reversed time migration and proposed imaging conditions that does not require polarity reversal correction or prior wave-mode separation. The proposed algorithm was applied on synthetic data example, producing successfully two separated P-P and P-S images with no cross-talking artifact, validating the applicability of the algorithm.

However, the results of field data example showed a leakage of P-P signal into P-S image. That required further examination of the results, where we applied the proposed migration scheme on each component data exclusively, expecting that way we will be able to quantify how much P-P and P-S signals were recorded by each component separately. The results of vertical component data migration gave nearly the same results as using both components, while radial component imaging showed very low signal in P-P image and reasonable signal in P-S image with high resolution. That directed us to question the vector fidelity of the radial component data.

Seeking better understanding of the reasons that can cause these leakage artifacts, we tested the algorithm over visco-elastic synthetic data to understand the effects of constant attenuation parameter on elastic imaging. The results of this test can help formulating an explanation of the field data results.

The difference in attenuation factor (Q) between P-P and P-S wave modes affect the result of migration, where the less attenuated wave-mode will perturb the more attenuated wave-mode. Whereas similarly attenuated wave-modes produce more accurate images. That point to the need for correlating the differential attenuation of both wave-modes and relative amplitude recovery scaling.

In realistic case, P-S waves suffer more attenuation than P-P, which provide an explanation for getting such a leakage of P-P signal into P-S image of Blackfoot dataset. Adding to that the possibility of poor coupling deteriorate the elastic signal fidelity. Also, the fact that P-S wave has shorter wavelength than P-P indicates that any leakage of P-P wave-mode will interfere with P-S signal in a constructive way, which produce a higher amplitude reflectivity with mixed resolution in P-S image as shown in Figure 3.7, or we should call it mixed image in this case. Therefore, low frequency component of P-S signal is important for P-S imaging, as it is less susceptible to the attenuation effect.

Accordingly, we believe in case of Blackfoot dataset, migration of different components exclusively will be the best way to produce accurate P-P and P-S images with no cross-talking artifacts. Otherwise we need (Q) compensation model and implementation of visco-elastic reverse-time migration, which for sure will produce more accurate results.

The P-S image of radial component data, migrated with initial velocity model, is incoherent and suffers from migration artifacts. In the next chapter we will show how accurate velocity estimation will enhance the image quality and reduce these artifacts.

4 Multi-component automatic velocity analysis via elastic reverse-time migration

4.1 Introduction

In general, the elastic parameters of subsurface can be obtained from conventional multicomponent data processing, based on uncertain approximations that we discussed earlier (section 1.5.2.2). The uncertainty of depth migrated images will always depend on the accuracy of the migration velocity fields. Velocity analysis of multi-component data is one of the biggest challenges in elastic imaging. The reason for that is the mutual-dependency between the accuracy of the initial velocity fields used in migration and the quality of the elastic migrated images that are used for velocity estimation. That requires a composite scheme that can interactively relate the accuracy of velocity models to the image quality and vice-versa. This is in fact an inversion problem.

Practically, a velocity model estimation technique should be based on the same level of theoretical and numerical approximations as the migration scheme, or there will be mismatch in algorithmic capabilities (Jones, 2015). A superior elastic migration algorithm as elastic reverse-time migration (ERTM) requires high accuracy velocity estimation technique based on wave-equation operators to obtain the optimum image. Without accurate velocity estimation the migration algorithm will suffer no matter how robust it is.

Automatic wave equation migration velocity analysis (WEMVA) is an iterative automatic velocity technique that can be described as a non-linear least-squares inversion of pre-stack seismic reflection data in the image domain, where an objective error function measuring the misfit in the image domain is iteratively minimized (Chavent and Jacewitz, 1995; Mulder and Ten Kroode, 2002; Shen et al., 2003; Sava and Biondi, 2004). The WEMVA method depends on what measure of misfit is used and which migration algorithm is employed to create the image (Sava and Vlad, 2008), where it can be based on the focusing of common-image point gathers (CIGs), maximizing stacking power or combination of both techniques. Weibull and Arntsen (2013) implemented an objective function for WEMVA based on differential semblance and similarity-index (stack-power) using acoustic RTM. In this chapter we will combine the ERTM scheme introduced in chapter 3 with WEMVA technique based on stack-power optimization as an objective function, in order to estimate optimal V_p and V_s migration velocity models.

One main issue of automatic velocity analysis techniques is the high computational cost. The proposed algorithm was tested successfully on 2D synthetic and field datasets. The results of 2D field data incited implementation of the method over 3D field data. The 3D results presented in this chapter are only related to V_p velocity inversion, whereas the 3D implementation of V_s velocity inversion is still in production phase by the time this thesis was delivered.

4.2 Theory

We test a method to automatically estimate enhanced V_p and V_s velocity models necessary for optimal imaging of P-P and P-S data using elastic reverse-time migration. Figure 4.1 illustrates in general the proposed workflow. In this method we use stack-power maximization (Chavent and Jacewitz, 1995; Weibull and Arntsen, 2014) as an objective function to measure the misfit error in migrated images. The objective function of stack-power (Equation 4.1) is then minimized using a gradient-based non-linear optimization method of L-BFGS (Byrd et al., 1995; Nocedal and Wright, 2000). The necessary gradients of the objective function with respect to V_p and V_s are computed using the adjoint-state method (Chavent, 2009).

The objective function is used to quantify the misfit error in the prestack depth migrated image. Stack-power maximization objective function is shown below; where I_p is the P-P image, I_s is the P-S image.

$$J = \frac{1}{2} \left\| \frac{\partial I_p}{\partial \mathbf{z}}(\mathbf{x}) \right\|^2, \text{ or } J = \frac{1}{2} \left\| \frac{\partial I_s}{\partial \mathbf{z}}(\mathbf{x}) \right\|^2 \quad 4.1$$

The non-linearity of the error function is one of the main challenges of the process. The application of the process on the image domain reduces such non-linearity to some extent. The minimization of misfit error function is an optimization problem, which we use a gradient-based optimization scheme to solve. In gradient based optimization the decent search directions are defined by the gradient of the misfit function in respect to the velocity parameter at each iteration step until convergence criteria is met, where the error is reduced. Using sophisticated optimization technique of L-BFGS method help in reducing the number of iterations required to successful convergence. We use B-spline parameterization (Dierckx, 1995) in order to allow local velocity variations and increase the numerical stability of the algorithm.

We also implement a regularization technique (Tikhonov et al., 1977) to constrain the non-uniqueness of the solution and limit the inherited errors during optimization.

Accordingly, at each iteration or line search step the objective function and gradient need to be evaluated. Given an initial input velocity model, the optimization algorithm will need the error function value and its gradient with respect to the velocity model in order to compute the step size that can result in minimizing the objective function. The process continues iteratively until it satisfies convergence criteria in order to find the best predictive model with reduced error, and an updated velocity model is produced. The stack-power maximization scheme is applied to each wave-mode image independently. Because of P-S imaging dependency on both V_p and V_s velocity fields, an enhanced V_p model must be obtained first.

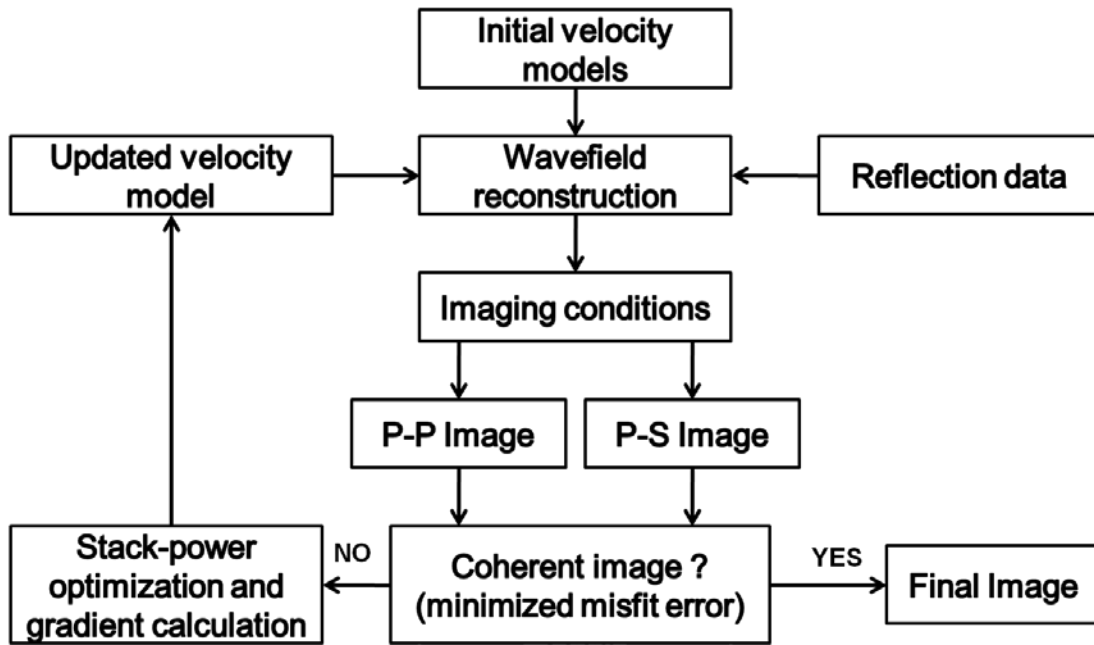


Figure 4.1: Proposed workflow for automatic migration velocity analysis.

4.3 Synthetic data example

In this section we use the same 2D Gullfaks synthetic model introduced before (section 3.3). The initial V_p model used for migration is a smoothed version of the true V_p model. The true velocity models and V_s perturbations are displayed in Figure 4.2. We apply stack-power maximization in order to account for the near-surface V_s perturbations and improve the P-S image. In this example we use for migration an initial V_s model that does not count for the near-surface velocity perturbations present in the true V_s model used for creating the data. Additionally, in the initial V_s model the water layer is substituted by a homogeneous layer with the ocean bottom velocities in order to reduce artifacts associated with generating strong surface waves during the receiver wave-field reconstruction.

The initial P-S migrated image shows clearly the effect of ignoring the near-surface velocity anomalies, where the reflectors are incoherent and inconsistent. Applying stack-power maximization procedure resulted in successfully detecting the near-surface velocity anomalies after 6 iterations, which enhanced the image. Figure 4.3 compares the initial and the enhanced P-S images after stack-power maximization. Vertical mute is applied to the velocity updates to limit it to be within 200 and 400 meters depth, reflecting our knowledge that the velocity perturbations are present in near-surface. By comparing the velocity updates detected by stack-power maximization shown in Figure 4.3 to the true perturbations shown in Figure 4.2, we can see that the detected updates are accurately placed horizontally, while the updates are distributed along the vertical mute we applied.

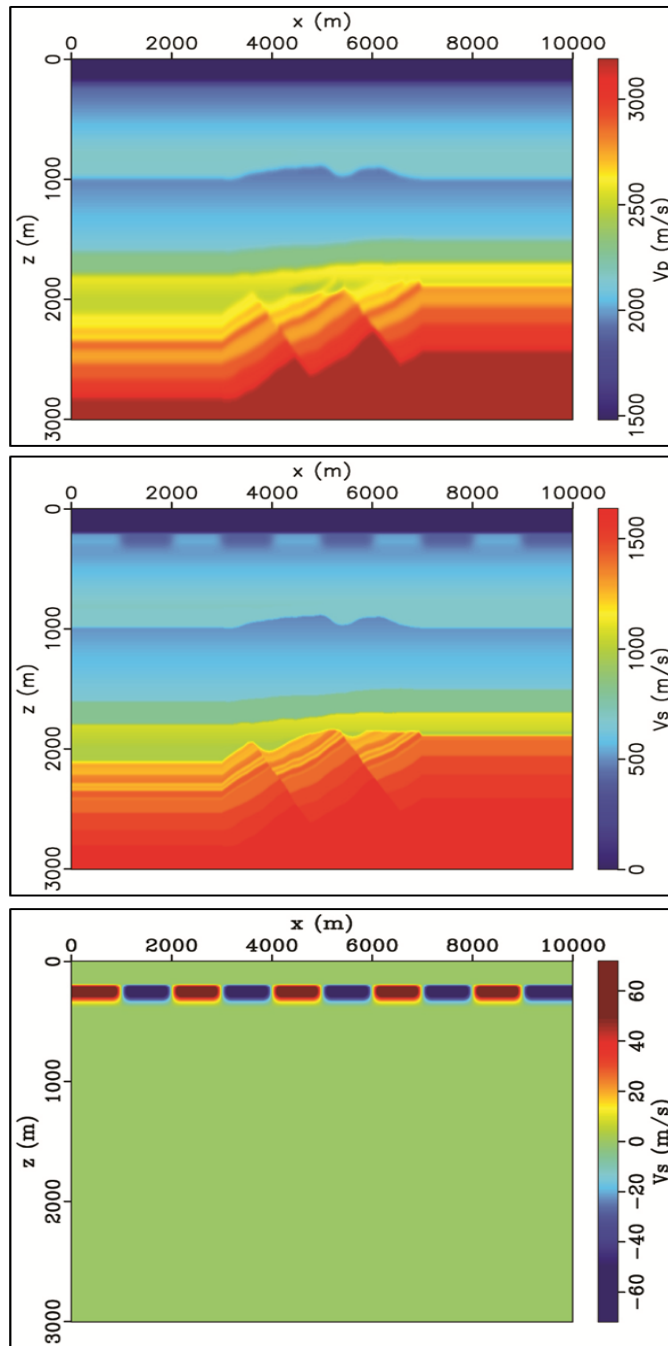


Figure 4.2: True velocity models used for creating Gullfaks synthetic dataset.

Top: True V_p .

Middel: True V_s .

Bottom: The near-surface perturbations of V_s model.

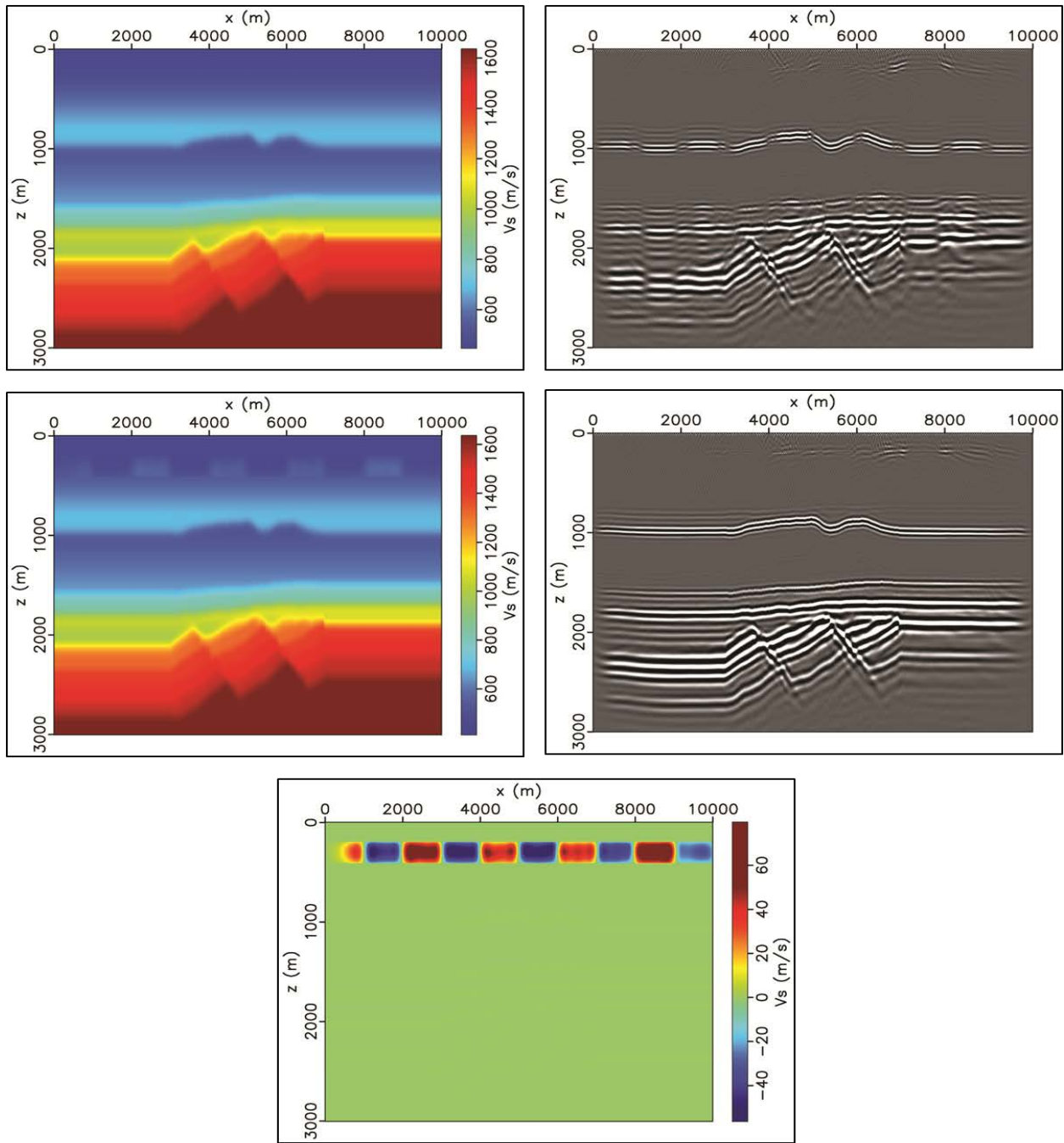


Figure 4.3: Migration V_s models and related images before and after stack-power optimization.

Top left: Initial V_s model.

Top right: Initial P-S image.

Middle left: V_s model updates after 6 iterations of stack-power optimization.

Middle right: Enhanced P-S image using updated V_s .

Bottom: Difference between final and initial V_s .

4.4 Field data example

4.4.1 2D example

For field data application we used the extracted 2D data described before (section 3.4). Due to the different attenuation of P-wave and S-wave, migration of each component is done exclusively in order to produce accurate P-P and P-S images with no cross-talking artifacts. No static corrections are applied, as one of the main goals of accurate velocity analysis is to estimate the near-surface velocity anomalies, which we expect stack-power optimization to compensate for. In all figures, z refers to the depth below 1000 m elevation datum. We assume constant density as it has no effect on travel time. The initial models used in this example are based on manual travel-time fitting using VSP data and ray-tracing from work done by Gulati et al., (1998). The source wavelet used in this procedure is Ormsby zero-phase wavelet with frequency range of 1-4-15-30 Hz and a time delay of 0.3 s as shown in Figure 4.4, hence the maximum frequency of the data used in stack-power maximization procedure is 30 Hz . Note the low-pass features of the source wavelet amplitude spectrum, which is essential to preserve the original input data bandwidth especially the low frequencies. In Figure 4.5 we show extracted wavelets of vertical and radial components input data for N-S section, estimated using fast Fourier transform. The velocity model resolution is based on 25 m^2 grid.

For N-S section, the initial velocity models used and the migrated initial P-P and P-S images are shown in Figure 4.6. We can see that in the initial P-P there are identifiable continuous reflectors, whereas the initial P-S image shows incoherent reflectors and suffers from artifacts. Migration of P-S data requires accurate V_p and V_s models, therefore V_p model should be estimated first. After estimating enhanced V_p model, we used the initial V_s/V_p ratio in order to scale V_p updates and add it to the initial V_s model. That approach might be geologically unrealistic, but it produces a model closer to the enhanced model we seek than the initial model we have from VSP data, which reduces the number of required iteration to produce the enhanced model. In other words, the initial model should be as close as possible to the true model to make the convergence achievable.

Figure 4.7 presents the results of P-P and P-S stack-power optimization. The final V_p model was obtained after 10 iterations. After that, using the scaled initial V_s model, the final V_s model was obtained after 9 iterations. The detected velocity updates are distributed along the whole vertical section of the model. The produced P-P image is more focused and sharpened, and the P-S image is significantly en-

hanced with coherent and consistent reflectors and less artifacts. Note that the images in Figure 4.7 have dominant frequency of 30 *Hz*.

One of the biggest challenges in imaging is the near-surface velocity anomalies. These anomalies affect the down-going and up-going wave propagation, which devastate the image quality. Usually, effects of near-surface velocity anomalies are solved by static corrections based on approaches which are susceptible to errors, while estimating the complex near-surface velocity field is the best solution for such challenge. In attempt to show the proposed method capabilities to detect the near-surface velocity and also to have a better idea of the non-uniqueness of the produced velocity models, we confined the velocity updates to near-surface area. This way we can consider the velocity updates are more geologically constrained to the near-surface velocity anomalies. Figure 4.8 shows the produced velocity updates and the related migrated images, where the velocity updates are limited vertically within 90 and 800 *m* depth. Note that the images displayed in Figure 4.8 have dominant frequency of 50 *Hz*. By comparing these results to the previous attempt of updating the whole model displayed in Figure 4.7, it can be observed that the produced images are enhanced, which indicates the non-uniqueness issue of the optimized solutions, it also must be considered that both images have different dominant frequency and the comparison might not be that fair.

The extracted 2D E-W section data of the radial component is not suitable for testing the technique as it has very poor signal to noise ratio. We show the result of stack-power maximization on the E-W section to estimate V_p model only. Figure 4.9 shows the updates detected by stack-power maximization and compares the initial P-P image to the enhanced one where the updated image is more coherent and structural elements as faults are sharpened.

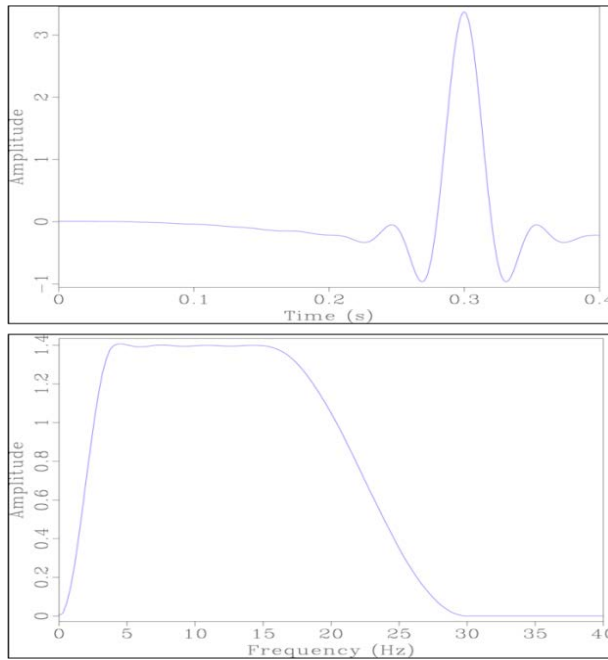


Figure 4.4: Source wavelet used in migration velocity analysis (Ormsby wavelet).

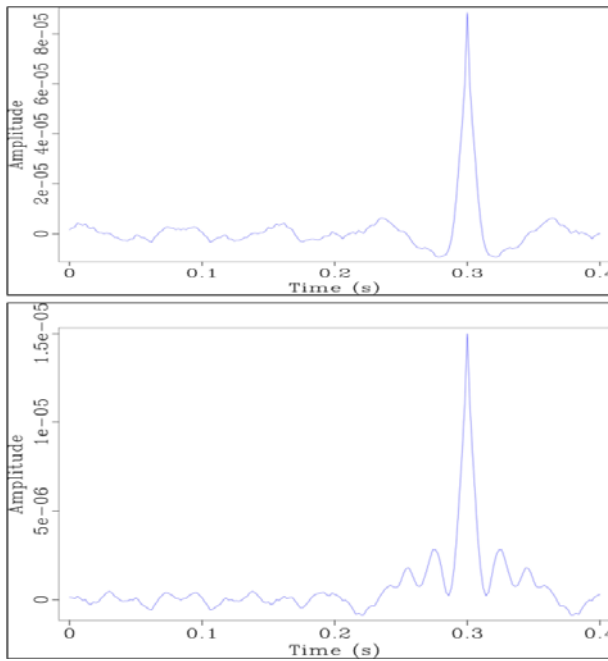


Figure 4.5: Extracted wavelets.

Top: From vertical component data.

Bottom: from radial component data.

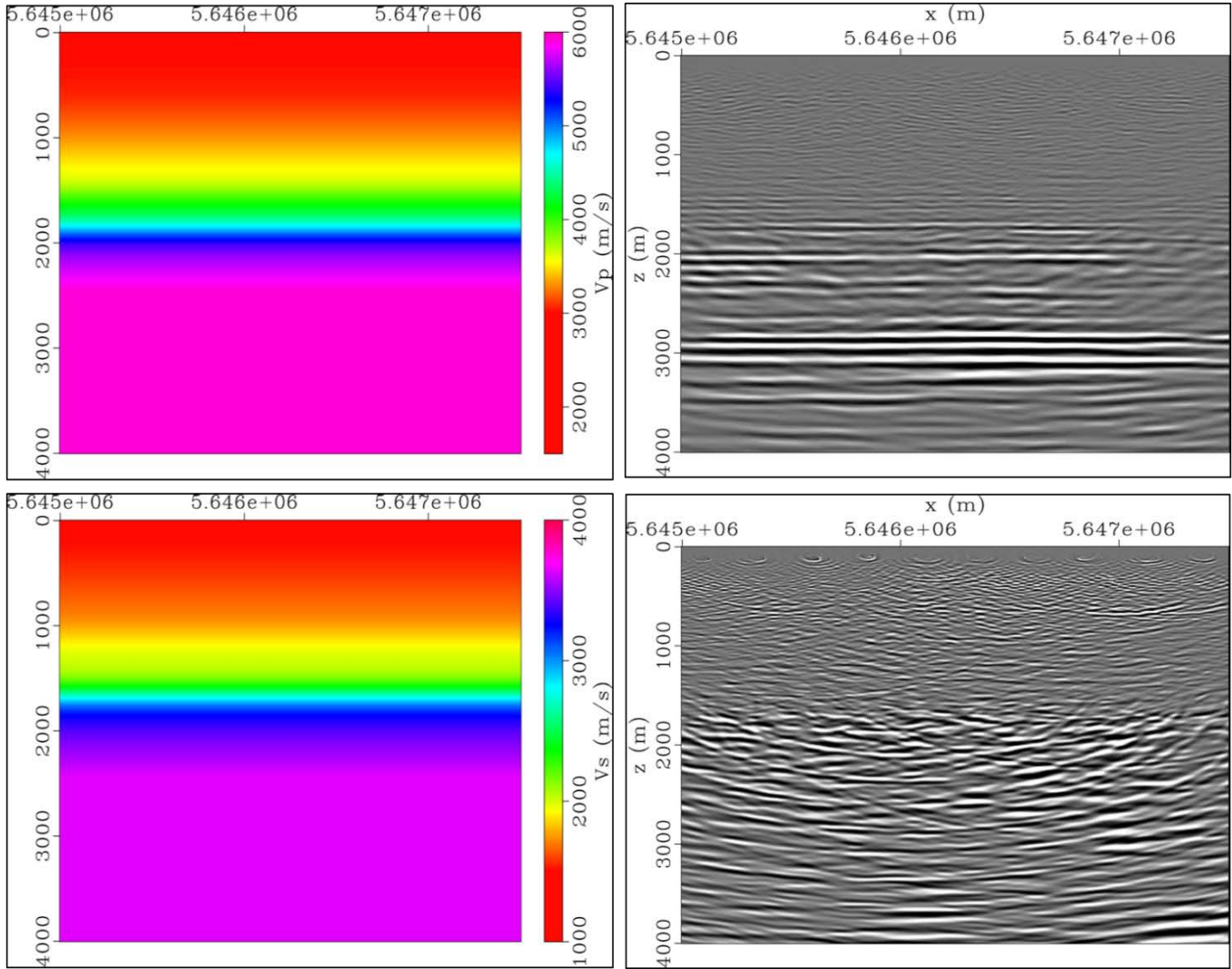


Figure 4.6: Initial migration velocity models and migration result for N-S section.

Top left: Initial V_p .

Top right: Initial P-P image.

Bottom left: Initial V_s .

Bottom right: Initial P-S image.

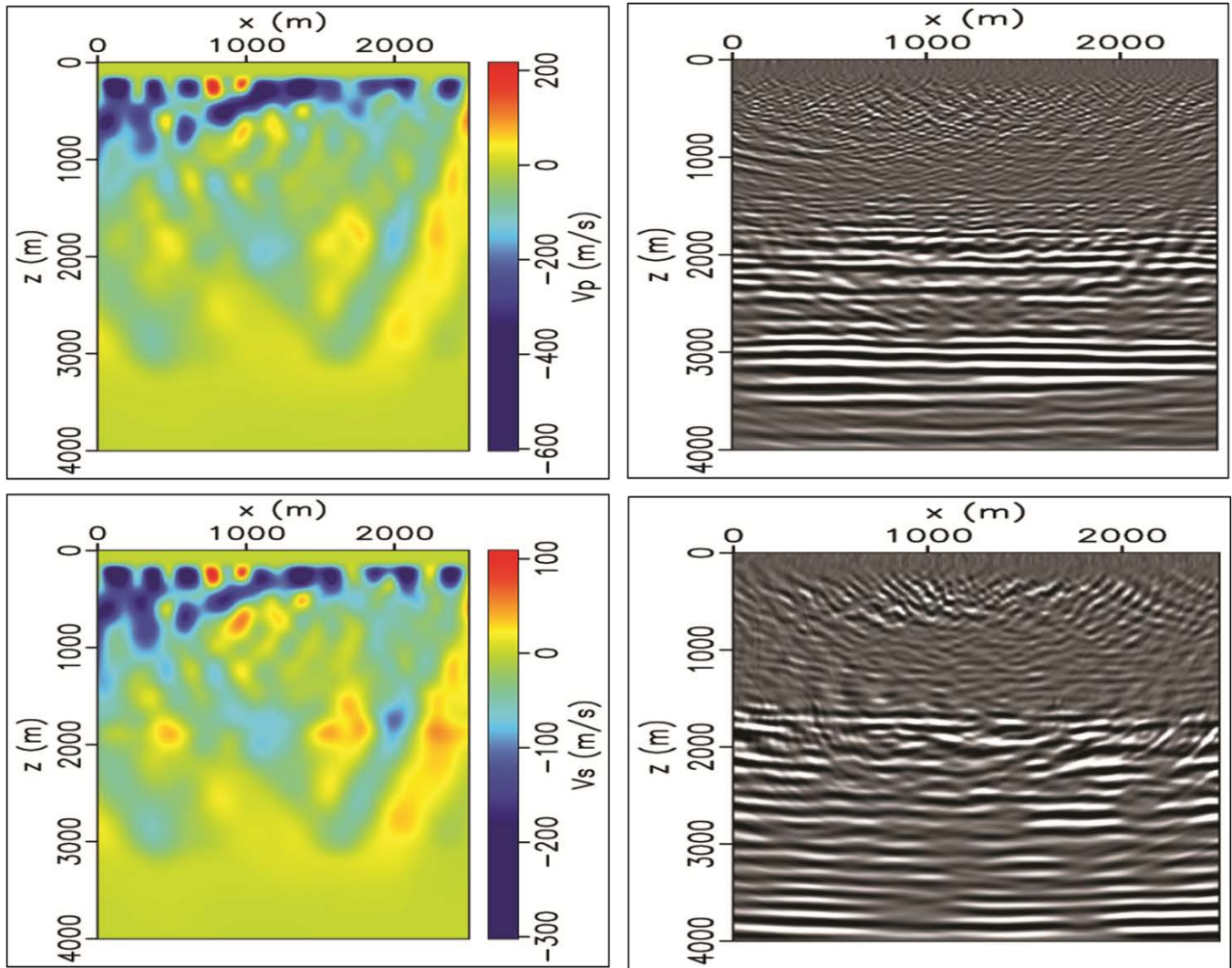


Figure 4.7: Results obtained from stack-power maximization procedure for N-S section.

Top left: V_p model updates after 10 iterations

Top right: Migrated P-P image using updated V_p model.

Bottom left: V_s model updates after 9 iterations.

Bottom right: Migrated P-S image using updated V_s model.

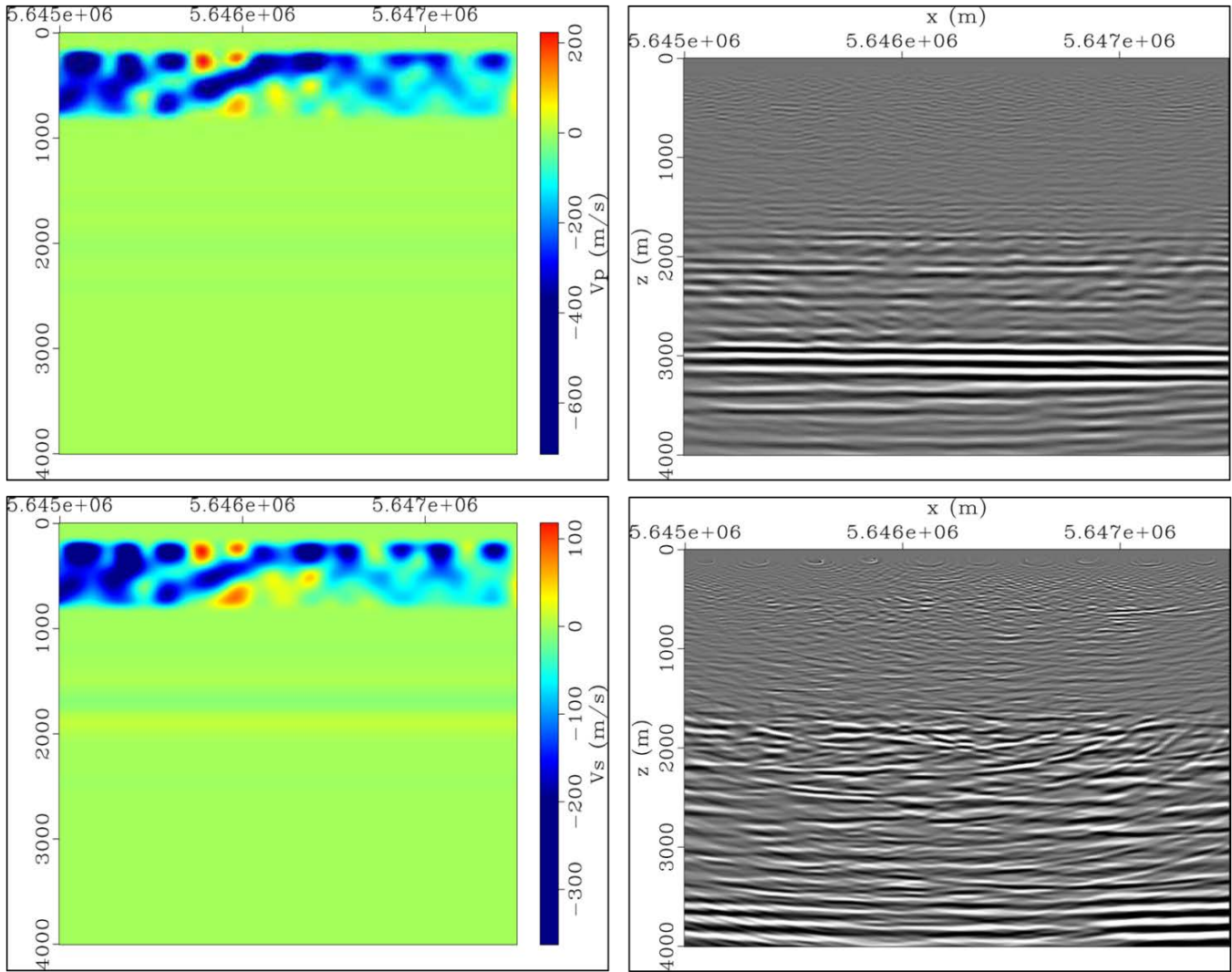


Figure 4.8: Results obtained from stack-power optimization procedure for N-S section where updates are limited to near-surface.

Top left: V_p model updates after 10 iterations.

Top right: Migrated P-P image using updated V_p model.

Bottom left: V_s model updates after 9 iterations.

Bottom right: Migrated P-S image using updated V_s model.

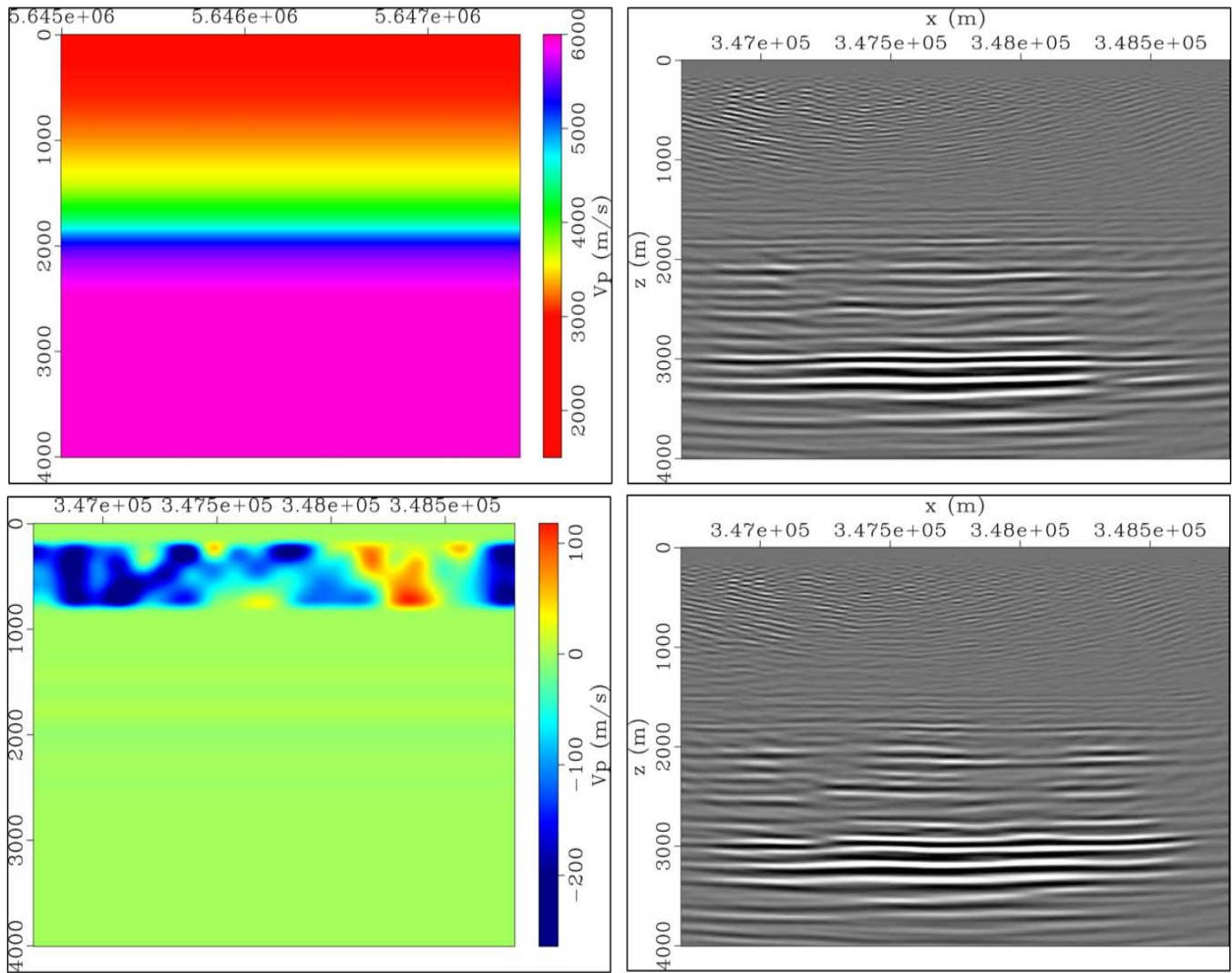


Figure 4.9: Results obtained from stack-power optimization procedure for E-W section .

Top left: Initial V_p model.

Top right: Initial P-P image.

Bottom left: Resulting V_p updates.

Bottom right: Enhanced P-P image.

Cycle skipping is the main problem facing velocity inversion techniques, where predicted and observed data differ by more than half a cycle and be out of phase (Sava and Biondi, 2004). Cycle skipping can steer the misfit function to get trapped in local minima or to diverge toward wrong direction producing incorrect models. In addition to having an initial model close as possible to the true model, low frequency content of the recorded data is a vital element for accurate velocity inversion. Low frequency signal increase the velocity inversion immunity toward cycle skipping, achieving better convergence and producing proper velocity models. As mentioned earlier, we applied a deconvolution of the recorded data with the impulse response of a 10 Hz geophone (Bertram and Margrave, 2010) in order to recover the low frequencies of the data with correct phase, which had its positive effects on velocity inversion.

In order to investigate the effect of low frequency data on stack-power optimization scheme, we tested the algorithm on pre-conditioned data with application of radial trace filtering (Henley, 1999) in order to remove coherent noise with application of low cut filter at 5 Hz. The radial trace filtering was applied on frequency range of 5-15 Hz. Figure 4.10 and Figure 4.11 show the amplitude spectrum of vertical and radial component data respectively, and show the difference before and after the low frequency enhancement and after low frequency filtering. It is obvious how the low frequency recovery technique enhanced the low frequency signal, and the applied filters reduced the low frequency signal, especially for the radial component data.

The results of stack-power maximization implementation on the data with low frequency filtered are shown in Figure 4.12. The initial P-S image shown in Figure 4.12 has fewer artifacts compared to the one shown in Figure 4.6, which can be related to the coherent noise removal. However, the missing low frequency has its effect on the P-S image overall quality reducing the image signal content, as expected in our previous discussion on P-S signal frequency relation to attenuation (section 3.6). After stack-power optimization implementation on the data with low frequency removed, the V_p updates after 10 iterations shows similar results to these of enhanced low frequency data, which indicate the advantage of applying the procedure in image domain. While for V_s inversion the process stuck after 7 iterations and produced lower accuracy model compared to the one produced for the enhanced low frequency data. For quantitative comparison between both cases, Figure 4.13 displays the numerical values of misfit error function for both V_p and V_s optimization. Note the high misfit error for V_s inversion with filtered low frequency and the insignificant enhancement along the iterations compared to the case with recovered low frequency content.

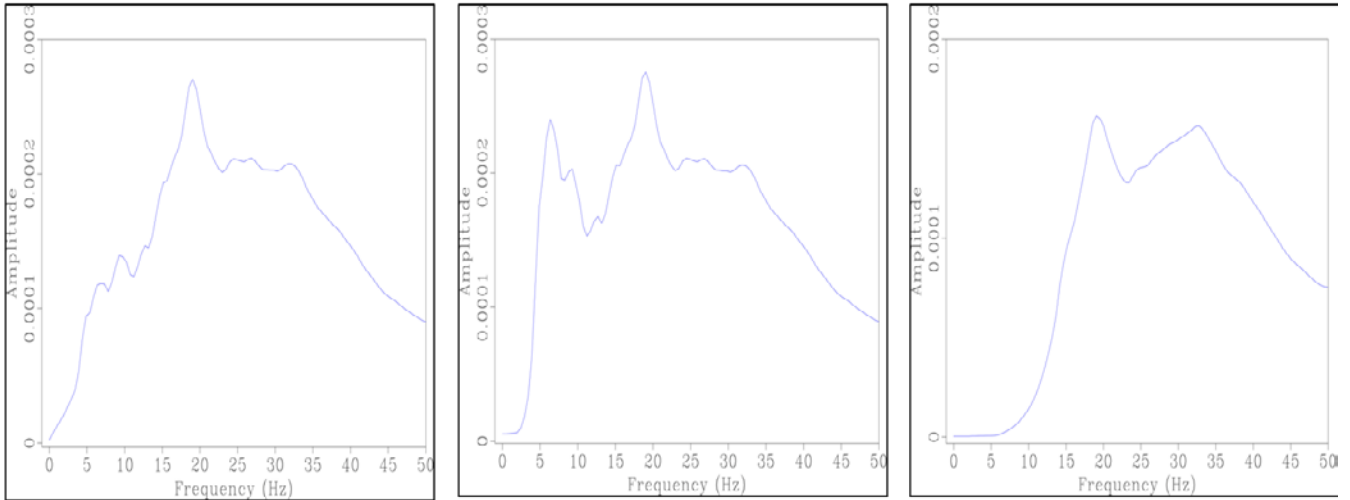


Figure 4.10: Amplitude spectrums of vertical component input data.

Left: Raw data.

Middle: Applied low frequency data recovery technique.

Right: Applied low-frequency coherent noise removal with low cut filter at 5Hz.

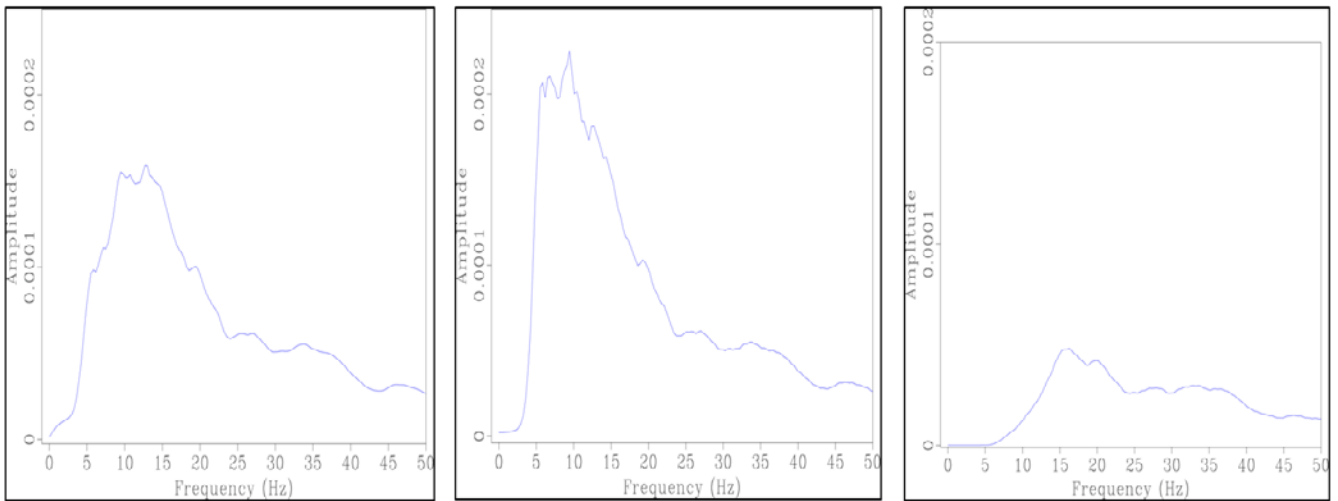


Figure 4.11: Amplitude spectrums of radial component input data.

Left: Raw data.

Middle: Applied low-frequency data recovery technique.

Right: Applied low-frequency coherent noise removal with low cut filter at 5Hz.

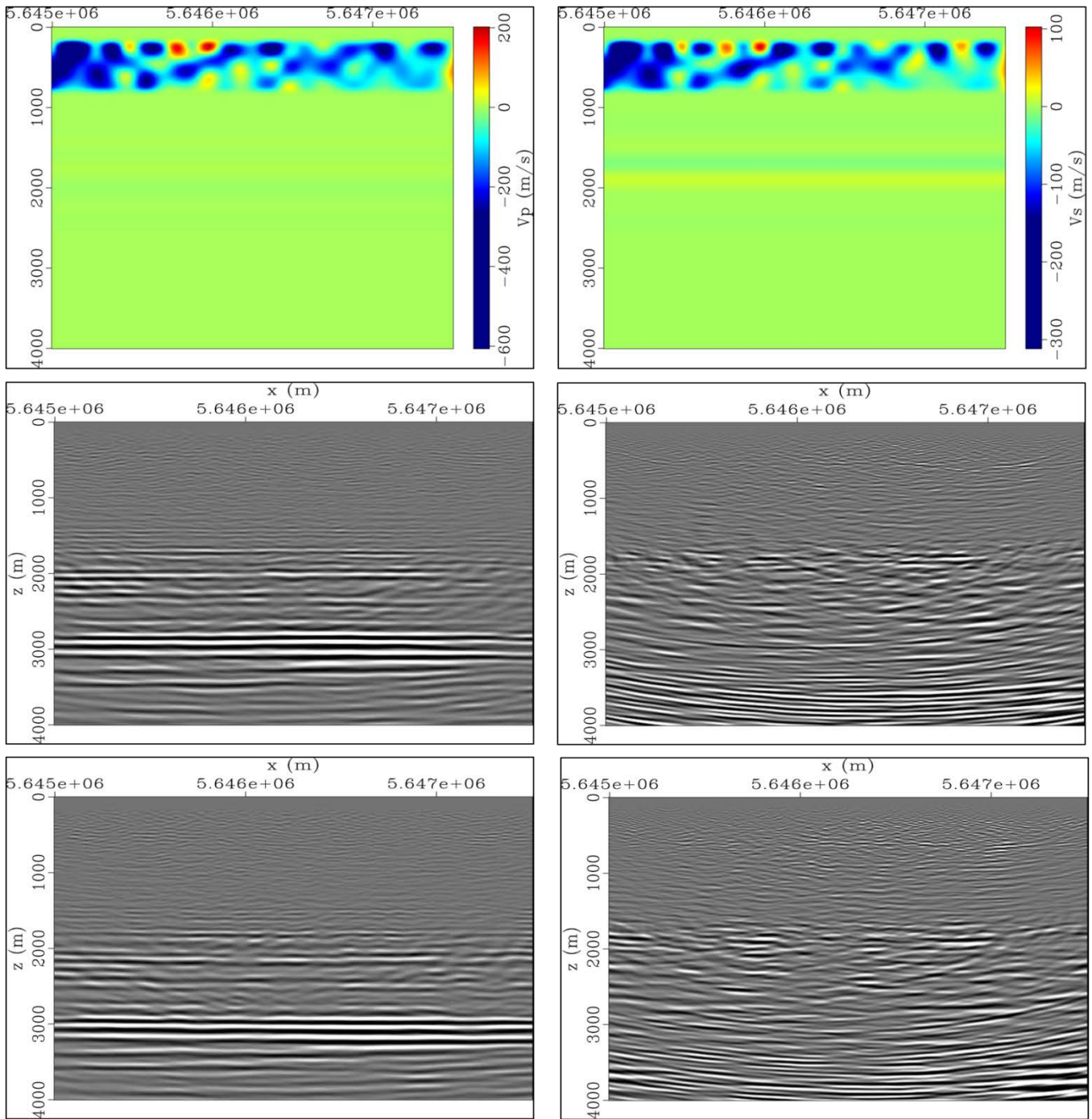


Figure 4.12: Results obtained from low-cut filtered data.

Top: V_p model updates after 10 iterations (left) and V_s model updates after 7 iterations (right).

Middle: Initial P-P image (left) and P-S image (right).

Bottom: Updated P-P image (left) and P-S image (right).

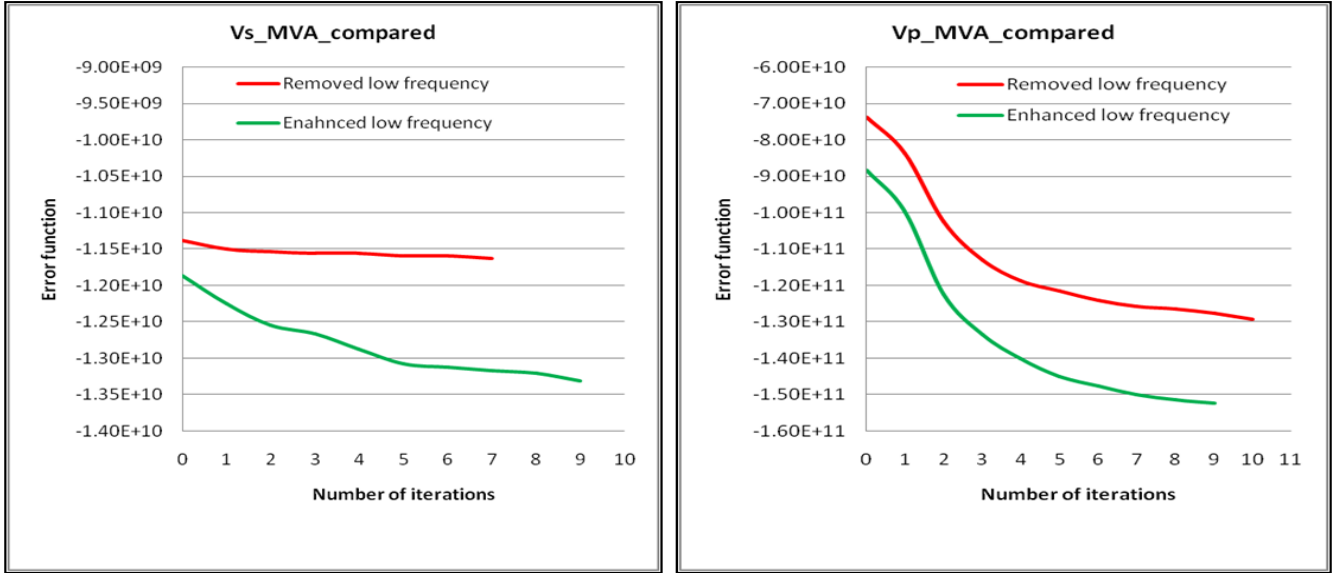


Figure 4.13: Comparison between the error function numerical values for V_s (left) and V_p (right) in cases of enhanced low frequency data (green curve) and filtering low frequency data (red curve).

4.4.2 3D example

The promising results of 2D data tests proved the efficiency of the algorithm and provided an outlook for optimizing the 3D implementation of the process. We here present the results of successful implementation of 3D V_p inversion for vertical component data with low frequency recovered. Unfortunately, 3D V_s implementation is still in progress due to the computational cost and compatibility issues of the available clusters and the algorithm, which required time consuming testing phase in order to stabilize the algorithm performance on the available clusters. In order to minimize the computational cost of the process, the data maximum frequency was set to 20 Hz, and it is required to start with low frequency data to avoid cycle skipping. The model grid resolution was 40 m in all dimensions. Adding to that the process was implemented for maximum depth of 3000 m. No physical limitations were set to the velocity updates distribution. The initial V_p model used is the same one used before for 2D example.

The produced V_p model obtained after 8 iterations is displayed in Figure 4.14 with the detected updates. The inline (easting section) and the cross-line (northing section) are equivalent to the 2D E-W and N-S sections respectively. By comparing the 3D results to the ones for N-S and E-W 2D sections, it can be observed how the better illumination and higher fold coverage improved the velocity inversion. The 3D results detected not just the near-surface anomalies but also the anomalies along the whole model in more geologically accurate manner. The results show the near-surface low velocity layer and what can be identified as near-surface channel system, and also show the effect of channel dominated sequence between 1500 and 2000 *m* depth.

Figure 4.15 compares the initial P-P migrated image to the enhanced P-P image using updated V_p model after 8 iterations. The maximum frequency of 20 *Hz* limited the image resolution, despite that we still can observe the enhancement of reflectors coherency and consistency. The edges of the image where the illumination is the lowest will be more susceptible to inaccurate imaging and cycle skipping. Both model grid resolution and data input frequency should be taken into consideration when analyzing the results. Further implementation to refine the model resolution by increasing the data frequency and reducing the grid size will produce higher resolution velocity models. Figure 4.16 presents the misfit error function numerical values along 8 iterations, showing lower misfit error values compared to those obtained from 2D implementation.

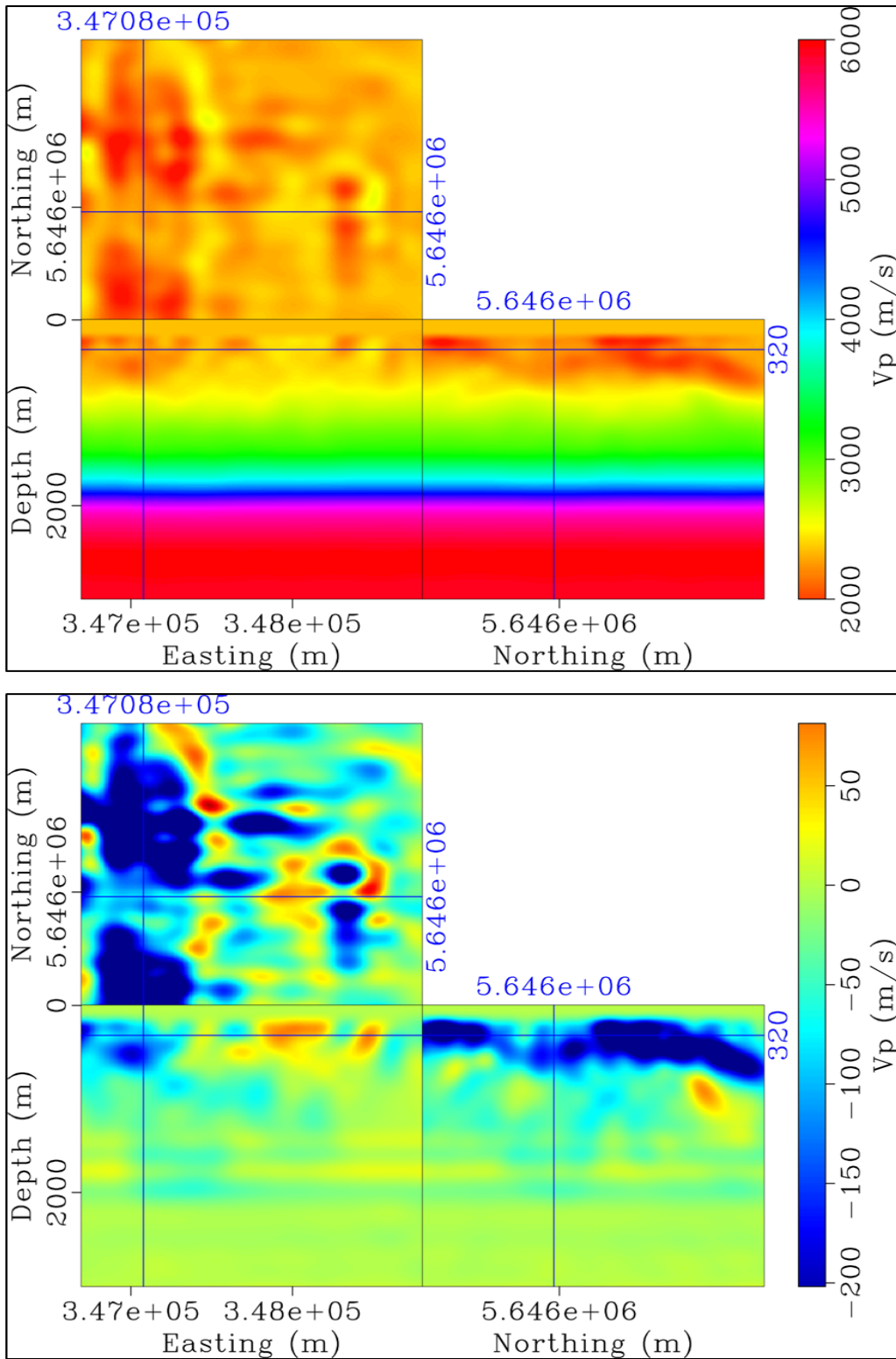


Figure 4.14: Produced V_p model and updates by 3D implementation of stack-power maximization after 8 iterations.

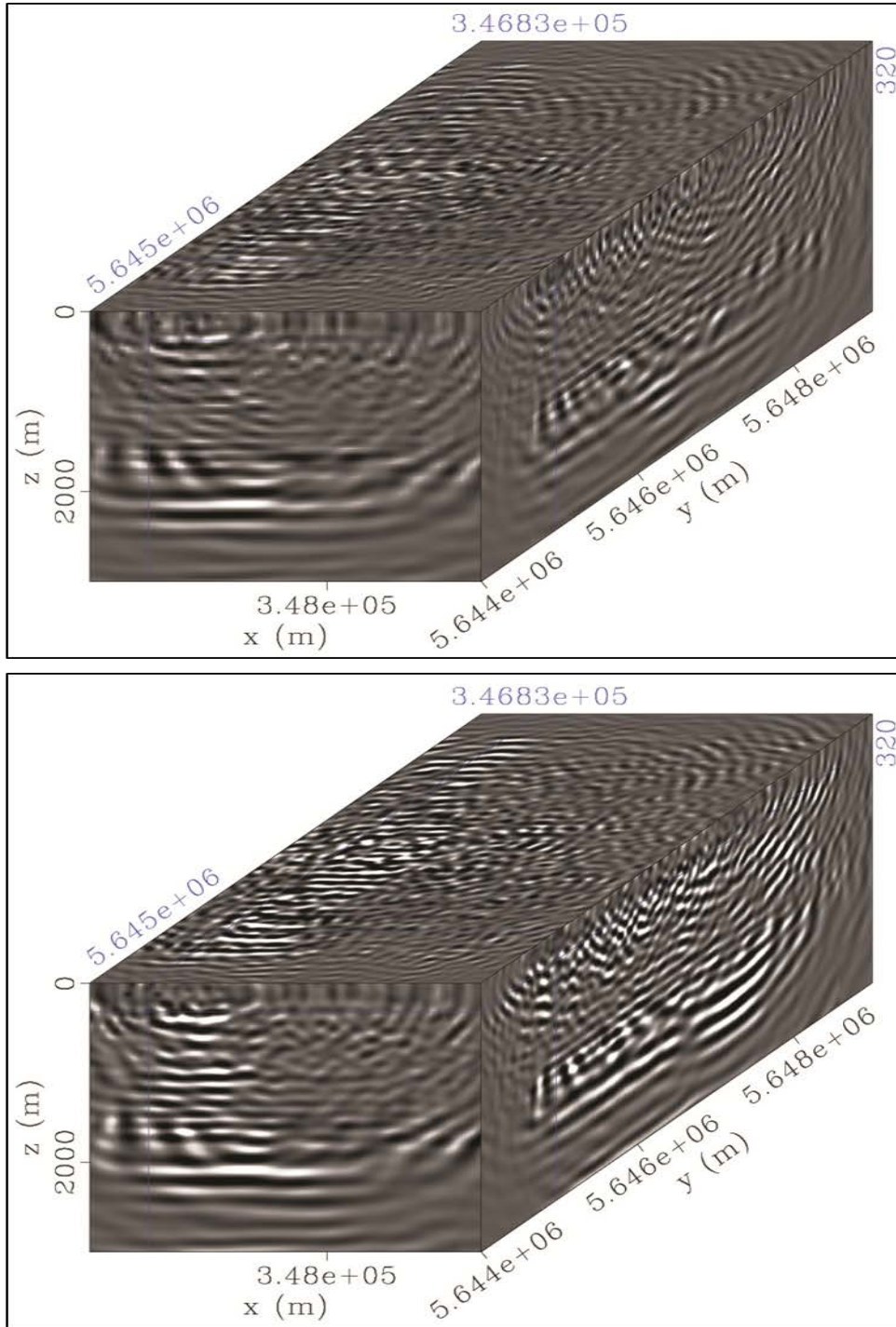


Figure 4.15: 3D display of migrated vertical component data with maximum frequency of 20 Hz.

Top: Initial P-P image.

Bottom: Enhanced P-P image after 8 iterations.

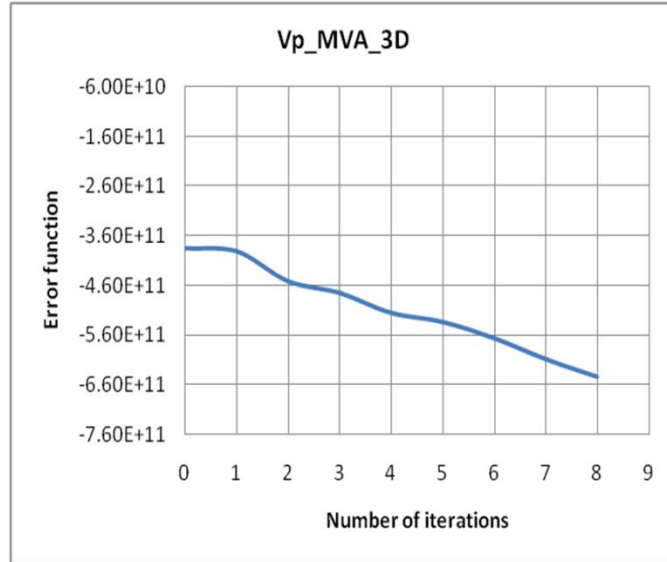


Figure 4.16: Error function numerical values for V_p 3D inversion.

4.5 Discussion

This chapter presents a composite scheme for multicomponent data velocity analysis based on elastic reverse-time migration and stack-power optimization in order to estimate optimal V_p and V_s migration velocity models. The automatic procedure of stack-power optimization works on focusing the seismic reflection data in the image domain based on gradient-based non-linear optimization to enhance the velocity field, avoiding manual picking, and reducing the non-linearity of the inversion problem. The key factor in optimization problems is the method followed to define the error or quantify it. In stack-power maximization we do not fit observations; we maximize the stack-power of the observed data itself.

The synthetic and field data examples presented in this chapter demonstrate the capabilities and challenges for the proposed scheme. The method is stable and capable of successfully providing enhanced velocity models using only raw data with very basic pre-conditioning such as ground roll mute and low frequency recovery. Even in 2D examples with low fold coverage the method still provide promising proof of concept results. It is hard to say that the produced models are geologically accurate, but we can definitely say that the produced models are optimized and the related images are enhanced. With better illumination and higher signal to noise ratio in the case of 3D implementation, the method gave outstanding results despite the coarse model cell size of 40 m^3 .

Several issues must be taken into account when implementing the proposed migration velocity analysis scheme;

- Data input quality (signal to noise ratio) and the low frequency vital rule in velocity analysis and P-S imaging.
- Sensitivity toward the initial model quality and smoothness, as it should be as close as possible to the true model to make the convergence achievable.
- The non-linearity of the objective function and the possibility of cycle skipping or over-fitting the data where the misfit function can get trapped in local minima or diverge toward wrong direction producing incorrect models.
- The non-uniqueness of the optimization solution can lead to several models that produce the same enhanced image without regard to geological accuracy.
- The model resolution (gridding) and its effect on the detectable velocity variations.
- The computational cost of the method.

These issues raise the need for amplitude-friendly and low frequency preserving processing techniques to de-noise and de-multiple the data, beside the need for good initial model in order to overcome cycle skipping and achieve reasonable convergence. The model gridding resolution represent a physical constrain that can be tackled by increasing the computational resources and the efficiency of the algorithm. Adding geological constrains and acquiring subsurface information through well data will definitely reduce the spectrum of possible non-unique solutions and produce geologically accurate model. Despite the computationally expensive implementation of the process, it can be considered as time and cost saving approach, where the process is capable of producing enhanced velocity models and accurate subsurface elastic images ready for interpretation using raw data directly, as demonstrated by the field data results, which can substantially reduce the processing cycle time and cost.

The produced images from stack-power optimization procedure are substantially improved with coherent and consistent reflectors. However, the P-P and P-S depth images should show depth consistency, which is not achieved by the stack-power optimization procedure. This issue can possibly be mitigated

using a better initial V_s/V_p ratio, or by using an objective function that enforces co-depthing P-P and P-S reflectors. In the following chapter we will discuss an approach for P-P and P-S images co-depthing.

5 Tomographic co-depthing of P-P and P-S images based on elastic reverse-time de-migration

5.1 Introduction

Correlating P-P and P-S migrated images in time domain based on conventional techniques is highly uncertain and ambiguous process which requires additional support of well logs and VSP data. The main reasons for that are the differences in P-S waves propagation time compared to P-P waves reflected from the same subsurface event, and the different reflectivity characteristics of P-S waves compared to P-P waves where the same subsurface event can have different response on both wave-fields. In addition to that, applying different static shifts on different receiver components increase the possibility of miscorrelation. Several publications aimed to mitigate the issue of P-P and P-S event registration based on analyzing V_p/V_s ratio (e.g., Garotta, 1985; Gaiser, 1996; Ogiesoba and Stewart, 2003; DeAngelo et al., 2003; Nickel and Sonneland, 2004). An example for the difficulties related to P-P and P-S events correlation based on conventional pre-stack time migration is discussed in section 2.3 of this thesis.

Using depth migration algorithm is the logical solution for the problem of time correlation ambiguity. However, even with overcoming the previous mentioned difficulties, the depth correlation will still be highly uncertain without accurate imaging of distinct P-P and P-S images that avoid wave-mode leakage, beside the main critical factor of velocity model accuracy which dominantly control the reflectors depth. An aspect of accurate velocity analysis for multi-component data is yielding depth consistent migrated P-P and P-S images where geologically equivalent reflectors are registered on the same depth. The issue of joint P-P and P-S velocity analysis to produce consistent P-P and P-S depth images was investigated by many authors (e.g., Herrenschmidt et al., 2001; Grechka et al., 2002; Broto et al., 2003; Szydlik et al., 2007).

Successful P-P and P-S co-depthing requires a comprehensive workflow that combine robust imaging and accurate velocity analysis algorithms. In addition to that, there is a need for a technique that can communicate the two depth images information in a common domain, independently from the migration velocity models accuracy. De-migration technique is capable of that, where it works as a proxy between the migrated image and the seismic data domain, enabling seismic data recreation from migrated images. De-migration method (Loewenthal et al., 1978) is an important concept with many useful applications in seismic exploration (Zhang and Duan, 2012; Leader and Biondi, 2014). Foss et al., (2005) presented co-

depthing tomographic approach for estimating the velocity model that produces depth consistent P-P and P-S images, and used migration/ de-migration technique as part of their scheme to obtain time information of the key reflectors of the P-P and P-S images. De-migration based on RTM has been used to recreate data from seismic images in the context of velocity analysis (Chauris and Benjema, 2010; Weibull and Arntsen, 2013) in optimized schemes for WEMVA.

In this chapter, we present a velocity analysis scheme that can be used to co-depth the reflectors of P-P and P-S images constructed by elastic reverse-time migration. The tomographic co-depthing method is based on manual interpretation of key reflectors in the initial P-P and P-S images and then automatically determining the velocities that will optimally match these reflectors in depth using target image fitting technique. In this process we use a novel Born modeling/de-migration method to create synthetic single scattering P-S data from the interpreted reflector models. We test the method using 2D synthetic and field datasets.

5.2 Theory

For co-depthing P-P and P-S reflectors we use an optimization procedure of target image fitting (Biondi and Sava, 1999; Sava and Biondi, 2004). The objective of this optimization procedure is to match two images, one derived from P-P reflectors, and one derived from P-S reflectors. As a measure of fit between the images, we use a normalized correlation function (Choi and Alkhalifah, 2012);

$$J = \int dx \int dy \frac{\langle \mathbf{I}(x, y), \mathbf{I}^{target}(x, y) \rangle_z}{\| \mathbf{I}(x, y) \|_z \| \mathbf{I}^{target}(x, y) \|_z} \quad 5.1$$

where J is the total misfit value, and I and I^{target} are images to be matched. In this process, the target image (I^{target}) which represents the P-P image is kept fixed and acts as the observed image assuming that the P-P reflectors are accurately imaged, while the P-S image ($I_{(V_s)}$) acts as the forward modeled image to be optimized using equation 5.1 by perturbing V_s to achieve co-depthing of both images. We solve the optimization problem using a gradient based optimization method, where the gradient with respect to V_s is computed efficiently using the adjoint state method (Lions and Magenes, 1972; Plessix, 2006).

In principle, we could use the P-P and P-S images created with equation 3.1 and equation 3.2 as the target and forward modeled images, respectively. However, the P-P and P-S images have different characteristics in terms of wavelength, reflecting the different velocities of P- and S-waves. This could lead to a poor fit, and at the same time increase the chance of cycle skipping. Accordingly, in this workflow we carefully select and interpret key horizons in both the P-P and P-S depth images and use them to create two P-S images, representing the target and forward modeled images. To create the images to be matched we use the interpreted reflectors in a Born modeling/demigration procedure adapted to P-S reflectivity.

Born modeling/demigration procedure is used to make seismic data for one or more reflectors interpreted from the P-P and P-S depth images. Using these data, we are able to reconstruct migrated images of what we coined the target image (from the P-P reflectors) and the forward modeled image (from the P-S reflectors).

Given a reflectivity model ($R(\mathbf{x})$); we can create single scattering 3C P-S data using the following forward modeling equation:

$$\frac{\partial^2 u_i^{ps}}{\partial t^2}(\mathbf{x}_r, t; s) - \frac{\partial}{\partial x_j} \left[a_{ijkl}(\mathbf{x}) \frac{\partial u_l^{ps}}{\partial x_k}(\mathbf{x}, t; s) \right] = \frac{A_{ij}^{ps}}{\partial x_i}(\mathbf{x}, t; s) \quad 5.2$$

where u_i^{ps} is the displacement field for the P-S data at the receivers, and A_{ij} is a Born source for P-S data, and is given by equation 5.3, with u^s being computed using equation 3.3.

$$A_{ij}^{ps}(\mathbf{x}, t; s) = R(\mathbf{x}) \left[\varepsilon_{ij}^s(\mathbf{x}, t; s) - \delta_{ij} \varepsilon_{kk}^s(\mathbf{x}, t; s) \right] \quad 5.3$$

Following the Born modeling, the resulting data is migrated using equation 3.2 to create the P-S images for the target (I^{target}) and forward modeled images (I). These images are the starting point for the optimization procedure. Figure 5.1 illustrates the proposed workflow for co-depthing procedure.

It can be shown, at least for a single reflector, that this method is always going to achieve global convergence. The only condition for successful convergence is that the largest difference in depth

between the reflectors should be smaller than $\lambda/4$. Where λ is the wavelength of the S-waves at the reflector position. Since we are free to choose the temporal frequency of the source in the Born modeling procedure, it is always possible to satisfy this condition.

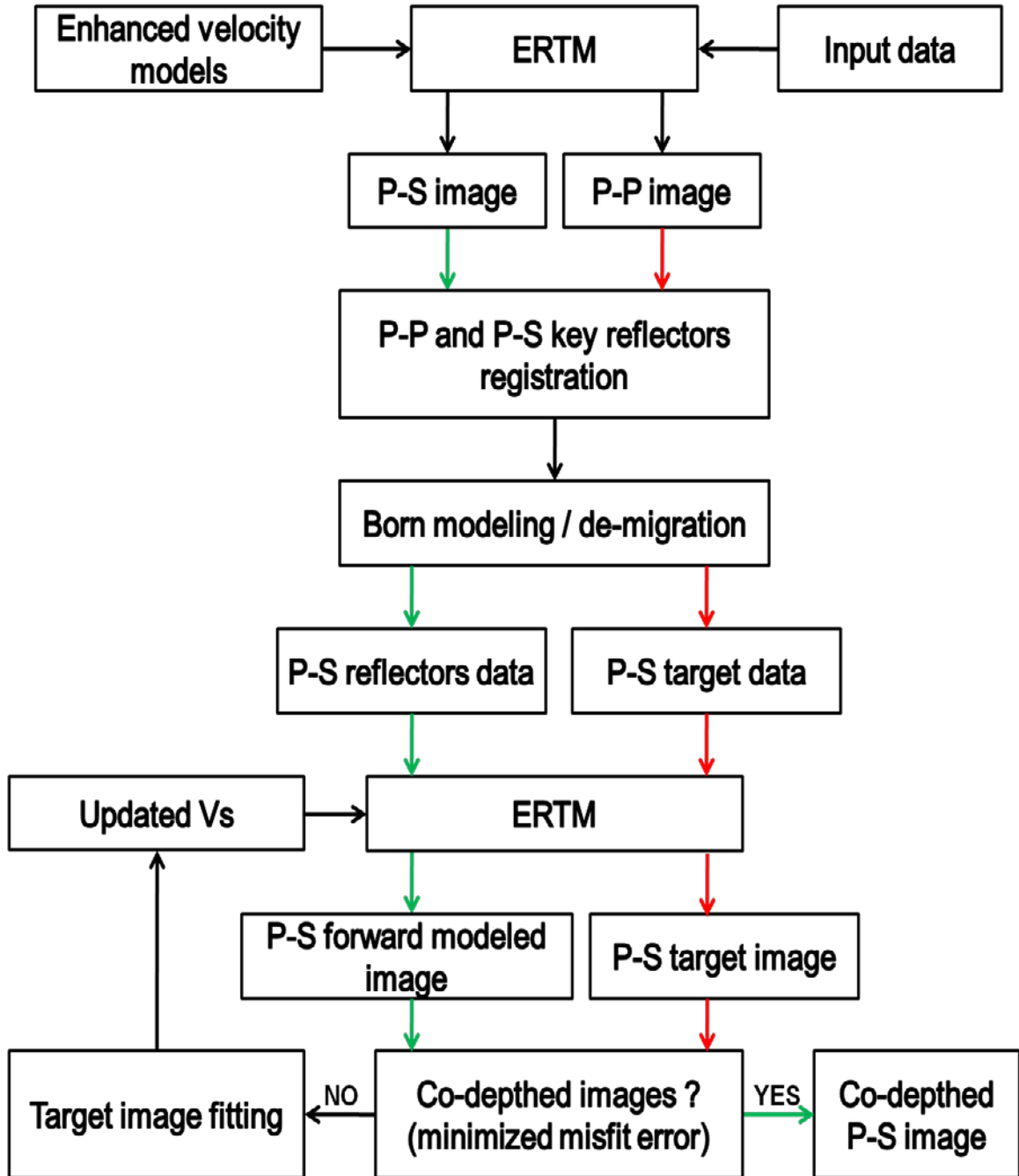


Figure 5.1: Workflow of P-P and P-S images co-depting procedure.

5.3 Synthetic data example

In this section we use the same 2D Gullfaks synthetic model introduced in section 3.3. Note that perturbations were added to the original V_s model in order to simulate near-surface velocity variations. In this example we use for migration an initial V_s model that does not account for the near-surface velocity perturbations present in the true V_s used for creating the data. The initial V_p model used for migration is a smoothed version of the true V_p model. We applied the proposed co-depting scheme in order to correct the P-S reflectors depth. Figure 5.2 shows the migration velocity models and related initial images. The P-P image seems largely unaffected by the errors in V_s migration velocity model and the reflectors are correctly imaged. While in the P-S image there are clear shifts in the reflectors due to the errors in the near-surface part of the V_s migration velocity. The differences in resolution and amplitude between the P-P and P-S images can also be observed.

After migration using the initial velocity models, we interpreted a key reflector at 1000 *m* depth in both the P-P and P-S images. These reflectors were de-migrated to 2C P-S reflection data using equation 5.2, and remigrated as P-S images representing the target image and the initial forward modeled image. Figure 5.3 compares the target P-S reflector image produced using P-P Born modeled data to the inconsistent initial forward modeled P-S reflector image, and shows the updated P-S reflector image after 6 iterations of target image procedure. The black arrows in Figure 5.3 refer to the areas of depth shifts in the reflector before and after the co-depting scheme implementation. Note that the velocity updates were deliberately constrained to the shallow part of the velocity model, reflecting our prior knowledge of the problem. The V_s model produced after 6 iterations of target image fitting procedure shown in Figure 5.4 was used to remigrate the original P-S data and produced co-depted P-S image shown in Figure 5.5. The updated P-S image is consistent in depth and successfully matched to P-P image, while it does not coherent because that is not ensured by the co-depting procedure.

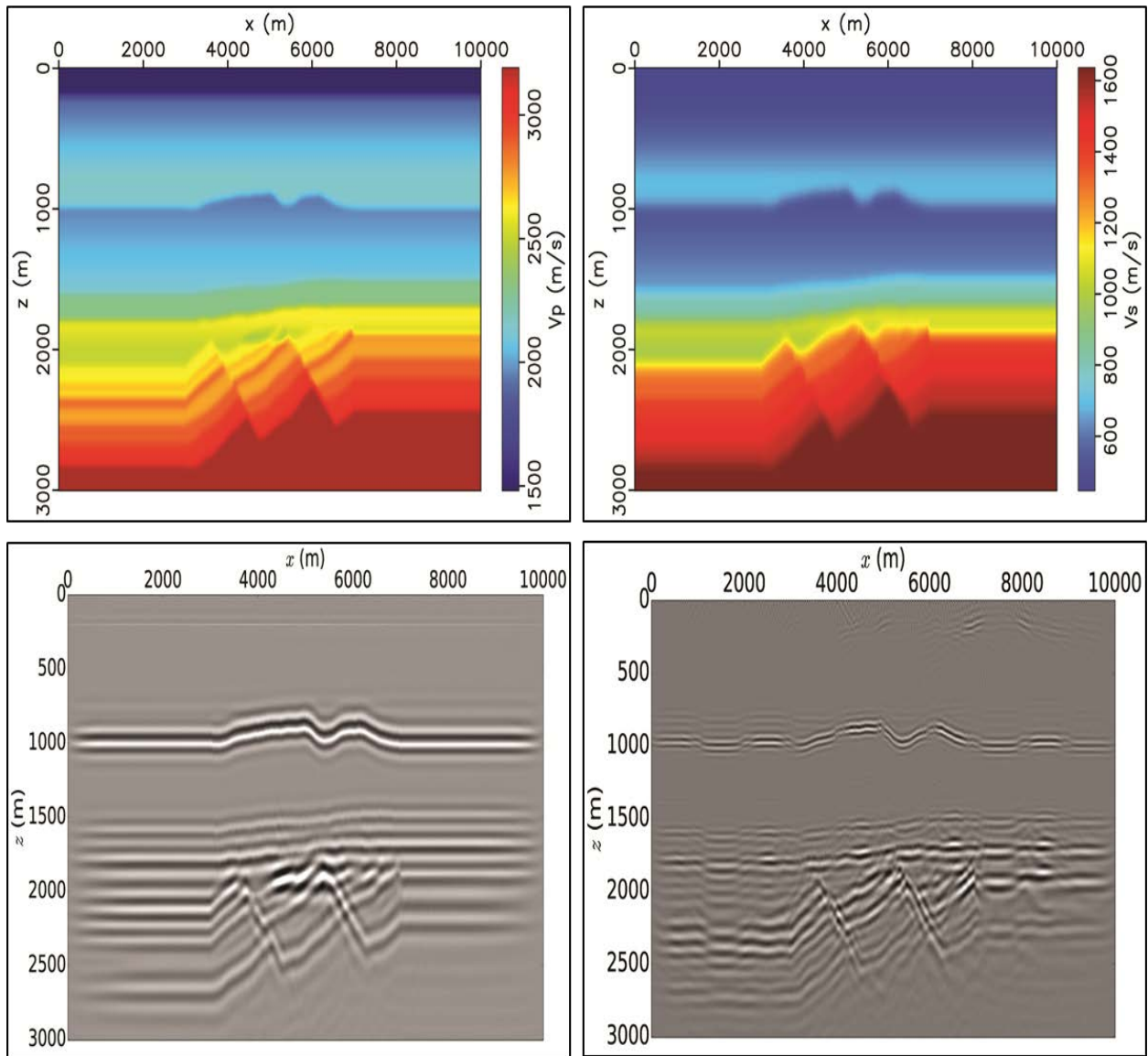


Figure 5.2: Migration velocity models and produced initial images.

Top left: V_p model.

Top right: V_s initial model.

Bottom left: P-P image.

Bottom right: P-S initial image.

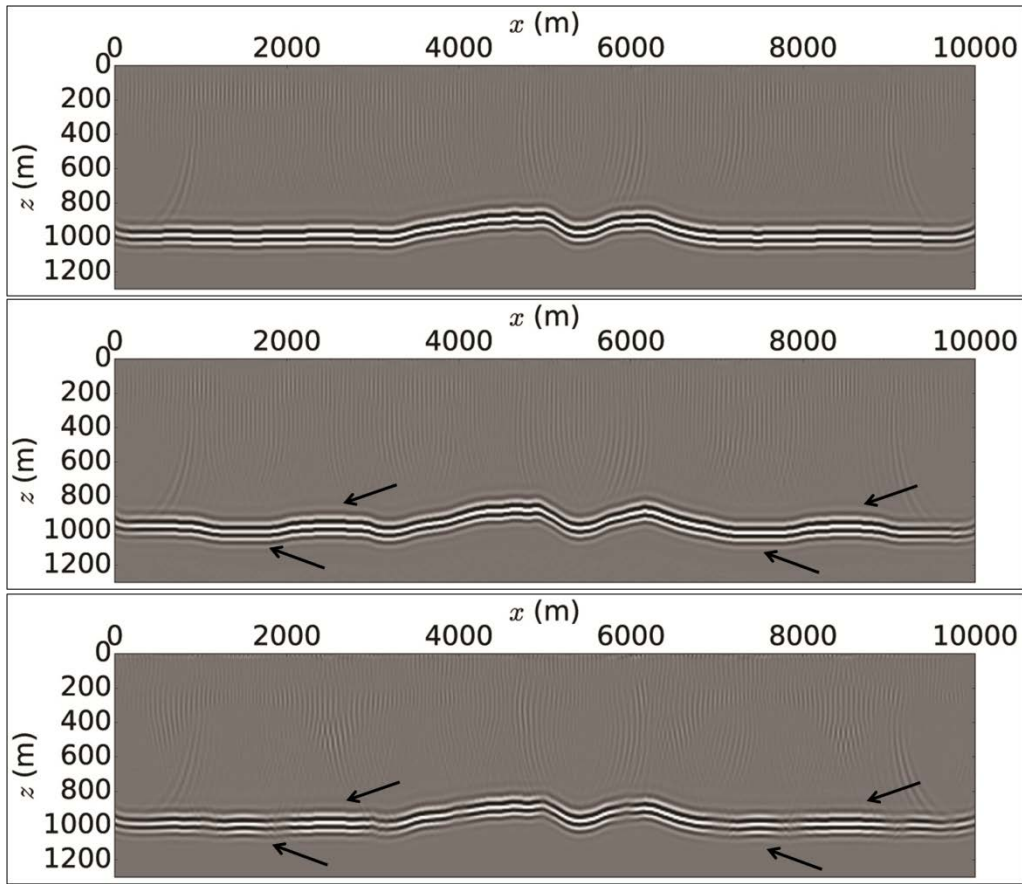


Figure 5.3: Key reflectors co-depting procedure.

Top: Target P-S reflector image produced using P-S Born modeled data.

Middle: Initial forward modeled P-S reflector image showing inconsistent depth.

Bottom: Updated P-S reflector image using target image fitting procedure after iterations.

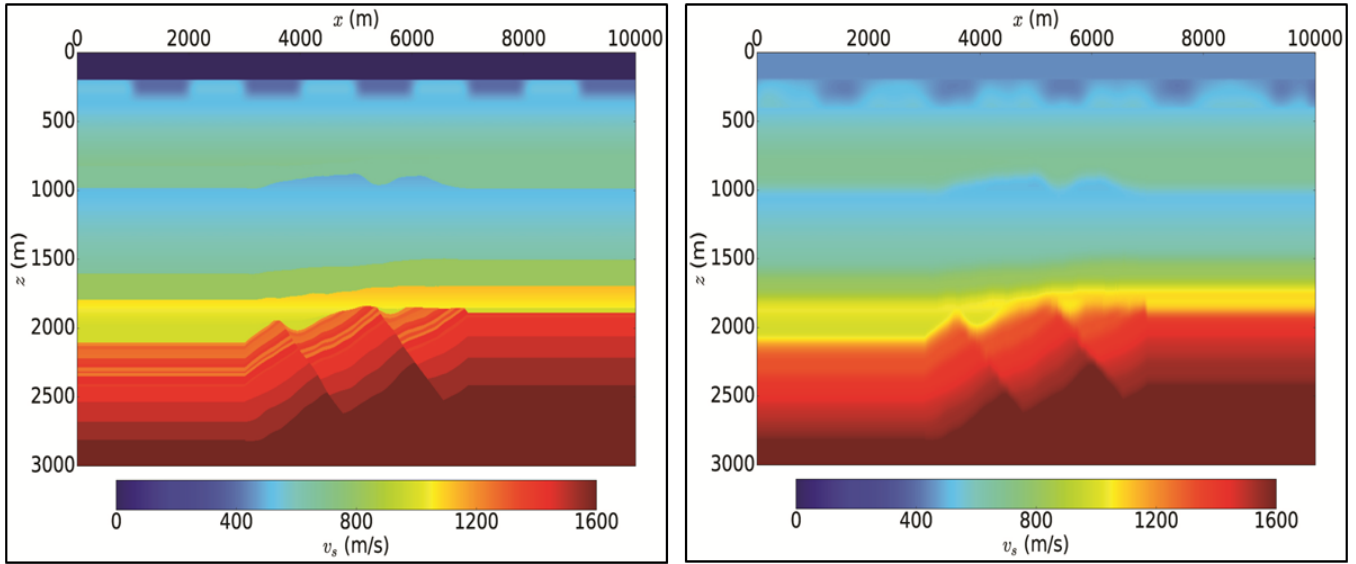


Figure 5.4: True V_s model (left) and updated V_s model (right) after 6 iterations using target image fitting procedure.

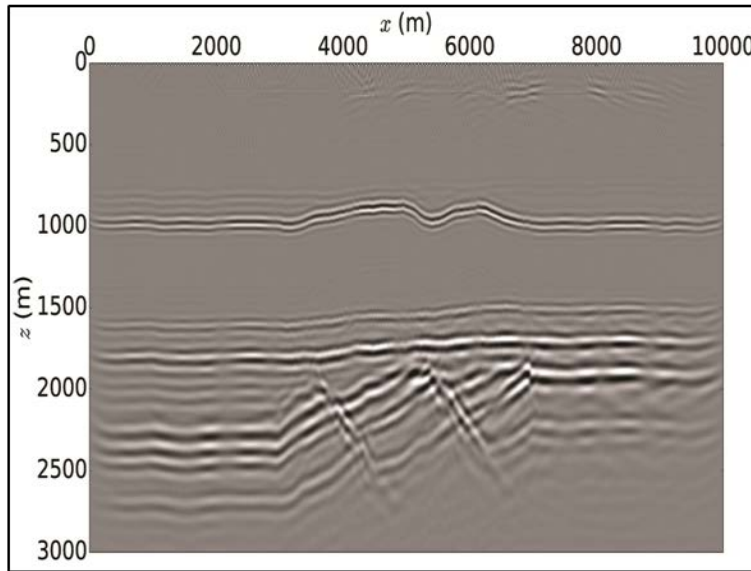


Figure 5.5: Updated P-S image after co-depting procedure.

5.4 Field data example

In this example, we apply the method on the N-S 2D line extracted from the Blackfoot 3D-3C dataset, and we follow the results obtained from stack-power maximization scheme discussed in section 4.4. Stack-power maximization procedure is necessary to improve the initial V_p and V_s models that produce coherent and sharpened images. However, the produced P-S image does not show an accurate depth matching with the P-P image. To co-depth the P-P and P-S images we apply the target image fitting procedure to generate the enhanced velocity model that best match the key reflectors on P-P and P-S depth migrated images.

The first step was to register and correlate the key reflectors on both P-P and P-S images. Interpretation of the key reflectors was done using Petrel software with auto-tracking feature in order to minimize the error in reflector depth registration. We registered 4 key reflectors to be correlated on P-P image and P-S images produced by stack-power maximization procedure, as shown in Figure 5.6. Note the depth inconsistency between the registered reflectors. The registered reflectors are used to build a reflectivity model for both P-P and P-S images. Using the last updated V_s model from stack-power optimization, the registered P-P reflectors were de-migrated to data domain and re-migrated in order to create P-S target image equivalent to P-P image.

In order to provide a robust long-wavelength solution and to avoid cycle skipping, the frequency range of the source wavelet in Born modeling was set to a suitable low frequency range of 5-15 Hz. It is critical to satisfy the condition that the maximum difference in depth between reflectors of the target image and the forward modeled image should be less than $\lambda/4$, and at the same time respect the minimum thickness between reflectors in the modeled image to avoid any destructive interference that can occur with very low frequency.

The V_s model updates after 10 iterations of target image fitting using the low frequency wavelet is shown in Figure 5.7. No vertical mute was applied to the velocity updates, which means that the velocity updates were not constrained to a particular part of the model. A second implementation of target image fitting was applied with a higher frequency wavelet covering the bandwidth 5-30 Hz, and using the updated V_s for low frequency model as a new starting point. This was used as a part of a multiscale approach to fine tune the model. In this case, the reflectors need to be re-picked, as their depth differences are reduced, allowing a higher frequency to be used for Born modeling process. The V_s model updates

after 3 iterations of target image fitting using the high frequency wavelet is shown in Figure 5.7. The algorithm we use enables fast quality control mechanism during implementation by checking the resulting migrated image per iteration.

In Figure 5.8, the migrated P-S images using updated V_s models from target image fitting procedure are compared to the P-S image produced from stack-power maximization. It is obvious how the P-S image was enhanced using target image fitting, where velocity updates of low frequency model corrected the significant inconsistency in depth of P-S reflectors, especially at the edges of the section. The high frequency model updates refined the corrections. Figure 5.9 display the misfit function numerical values for target image fitting procedure.

Despite improving depth consistency of P-S image, the target image fitting procedure does not guarantee an improvement in focusing and coherency of the produced migrated image. That requires a final stack-power optimization application in order to produce the optimum velocity model that can achieve both co-depting and focusing of the final P-S image. Figure 5.10 shows the V_s model updates after 10 iterations of stack-power optimization and the corresponding P-S migrated image, which is now better focused and co-depted to the P-P image. Figure 5.11 display the final stack-power optimization misfit function values along 10 iterations.

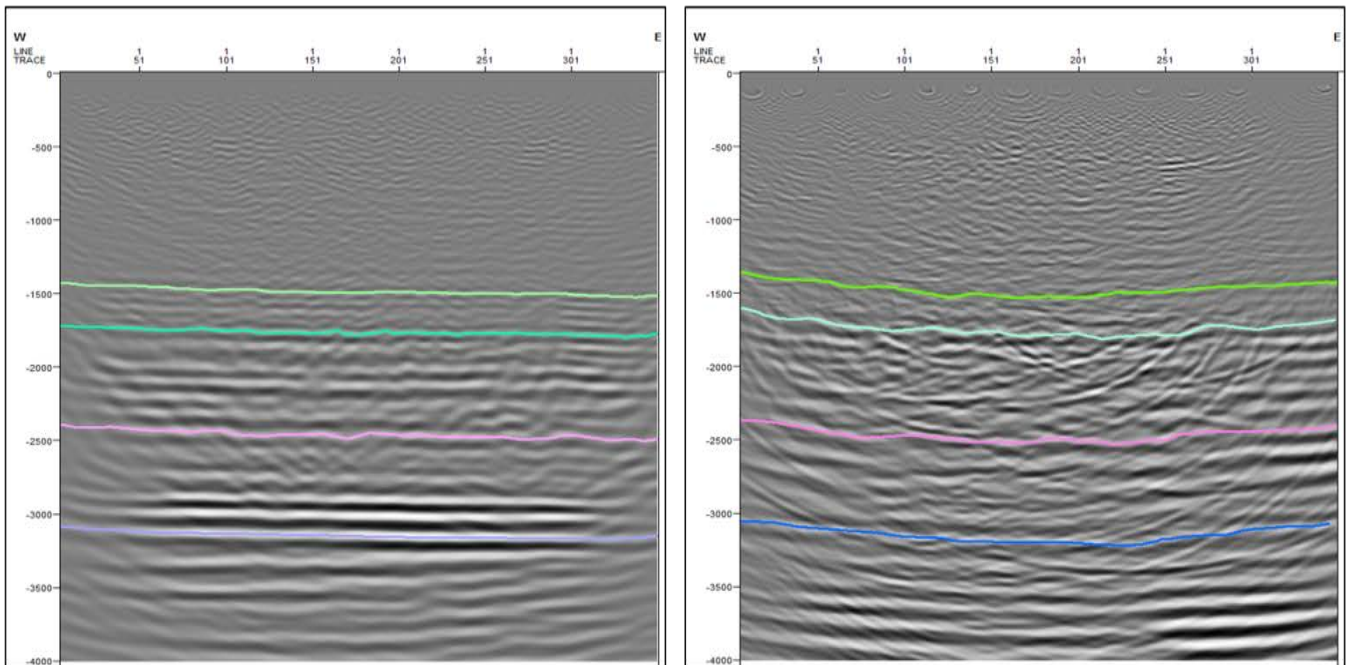


Figure 5.6: Registration of 4 key reflectors on P-P image (left) and P-S image (right)

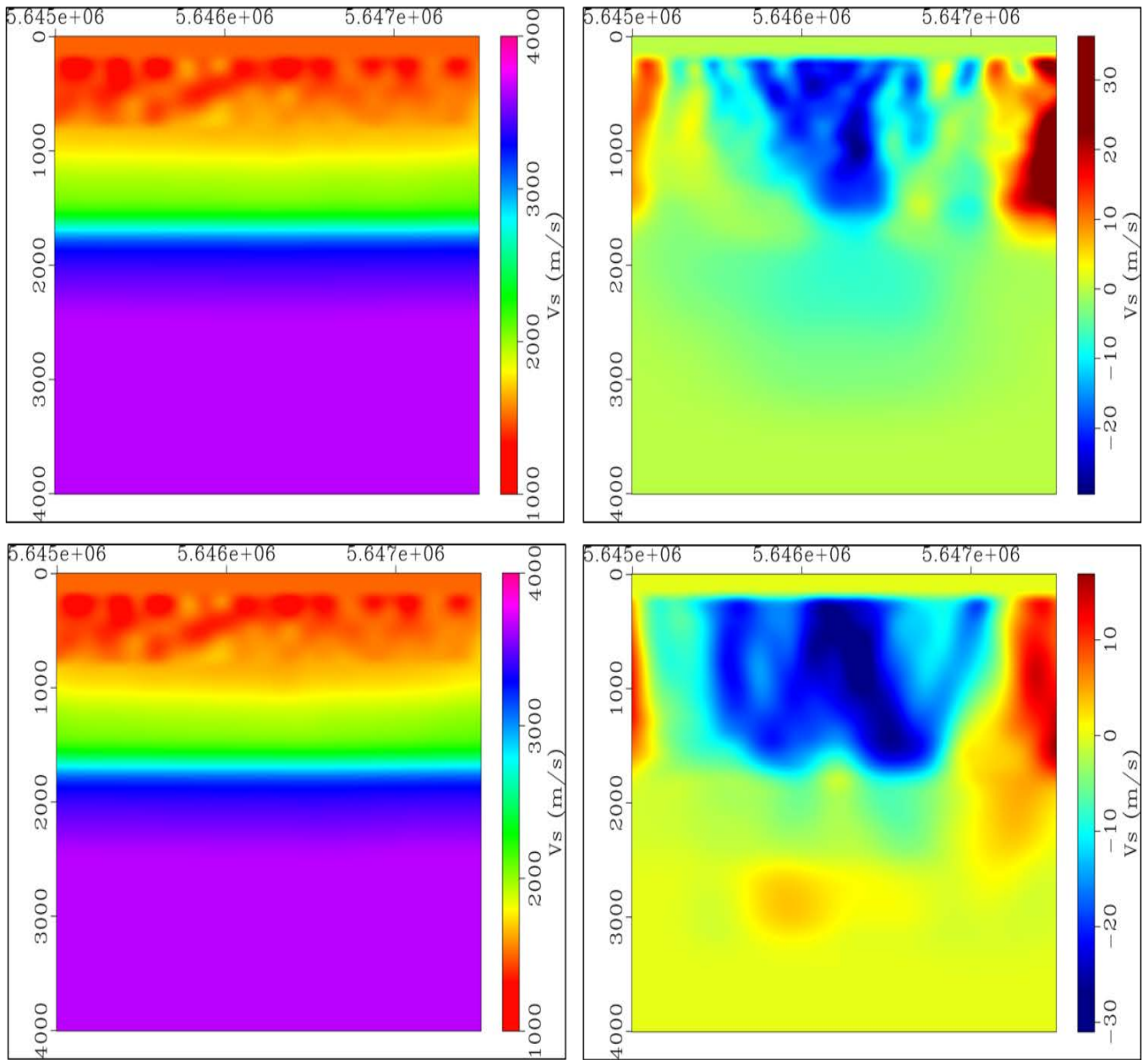


Figure 5.7: Results of target image fitting procedure.

Top left: Produced V_s model after 10 iterations of target image fitting for the low frequency model.

Top right: V_s model updates after 10 iterations of target image fitting for the low frequency model.

Bottom left: Produced V_s model after 3 iterations of target image fitting for the high frequency model.

Bottom right: V_s model updates after 3 iterations of target image fitting for the high frequency model.

Note the distribution of the updates over the model edges with positive values in order to compensate for velocity errors produced in stack-power procedure due to poor illumination.

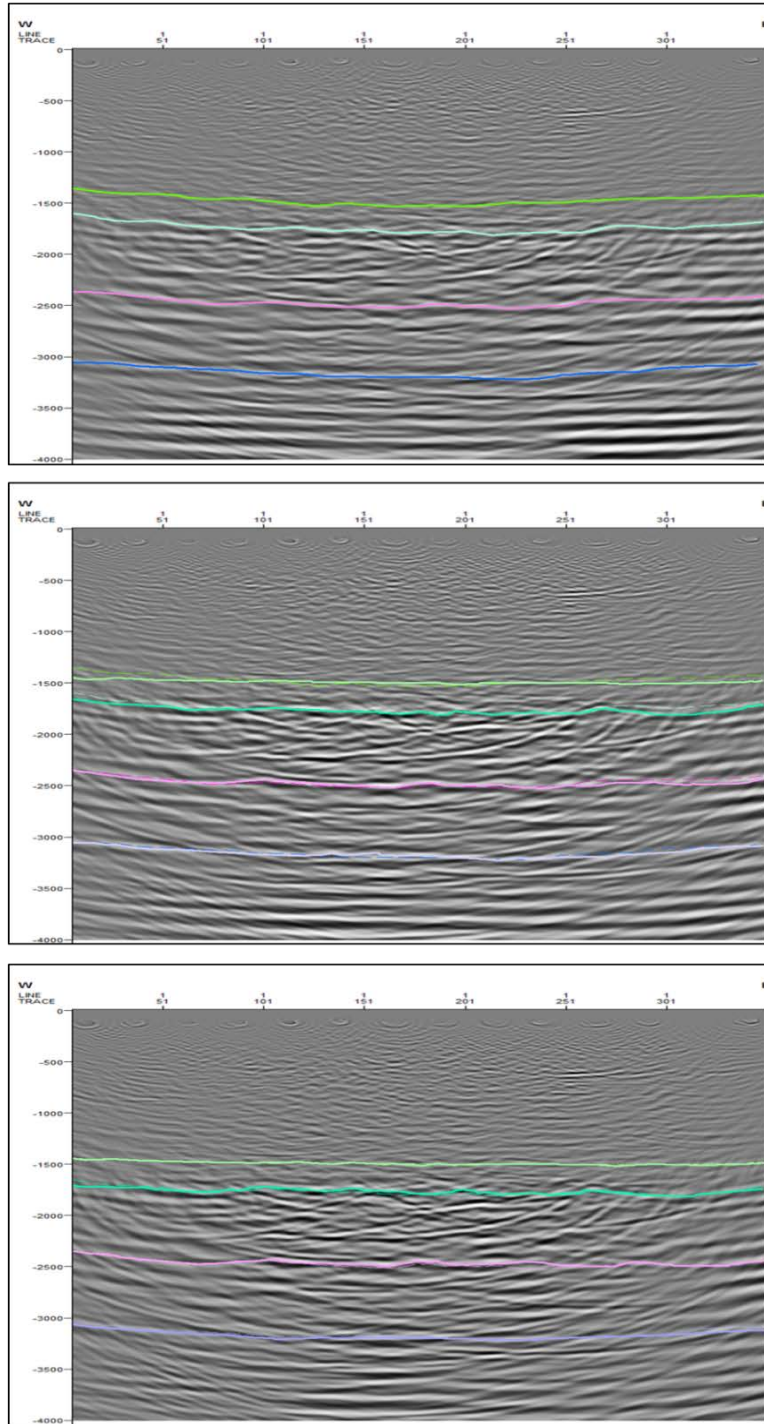


Figure 5.8: Produced P-S images.

Top: Initial P-S image migrated using V_s model updated by stack-power maximization.

Middle: Produced P-S image using V_s updated by target image fitting for the low frequency model.

Bottom: Produced P-S image using V_s updated by target image fitting for the high frequency model.

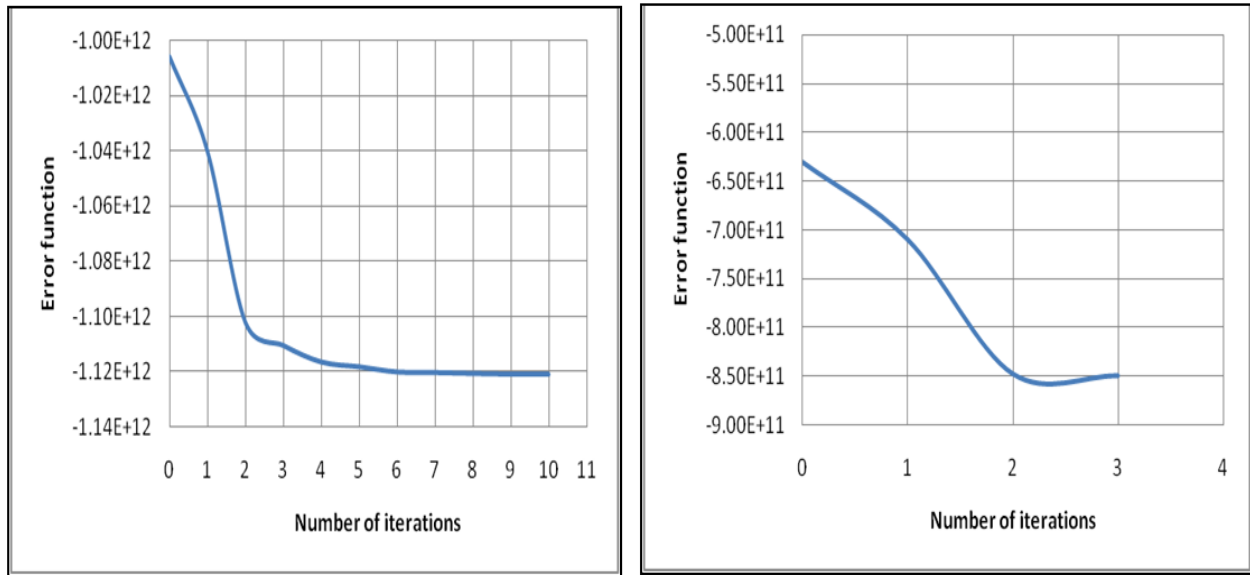


Figure 5.9: Target image fitting function numerical values for low frequency model (left) and high frequency model (right).

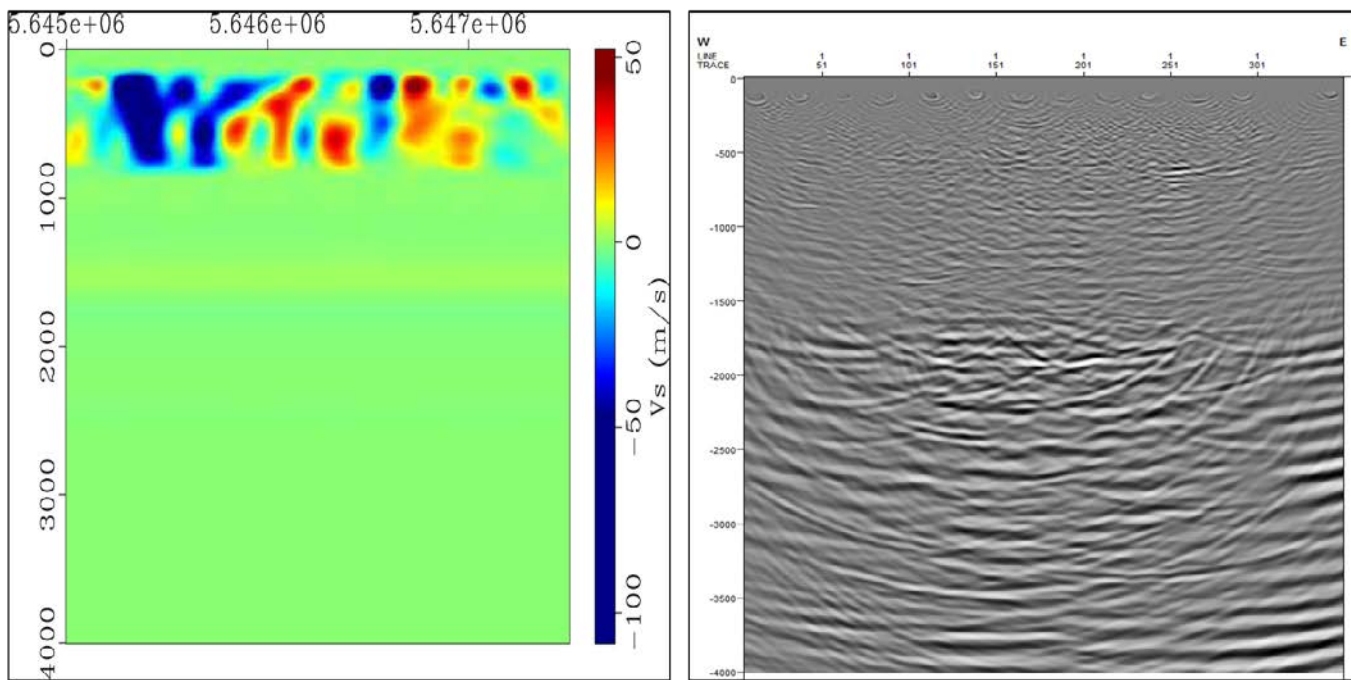


Figure 5.10: Final V_s model updates after 10 iterations of stack-power optimization and the corresponding P-S migrated image.

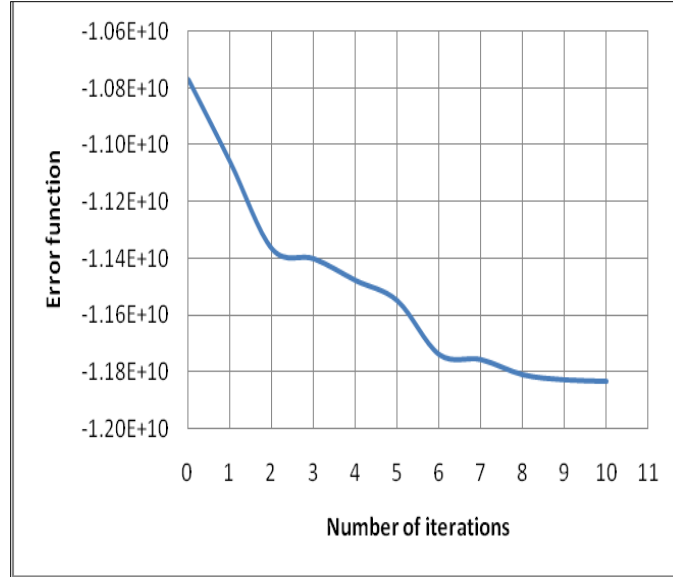


Figure 5.11: Final stack-power maximization error function values.

5.5 Discussion

The work described in this chapter is a continuation of the work discussed in chapter 3 and chapter 4, as part of a comprehensive scheme to achieve the main objective of producing optimized subsurface images from multi-component data. We presented a method that automatically co-depth P-P and P-S images migrated using elastic reversed time migration. The method is based on Born modeling/de-migration of interpreted key reflectors in P-P and P-S images to produce synthetic P-S data. These data are used to produce P-S images which are input to the automatic procedure of target image fitting. The result is an updated velocity model that co-depth the P-S and P-P images.

The method was tested on 2D synthetic and field datasets providing promising results. The co-depthing process is resilient and can be applied for all registered reflectors at once or for each reflector in a layer-stripping mode. The results presented in this chapter reveal the robustness of the technique even with application over 4 reflectors model. The main source of depth uncertainty in this scheme will be the accuracy of P-P depth image. For that we rely on the stack-power optimization based on ERTM to produce the most accurate possible P-P depth image. Adding geological control points such as well data will definitely reduce the depth uncertainty of the produced images and velocity models.

The main condition for successful application of the process is that the maximum difference in depth between the target image and the forward modeled image registered reflector should be less than $\lambda/4$, and at the same time respect the minimum thickness between reflectors in the modeled image to avoid any destructive interference that can occur with very low frequency. Accordingly, implementation with gradual increase in the model frequency is required to refine the velocity model.

Target image fitting procedure does not guarantee an improvement in the produced image coherency and focusing. That requires further application of stack-power optimization in order to produce the optimum velocity model that can achieve both co-depting and focusing of the final P-S image. The final image shown in Figure 5.10 does not look perfectly coherent, due to the low illumination of the lower section, as the implemented workflow of stack-power maximization and target image fitting could adjust the top section of the image in sufficient way while it suffered in the image lower section. That can also be observed from comparing the initial V_s/V_p ratio and the final ratio after stack-power maximization and co-depting application, as shown in Figure 5.12. Application of 3D data will certainly provide more reliable results.

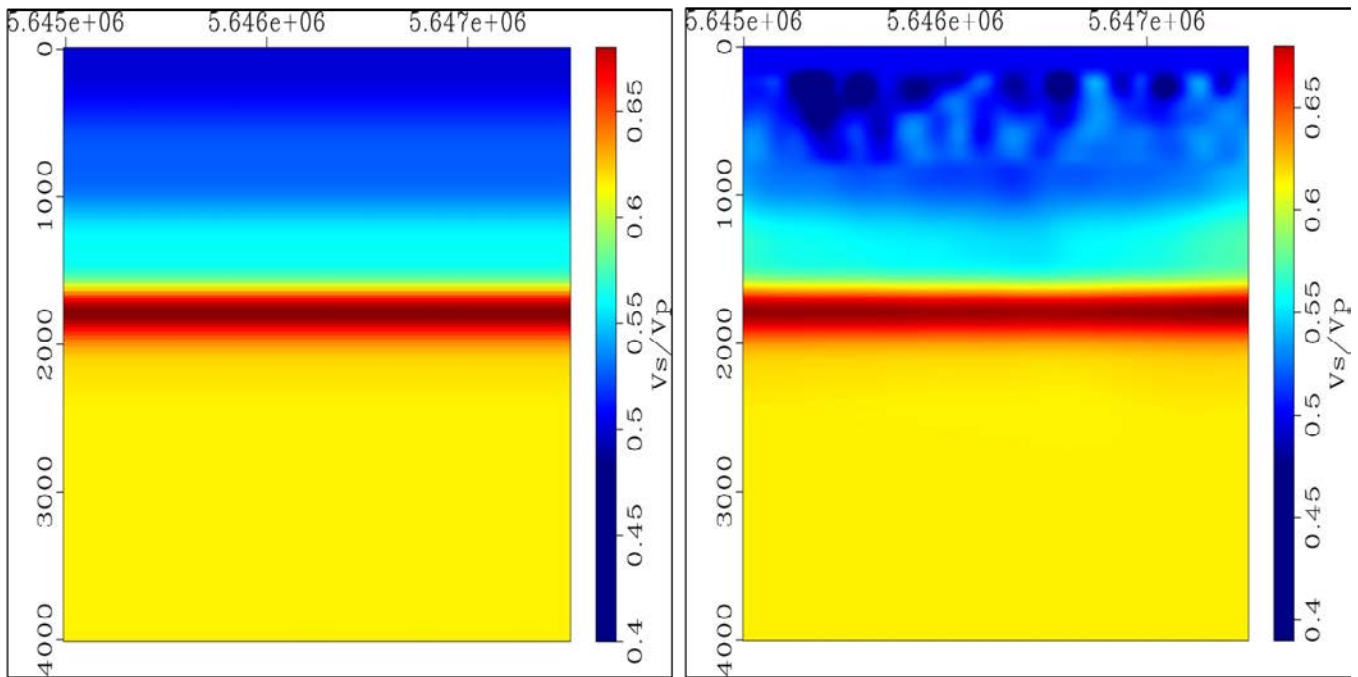


Figure 5.12: Comparison between initial V_s/V_p ratio (left) and final V_s/V_p ratio (right).

6 Conclusions

In this thesis we visited the challenges related to converted wave processing and imaging and introduced a novel workflow for accurate depth imaging and velocity analysis of multi-component data in isotropic media. The workflow combines imaging via ERTM and velocity analysis using WEMVA techniques in a comprehensive data-driven framework. The purpose of this work was to make a step toward more robust elastic imaging and velocity analysis and to better understand elastic imaging challenges and limitations.

The workflow was tested over synthetic and field dataset. First, we successfully implemented new imaging conditions for ERTM in order to overcome the polarity reversal problem, and investigated the main reasons for cross-talking between different wave-modes. Second, we applied stack-power optimization to produce improved V_p and V_s models that enhanced the image coherency. Third, we applied co-depting scheme based on Born modeling/de-migration method and target image fitting procedure in order to produce the V_s model that result in depth consistent P-S and P-P images. Finally, we further applied stack-power optimization in order to produce the optimum velocity model that can focus the co-depted P-S image.

The application of this workflow does not require any application of data rotation, wavefield separation, or static correction. The results presented in this thesis show the robustness and practicality of the workflow to produce enhanced velocity models and accurate subsurface elastic images even with low signal to noise ratio and without de-noising the data. Despite the computationally expensive implementation of the workflow, it can be considered as time and cost saving approach, as it can substantially reduce the exploration cycle time and cost.

However, there are limitations and challenges that must be considered in elastic imaging of multi-component data. We can categorize them to the following:

- Acquisition related: geophone coupling and vector fidelity and recording low frequency signal.
- Processing related: signal to noise ratio, multiple attenuation and preserving low frequency.
- Subsurface parameters: velocity fields accuracy, attenuation and anisotropy.
- Algorithm related: imaging of distinct P-P and P-S images and computational cost.

The acquisition related issues have the most devastating effects on elastic imaging, as no process will sufficiently recover missing information. In this thesis we tackled the issues of accurate imaging and velocity analysis in connection to vector fidelity, attenuation, and low frequency signal effects. The results discussed indicated the importance of broadband seismic and high fidelity of recordings, and the need for low frequency noise attenuation and de-multiple techniques in order to suppress low-frequency noise without wasting valuable information.

Further work should be initiated in areas of attenuation compensation and visco-elastic implementation of reverse-time migration in order to overcome the wave-mode cross-talk problem. Future work is necessary to consider anisotropy with multi-parameters inversion techniques, which will definitely yield significant enhancement of subsurface imaging and velocity analysis.

The computational cost of stack-power optimization scheme, and the time consuming testing phase in order to optimize the algorithm efficiency and compatibility with the available clusters environments, made it hard to finalize 3D inversion of V_s model in time for delivering this thesis. For the meantime, we successfully implemented 3D inversion of V_p model and the algorithm performed in a stable way producing outstanding results. Computational resources can limit the resolution and the number of possible elastic subsurface parameters inversion. However, this limitation is constantly diminished with the rapid technological development. Further work is required to tackle the main challenges of stack-power optimization scheme, as the non-linearity of the objective function and the non-uniqueness of the optimization solution. In future we may consider using global optimization approaches such as Mont-Carlo method.

The main step in order to find answers is to first understand the questions. We believe the work presented in this thesis can help in better understanding of the challenges and limitations that need to be addressed in elastic imaging and velocity analysis of multi-component data.

References

- Aki, K. & Richards, P. 1980. Quantative seismology: Theory and methods. *Freeman and Company*, 2
- Alford, R. 1986. Shear data in the presence of azimuthal anisotropy: Dilley, Texas. *SEG Technical Program Expanded Abstracts 1986*. Society of Exploration Geophysicists.
- Alkhalifah, T. 1997. Velocity analysis using nonhyperbolic moveout in transversely isotropic media. *Geophysics*, 62(6), pp 1839-1854.
- Alves, G. & Biondi, B. 2016. Imaging condition for elastic reverse time migration. *SEG Technical Program Expanded Abstracts 2016*. Society of Exploration Geophysicists.
- Artman, B., Podladtchikov, I. & Goertz, A. 2009. Elastic time-reverse modeling imaging conditions. *SEG Technical Program Expanded Abstracts 2009*. Society of Exploration Geophysicists.
- Bale, R. A. & Stewart, R. R. 2002. The impact of attenuation on the resolution of multicomponent seismic data. *SEG Technical Program Expanded Abstracts 2002*. Society of Exploration Geophysicists.
- Barkved, O., Bartman, B., Gaiser, J., Van Dok, R., Johns, T., Kristiansen, P., Probert, T. & Thompson, M. 2004. The many facets of multicomponent seismic data. *Oilfield Review*, 16(2), pp 42-56.
- Baysal, E., Kosloff, D. D. & Sherwood, J. W. 1983. Reverse time migration. *Geophysics*, 48(11), pp 1514-1524.
- Bertram, M. B. & Margrave, G. F. 2010. Recovery of Low Frequency Data from 10Hz Geophones. *CREWES Research Report*, 22.
- Biondi, B. & Sava, P. 1999. Wave-equation migration velocity analysis. *SEG Technical Program Expanded Abstracts 1999*. Society of Exploration Geophysicists.
- Bland, H. C., Bertram, M. B. & Gallant, E. V. 2004. Testing the quality of geophone plants for 3-C land acquisition,
- Broto, K., Ehinger, A., Kommedal, J. H. & Folstad, P. G. 2003. Anisotropic travelttime tomography for depth consistent imaging of PP and PS data. *The Leading Edge*, 22(2), pp 114-119.

- Byrd, R. H., Lu, P., Nocedal, J. & Zhu, C. 1995. A limited memory algorithm for bound constrained optimization. *SIAM Journal on Scientific Computing*, 16(5), pp 1190-1208.
- Cafarelli, B., Randazzo, S., Campbell, S., Sobreira, J. F. F., Guimaraes, M. A. G., Rodriguez, C., Johann, P. & Theodoro, C. 2006. Ultra-deepwater 4-C offshore Brazil. *The Leading Edge*, 25(4), pp 474-477.
- Cary, P. W. & Eaton, D. W. 1993. A simple method for resolving large converted-wave (P-SV) statics. *Geophysics*, 58(3), pp 429-433.
- Chang, W.-F. & McMechan, G. A. 1987. Elastic reverse-time migration. *Geophysics*, 52(10), pp 1365-1375.
- Chauris, H. & Benjema, M. 2010. Seismic wave-equation demigration/migration. *Geophysics*, 75(3), pp S111-S119.
- Chavent, G. 2009. *Nonlinear least squares for inverse problems: theoretical foundations and step-by-step guide for applications*: Springer Science & Business Media.
- Chavent, G. & Jacewitz, C. A. 1995. Determination of background velocities by multiple migration fitting. *Geophysics*, 60(2), pp 476-490.
- Choi, Y. & Alkhalifah, T. 2012. Application of multi-source waveform inversion to marine streamer data using the global correlation norm. *Geophysical Prospecting*, 60(4), pp 748-758.
- Cieslewicz, D. 1999. Near-surface seismic characterization using three-component buried geophones.
- Claerbout, J. F. 1971. Toward a unified theory of reflector mapping. *Geophysics*, 36(3), pp 467-481.
- Crampin, S. & Peacock, S. 2005. A review of shear-wave splitting in the compliant crack-critical anisotropic Earth. *Wave motion*, 41(1), pp 59-77.
- DeAngelo, M. V., Backus, M., Hardage, B. A., Murray, P. & Knapp, S. 2003. Depth registration of P-wave and C-wave seismic data for shallow marine sediment characterization, Gulf of Mexico. *The Leading Edge*, 22(2), pp 96-105.

- Dellinger, J. & Etgen, J. 1990. Wave-field separation in two-dimensional anisotropic media. *Geophysics*, 55(7), pp 914-919.
- Denli, H. & Huang, L. 2008. Elastic-wave reverse-time migration with a wavefield-separation imaging condition. *SEG Technical Program Expanded Abstracts 2008*. Society of Exploration Geophysicists.
- Dierckx, P. 1995. *Curve and surface fitting with splines*: Oxford University Press.
- Du, Q., Zhu, Y. & Ba, J. 2012. Polarity reversal correction for elastic reverse time migration. *Geophysics*, 77(2), pp S31-S41.
- Duan, Y. & Sava, P. Converted-waves imaging condition for elastic reverse-time migration. 2014 SEG Annual Meeting, 2014. Society of Exploration Geophysicists.
- Duan, Y. & Sava, P. 2015. Scalar imaging condition for elastic reverse time migration. *Geophysics*, 80(4), pp S127-S136.
- Eaton, D., Slotboom, R., Stewart, R. & Lawton, D. 1990. Depth-variant converted-wave stacking. *SEG Technical Program Expanded Abstracts 1990*. Society of Exploration Geophysicists.
- Eaton, D. W., Caryt, P. W. & Schafer, A. W. 1991. Estimation of P-SV residual statics by stack-power optimization. *CREWES Research Report*, 3(88-106).
- Etgen, J. T. Prestacked migration of P and Sv-waves. 1988 SEG Annual Meeting, 1988. Society of Exploration Geophysicists.
- Fomel, S., Sava, P., Vlad, I., Liu, Y. & Bashkardin, V. 2013. Madagascar: Open-source software project for multidimensional data analysis and reproducible computational experiments. *Journal of Open Research Software*, 1(1), pp.
- Foss, S.-K., Ursin, B. & Hoop, M. V. d. 2005. Depth-consistent reflection tomography using PP and PS seismic data. *Geophysics*, 70(5), pp U51-U65.
- Gaiser, J. PS-wave Attenuation and Resolution Related to Vp/Vs Estimates. 75th EAGE Conference & Exhibition incorporating SPE EUROPEC 2013, 2013.
- Gaiser, J. E. 1996. Multicomponent VP/VS correlation analysis. *Geophysics*, 61(4), pp 1137-1149.

- Gaiser, J. E. 1998. Compensating OBC data for variations in geophone coupling. *SEG Technical Program Expanded Abstracts 1998*. Society of Exploration Geophysicists.
- Gaiser, J. E., Barr, F. J. & Paffenholz, J. 2000. Horizontal and vertical receiver-consistent deconvolution for an ocean bottom cable. Google Patents.
- Garotta, R. 1984. Two-component acquisition as a routine procedure. *SEG Technical Program Expanded Abstracts 1984*. Society of Exploration Geophysicists.
- Garotta, R. 1985. Observation of shear waves and correlation with P events. *Seismic Shear Waves: Handbook of Geophysical Exploration*, 15(1-86).
- Garotta, R., Granger, P.-Y. & Dariu, H. 2000. Elastic parameter derivations from multi-component data. *SEG Technical Program Expanded Abstracts 2000*. Society of Exploration Geophysicists.
- Granli, J. R., Arntsen, B., Sollid, A. & Hilde, E. 1999. Imaging through gas-filled sediments using marine shear-wave data. *GEOPHYSICS*, 64(3), pp 668-677.
- Gray, S. H., Etgen, J., Dellinger, J. & Whitmore, D. 2001. Seismic migration problems and solutions. *Geophysics*, 66(5), pp 1622-1640.
- Grechka, V., Pech, A. & Tsvankin, I. 2002. Multicomponent stacking-velocity tomography for transversely isotropic media. *Geophysics*, 67(5), pp 1564-1574.
- Guevara, S. E., Margrave, G. F. & Isaac, H. 2015. A method for converted wave receiver statics correction in the CRG domain. *SEG Technical Program Expanded Abstracts 2015*. Society of Exploration Geophysicists.
- Gulati, J. S., Stewart, R. R. & Parkin, J. M. 1998. 3C-3D VSP: The Blackfoot experiment,
- Harrison, M. P. 1992. *Processing of P-SV surface-seismic data: Anisotropy analysis, dip moveout, and migration*: Geology and Geophysics, University of Calgary.
- Henley, D. 1999. The radial trace transform: An effective domain for coherent noise attenuation and wavefield separation. *SEG Technical Program Expanded Abstracts 1999*. Society of Exploration Geophysicists.

- Herrenschmidt, A., Granger, P.-Y., Audebert, F., Gereau, C., Etienne, G., Stopin, A., Alerini, M., Lebegat, S., Lambaré, G. & Berthet, P. 2001. Comparison of different strategies for velocity model building and imaging of PP and PS real data. *The Leading Edge*, 20(9), pp 984-995.
- Hokstad, K., Mittet, R. & Landrø, M. 1998. Elastic reverse time migration of marine walkaway vertical seismic profiling data. *Geophysics*, 63(5), pp 1685-1695.
- Ikelle, L. & Amundsen, L. 2005. *Introduction to Petroleum Seismology*: Society of Exploration Geophysicists.
- Jones, I. F. 2015. Estimating subsurface parameter fields for seismic migration: velocity model building. *Encyclopedia of exploration geophysics*. Society of Exploration Geophysicists.
- Kendall, R. R., Gray, S. H. & Murphy, G. E. 1998. Subsalt imaging using prestack depth migration of converted waves: Mahogany Field, Gulf of Mexico. *SEG Technical Program Expanded Abstracts 1998*. Society of Exploration Geophysicists.
- Kristensen, Å. & Hovem, J. M. 1991. Sensitivity of bottom loss to attenuation and shear conversion. *Shear Waves in Marine Sediments*. Springer.
- Krohn, C. E. 1984. Geophone ground coupling. *Geophysics*, 49(6), pp 722-731.
- Lawton, D. C., Stewart, R. R., Cordsen, A. & Hrycak, S. 1995. Advances in 3C-3D design for converted waves. *CREWES Res. Rep*, 7(43.1-43.1).
- Leader, C. & Biondi, B. 2014. Demigration and image space separation of simultaneously acquired data. *SEG Technical Program Expanded Abstracts 2014*. Society of Exploration Geophysicists.
- Lions, J. & Magenes, E. 1972. *Non-homogeneous boundary value problems and applications*, Berlin: Springer Verlag.
- Loewenthal, D., Lu, L., Roberson, R. & Sherwood, J. 1978. The wave equation applied to migration.
- Lou, M., Zhang, Y. & Pham, L. 2000. Shear-wave splitting and its implied fracture orientation analysis from PS waves in marine multi-component seismic data. *First Break*, 18(vii-ix).
- Lu, H.-x. & Margrave, G. F. 1998. Reprocessing the Blackfoot 3C-3D seismic data,

- MacLeod, M., Hanson, R., Bell, C. & McHugo, S. 1999. The Alba Field ocean bottom cable seismic survey: Impact on development. *The Leading Edge*, 18(11), pp 1306-1312.
- Miller, S. L. 1996. *Multicomponent Seismic Data Interpretation*. M.Sc. thesis, Univ. of Calgary.
- Mora, P. 1987. Nonlinear two-dimensional elastic inversion of multioffset seismic data. *Geophysics*, 52(9), pp 1211-1228.
- Mulder, W. & Ten Kroode, A. 2002. Automatic velocity analysis by differential semblance optimization. *Geophysics*, 67(4), pp 1184-1191.
- Nickel, M. & Sonneland, L. 2004. Automated PS to PP event registration and estimation of a high-resolution Vp-Vs ratio volume. *SEG Technical Program Expanded Abstracts 2004*. Society of Exploration Geophysicists.
- Nocedal, J. & Wright, S. J. 2000. Numerical optimization. 2nd printing. New York: Springer.
- Ogiesoba, O. C. & Stewart, R. R. 2003. Vp/Vs from multicomponent seismic data and automatic PS to PP time mapping. *SEG Technical Program Expanded Abstracts 2003*. Society of Exploration Geophysicists.
- Plessix, R.-E. 2006. A review of the adjoint-state method for computing the gradient of a functional with geophysical applications. *Geophysical Journal International*, 167(2), pp 495-503.
- Rickett, J. E. & Sava, P. C. 2002. Offset and angle-domain common image-point gathers for shot-profile migration. *Geophysics*, 67(3), pp 883-889.
- Rocha, D., Tanushev, N. & Sava, P. 2017. Anisotropic elastic wavefield imaging using the energy norm. *Geophysics*, 82(3), pp S225-S234.
- Rodriguez Suarez, C. 2000. *Advanced Marine Seismic Methods: Ocean-bottom and vertical-cable analyses*. Doctoral, University of Calgary.
- Ronen, J. & Claerbout, J. F. 1985. Surface-consistent residual statics estimation by stack-power maximization. *Geophysics*, 50(12), pp 2759-2767.

- Sava, P. & Biondi, B. 2004. Wave-equation migration velocity analysis. I. Theory. *Geophysical Prospecting*, 52(6), pp 593-606.
- Sava, P. & Hill, S. J. 2009. Overview and classification of wavefield seismic imaging methods. *The Leading Edge*, 28(2), pp 170-183.
- Sava, P. & Vlad, I. 2008. Numeric implementation of wave-equation migration velocity analysis operators. *Geophysics*, 73(5), pp VE145-VE159.
- Shen, P., Symes, W. W. & Stolk, C. C. 2003. Differential semblance velocity analysis by wave-equation migration. *SEG Technical Program Expanded Abstracts 2003*. Society of Exploration Geophysicists.
- Simin, V., Harrison, M. P. & Lorentz, G. A. 1996. Processing the Blackfoot 3C-3D seismic survey,
- Slotboom, R. 1990. Converted wave (P-SV) moveout estimation. *SEG Technical Program Expanded Abstracts 1990*. Society of Exploration Geophysicists.
- Stewart, R. R. & Ferguson, R. J. 1996. Shear-wave interval velocity from PS stacking velocities. *Canadian Journal of Exploration Geophysics*, 32(139-142).
- Stewart, R. R., Gaiser, J. E., Brown, R. J. & Lawton, D. C. 2002. Converted-wave seismic exploration: Methods. *Geophysics*, 67(5), pp 1348-1363.
- Stewart, R. R., Gaiser, J. E., Brown, R. J. & Lawton, D. C. 2003. Converted-wave seismic exploration: Applications. *Geophysics*, 68(1), pp 40-57.
- Sun, R. & McMECHAN, G. A. 1986. Pre-stack reverse-time migration for elastic waves with application to synthetic offset vertical seismic profiles. *Proceedings of the IEEE*, 74(3), pp 457-465.
- Szydluk, T., Smith, P., Way, S., Aamodt, L. & Friedrich, C. 2007. 3D PP/PS prestack depth migration on the Volve field. *First break*, 25(4), pp.
- Tessmer, G. & Behle, A. 1988. COMMON REFLECTION POINT DATA-STACKING TECHNIQUE FOR CONVERTED WAVES. *Geophysical prospecting*, 36(7), pp 671-688.

- Thomsen, L. 1999. Converted-wave reflection seismology over inhomogeneous, anisotropic media. *Geophysics*, 64(3), pp 678-690.
- Tikhonov, A. N., Arsenin, V. I. A. k. & John, F. 1977. *Solutions of ill-posed problems*: Winston Washington, DC.
- Tree, E. The vector infidelity of the ocean bottom multicomponent seismic acquisition system. 61st EAGE Conference and Exhibition, 1999.
- Vaezi, Y. & DeMeersman, K. Supervirtual S-wave Refraction Interferometry for Converted Wave Statics and Near-surface S-wave Velocity Model Building. 76th EAGE Conference and Exhibition 2014, 2014.
- Virieux, J. 1986. P-SV wave propagation in heterogeneous media: Velocity-stress finite-difference method. *Geophysics*, 51(4), pp 889-901.
- Wang, W. & McMechan, G. A. 2015. Vector domain P and S decomposition in viscoelastic media. *SEG Technical Program Expanded Abstracts 2015*. Society of Exploration Geophysicists.
- Wang, Y., Lu, J., Shi, Y. & Yang, C. 2009. PS-wave Q estimation based on the P-wave Q values. *Journal of geophysics and engineering*, 6(4), pp 386.
- Weibull, W. W. & Arntsen, B. 2013. Automatic velocity analysis with reverse-time migration. *Geophysics*, 78(4), pp S179-S192.
- Weibull, W. W. & Arntsen, B. 2014. Anisotropic migration velocity analysis using reverse-time migration. *Geophysics*, 79(1), pp R13-R25.
- Xue, Z., Zhu, T., Fomel, S. & Sun, J. 2016. Q-compensated full-waveform inversion using constant-Q wave equation. *SEG Technical Program Expanded Abstracts 2016*. Society of Exploration Geophysicists.
- Yan, J. & Sava, P. Elastic wavefield imaging with scalar and vector potentials. 2007 SEG Annual Meeting, 2007. Society of Exploration Geophysicists.
- Yan, J. & Sava, P. 2008. Isotropic angle-domain elastic reverse-time migration. *Geophysics*, 73(6), pp S229-S239.

- Yan, R. & Xie, X.-B. 2009. A new angle-domain imaging condition for prestack reverse-time migration. *SEG Technical Program Expanded Abstracts 2009*. Society of Exploration Geophysicists.
- Zhang, Y. & Duan, L. 2012. Predicting multiples using a reverse time demigration. *SEG Technical Program Expanded Abstracts 2012*. Society of Exploration Geophysicists.
- Zhe, J. & Greenhalgh, S. A. 1997. Prestack multicomponent migration. *Geophysics*, 62(2), pp 598-613.
- Zhu, H. 2017. Elastic wavefield separation based on the Helmholtz decomposition. *Geophysics*, 82(2), pp S173-S183.
- Zhu, T. & Sun, J. 2017. Viscoelastic reverse time migration with attenuation compensation. *Geophysics*, 82(2), pp S61-S73.